University of Stuttgart
Faculty of Chemistry

Reactive Wetting of Tin-based Miniaturised Solder Joints

Von der Fakultät Chemie der Universität Stuttgart
zur Erlangung der Würde eines Doktors der
Naturwissenschaften (Dr. rer. Nat.) genehmigte Abhandlung

Vorgelegt von

Samuel Jordan Griffiths

aus Australien

Hauptberichter:	Prof. Dr. Guido Schmitz
Mitberichter:	Prof. Dr. André Zimmermann
Prüfungsvorsitzender:	Prof. Dr. Peer Fischer

Tag der Mündlichen Prüfung: 31 March 2022

Institüt für Materialwissenschaft (IMW) der Universität Stuttgart

2022

Abstract

The microelectronics industry drives efforts to continuously miniaturize solder joints. But within this context, other joint properties such as joint strength cannot be compromised. Commonly, wetting angles have been used as an indicator for the strength of a solder connection. However, the work of adhesion is a more accurate representation of bonding strength. In this work, we determine the contact angles for SnPb and SnPb solder alloys on both polished Cu and Ni substrates in the sessile-drop geometry using equivalent measurement conditions over their entire composition range at 350 °C and 500 °C. Surface tensions were also determined for both solder alloys for all compositions at both temperatures. From these raw results, the experimental work of adhesion can be determined via the Young-Dupre equation which relates the work of adhesion to the contact angle and surface tension. The composition dependence of the work of adhesion matches the thermodynamic stability of the product phase/s. The existence of the expected intermetallic phases was also controlled via SEM micrographs and EDX investigations. This result corroborates the concept of Eustathopoulos which states that the reactive spreading triple line equilibrates on the product phase of highest Sn concentration. Finally, thermodynamic modelling of the work of adhesion, according to the approach of Butler, has indicated both significant segregation of Sn at the reactive solid-liquid interface, and Pb/Bi segregation at the liquid surface.

It is well understood that capillary forces become more predominant at smaller liquid volumes. Nonetheless, the wetting behavior of reactive solder joints in dependence on solder volume is not well understood. Here we investigate reactive wetting equilibria on eutectic SnPb solder on restricted geometry Cu samples. The Cu samples were produced by a process of laser writing lithography and electrodeposition and consisted of a circular pad to which a long straight track was attached, taking the geometric form of a “lollipop”. With this geometry, a ball of solder melted on the pad first wets the pad and then spreads along the track. Size dependencies of reactive wetting were investigated by conducting measurements on structures of varying track width. The dependency of the spreading distance and contact angle on size was investigated for characteristic lengths ranging from 3 mm down to ~100 µm. The contact angles demonstrated non-ideal behavior,

increasing with decreasing track width. Furthermore, by modifying Young's equation, it was found that the contact angle size dependency could be well described by an effective triple line energy of $\epsilon_t = (753 \pm 31) \times 10^{-9}$ J/m for eutectic SnPb on electrodeposited Cu.

To clarify the cause of the observed effective triple line energy and general non-ideal wetting behavior, additional experiments were conducted on flat unstructured substrates of both smooth polished and rough electroplated surface finish. In these experiments, pure Sn solder was used and the size dependency was tested by varying the solder volume rather than the structural dimensions of the substrate. Nonetheless, in the case of the rough substrates, similar trends were observed to those of the structured "lollipop" samples. These trends were quantified using the so-called "excess capillary energy" approach. If was found that the smaller excess capillary energy per line length of smaller droplets could well describe the observed increase in CA with decreasing droplet size. Remarkably, for the smooth polished case, the contact angles were found to decrease with decreasing solder radius. This proved that it is the inherent surface roughness of the substrate, not the intermetallic roughness, which is the predominant factor causing hysteretic reactive wetting. The trend for the smooth substrate case was attributed to both the loss of droplet volume (caused by intermetallic formation and the formation of so-called "halo" regions) and the dynamic roughening associated with the formation of intermetallic at the substrate near the triple line. This shift in surface roughness may have caused a shift in the capillary equilibrium according to the concept of Wenzel, resulting in a contact angle reduction for smaller solder volumes.

Finally, spreading kinetics were investigated for (i) Sn_4Pb_6 and Sn_3Pb_7 on smooth Cu substrates of the "lollipop" geometry and (ii) Sn_4Pb_6 on equivalent structured substrates except with a pretreated Cu_6Sn_5 surface finish which was formed by reaction in molten Sn and exposed via etching of the residual Sn with HCl. The particular solder alloy compositions of the first investigation were selected for their preferential formation of Cu_6Sn_5 and Cu_3Sn at 350 °C respectively. By this means, the dependence of flow kinetics on the rate of intermetallic formation could be studied. The second investigation offered a useful comparison, whereby the rate-limiting reaction step of reactive spreading was removed. Faster spreading was observed on the pre-reacted substrate.

Kurzfassung

Die Mikroelektronikindustrie treibt die Bemühungen voran, Lötstellen kontinuierlich zu miniaturisieren. In diesem Zusammenhang dürfen jedoch andere Verbindungseigenschaften wie die Verbindungsfestigkeit nicht beeinträchtigt werden. Üblicherweise werden Benetzungswinkel als Indikator für die Stärke einer Lötverbindung verwendet. Nichtsdestotrotz ist die Adhäsionsarbeit eigentlich eine genauere Darstellung der Bindungsstärke. In dieser Arbeit bestimmen wir die Kontaktwinkel für SnPb und SnPb-Lotlegierungen auf polierten Cu- und Ni-Substraten in einer Sessile-Drop-Geometrie unter äquivalenten Messbedingungen über ihren gesamten Zusammensetzungsbereich bei 350 °C und 500 °C. Auch wurden Oberflächenspannungen für beide Lotlegierungen für alle Zusammensetzungen bei beiden Temperaturen bestimmt. Aus diesen Rohergebnissen kann die experimentelle Adhäsionsarbeit über die Young-Dupre-Gleichung bestimmt werden, die die Adhäsionsarbeit mit dem Kontaktwinkel und der Oberflächenspannung in Beziehung setzt. Die Zusammensetzungsabhängigkeit der Adhäsionsarbeit entspricht der thermodynamischen Stabilität der Produktphase/n. Auch die Existenz der erwarteten intermetallischen Phasen wurde über REM-Aufnahmen und EDX-Untersuchungen kontrolliert. Dieses Ergebnis bestätigt das Konzept von Eustathopoulos, das besagt, dass sich die reaktive Ausbreitungstripellinie auf der Produktphase mit der höchsten Sn-Konzentration equilibriert. Schließlich hat die thermodynamische Modellierung der Adhäsionsarbeit gemäß dem Ansatz von Butler sowohl auf eine signifikante Segregation von Sn an der reaktiven Fest-Flüssig-Grenzfläche als auch auf eine Pb/Bi-Segregation an der Flüssigkeitsoberfläche hingewiesen.

Es ist allgemein bekannt, dass Kapillarkräfte bei kleineren Flüssigkeitsvolumen vorherrschender werden. Dennoch ist das Benetzungsverhalten von reaktiven Lötstellen in Abhängigkeit vom Lotvolumen nicht gut verstanden. Hier untersuchen wir reaktive Benetzungsgleichgewichte auf eutektischem SnPb-Lot auf Cu-Proben mit eingeschränkter Geometrie. Die Cu-Proben wurden durch einen Prozess der Laserschreiblithographie und Elektroabscheidung hergestellt

und bestanden aus einem kreisförmigen Pad, an dem eine lange gerade Leiterbahn angebracht war, die die geometrische Form eines „Lollipop“ annahm. Bei dieser Geometrie benetzt eine auf dem Pad geschmolzene Lotkugel zuerst das Pad und breitet sich dann entlang der Leiterbahn aus. Größenabhängigkeiten der reaktiven Benetzung wurden durch Messungen an Strukturen unterschiedlicher Leiterbahnbreite untersucht. Die Abhängigkeit der Ausbreitungsdistanz und des Kontaktwinkels von der Größe wurde für charakteristische Längen im Bereich von 3 mm bis hinunter zu ~100 µm untersucht. Die Kontaktwinkel zeigten ein nicht ideales Verhalten und nahmen mit abnehmender Spurbreite zu. Darüber hinaus wurde durch Modifizieren der Young’sche Gleichung festgestellt, dass die Abhängigkeit der Kontaktwinkelgröße für eutektisches SnPb auf galvanisch abgeschiedenem Cu durch eine effektive Tripellinienenergie von $\epsilon_t = (753 \pm 31) \times 10^{-9}\,\mathrm{J/m}$ gut beschrieben werden kann.

Um die Ursache der beobachteten effektiven Tripellinienenergie und des allgemeinen nicht idealen Benetzungsverhaltens zu klären, wurden zusätzliche Experimente an flachen unstrukturierten Substraten mit sowohl glatt polierter als auch rauer galvanisierter Oberflächenbeschaffenheit durchgeführt. Bei diesen Experimenten wurde reines Sn-Lot verwendet und die Größenabhängigkeit wurde getestet, indem das Lotvolumen, und nicht die strukturellen Abmessungen des Substrats, variiert wurde. Dennoch wurden bei den rauen Substraten ähnliche Trends wie bei den strukturierten „Lollipop“-Proben beobachtet. Diese Trends wurden mit dem sogenannten „excess capillary energy“-Ansatz quantifiziert. Es wurde festgestellt, dass die geringere überschüssige Kapillarenergie pro Linienlänge kleinerer Tröpfchen die beobachtete Zunahme der CA mit abnehmender Tröpfchengröße gut beschreiben könnte. Bemerkenswerterweise wurde für das glatt polierte Gehäuse festgestellt, dass die Kontaktwinkel mit abnehmendem Lötradius abnahmen. Dies bewies, dass es die inhärente Oberflächenrauhigkeit des Substrats ist, nicht die intermetallische Rauhigkeit, die der vorherrschende Faktor ist, der bei reaktive Benetzung Hysterese verursacht. Der Trend für den Fall des glatten Substrats wurde sowohl dem Verlust an Tröpfchenvolumen (verursacht durch intermetallische Bildung und die Bildung sogenannter „Halo“-Bereiche) als auch der dynamischen Aufrauung zugeschrieben, die mit der Bildung von intermetallischen Phasen am Substrat in der Nähe der Tripellinie verbunden ist. Diese Verschiebung der Oberflächenrauhigkeit könnte nach dem Konzept von Wenzel zu einer

Verschiebung des Kapillargleichgewichts geführt haben, was zu einer Verringerung des Kontaktwinkels bei kleineren Lotvolumen führt.

Schließlich wurde die Ausbreitungskinetik untersucht für: (i) Sn_4Pb_6 und Sn_3Pb_7 auf glatten Cu-Substraten der „Lollipop"-Geometrie und; (ii) Sn_4Pb_6 auf äquivalent strukturierten Substraten, zusätzlich mit einer vorbehandelten Cu_6Sn_5-Oberflächenveredelung, die durch Reaktion in geschmolzenem Sn gebildet und durch Ätzen des restlichen Sn mit HCl freigelegt wurde. Die speziellen Lotlegierungszusammensetzungen der ersten Untersuchung wurden aufgrund ihrer bevorzugten Bildung von Cu_6Sn_5 bzw. Cu_3Sn bei 350 °C ausgewählt. Auf diese Weise konnte die Abhängigkeit der Fließkinetik von der Geschwindigkeit der intermetallischen Bildung untersucht werden. Die zweite Untersuchung bot einen nützlichen Vergleich, wobei der geschwindigkeitsbegrenzende Reaktionsschritt der reaktiven Ausbreitung entfernt wurde. Auf dem vorreagierten Substrat wurde eine schnellere Ausbreitung beobachtet.

Table of contents

List of variables

Variable	Description	SI units
a	Droplet (spherical cap) base radius	[m]
A	Area	[m^2]
F	Capillary driving force for wetting	[J/m^2]
g	Acceleration of gravity	[m/s^2]
G	Gibbs capillary energy	[J]
δG	Excess Gibbs capillary energy	[J]
$\delta \tilde{G}$	Excess Gibbs capillary energy per line length	[J/m]
h	Height	[m]
Δp	Laplace pressure	[N/m^2]
r	Droplet (spherical cap) radius of curvature	[m]
r_p	Pad radius (structured substrates experiment)	[m]
R_p	Radius of droplet on pad (structured substrate experiments)	[m]
R_s	Radius of droplet on strip (structured substrate experiments)	[m]
R	Wenzel's roughness parameter	[-]
s_f	Spreading distance	[m]
U	Triple line pinning energy barrier	[J/m]
W_a	Work of adhesion	[J]
γ_{sv}	Solid-vapor surface energy	[J/m^2]
γ_{lv}	Liquid-vapor surface energy	[J/m^2]

γ_{sl}	Solid-liquid interface energy	[J/m^2]
δ	Strip width (structured substrates)	[m]
ϵ_t	Triple line energy	[J/m]
$\Delta\theta$	Contact angle hysteresis ($\theta_a - \theta_r$)	[°]
θ_0	Equilibrium contact angle	[°]
θ_a	Advancing contact angle	[°]
θ_{ap}	Apparent contact angle	[°]
θ_c	Cassie's contact angle	[°]
θ_f	Front contact angle (structured substrate experiments)	[°]
θ_i	Intrinsic contact angle	[°]
θ_p	Pad contact angle (structured substrate experiments)	[°]
θ_r	Receding contact angle	[°]
θ_s	Strip contact angle (structured substrate experiments)	[°]
θ_w	Wenzel's contact angle	[°]
θ_y	Young's contact angle	[°]
ρ	Density	[kg/m^2]
σ_{sv}	Solid-vapor surface tension	[N/m]
σ_{lv}	Liquid-vapor surface tension	[N/m]
σ_{sl}	Solid-liquid interface tension	[N/m]
τ	Effective intermetallic thickness	[m]

List of abbreviations

AFM	Atomic force microscopy
BSE	Backscattered electron
CA	Contact angle
CAH	Contact angle hysteresis
EBSD	Electron-Backscatter-Diffraction
EDX	Energy-dispersive X-ray spectroscopy
HT	High temperature
IMC	Intermetallic compound
LT	Low temperature
SE	Secondary electron
SEM	Scanning electron microscope
TL	Triple line

1 Introduction

During recent decades the microelectronics industry's ambition to achieve ever higher information processing density has motivated a ceaseless drive for solder joint miniaturization while reconciling the necessity for improved solder joint stability. This economic drive, as well as inherent fundamental scientific interest, inspires ongoing research aimed at improving the scientific community's fundamental understanding of the processes involved in solder micro-joining. Although soldering is a process also used for bonding metal structural components (where welding is unfavorable), they also are required ubiquitously in the electronics industry, from the soldering of fundamental electronic components on through-pin PCBs (e.g. in small household appliances) to the small micro-dots joining microchips and PCBs in the packaging of high processing density devices (mobile phones, laptops, etc.). Solder alloys act as a conductive "glue" between electronic components allowing the flow of power or information (binary bits). Tin is the most commonly used base alloy component due to its low melting point, good wettability, and reactivity with metals commonly used in electronic devices (e.g. Cu, Ni). Nonetheless, pure tin solder joints are not applied in an industrial context, because they are prone to whisker formation which can cause short-circuits and reduce joint reliability. Before 2006, lead was the most common alloying component; eutectic SnPb solder offers the lowest melting point, has improved wettability, and suppresses whisker formation. But since 2006, due to the toxicity of lead, EU guidelines disallowed its use in commercial products. Consequently renewed scientific efforts have been aimed at finding alternatives to lead-based solders. Other common alloying elements include Bi, In, Sb, Zn, Ag, Cu which are chosen depending on the requirement of the application (preferred temperature or mechanical stability, wettability, melting point, etc.). The property of good wetting is crucial for most soldering processes. Here wettability is understood as the tendency of a liquid to spontaneously spread over a solid surface. This is necessary so that the molten solder coats and forms a reactive bond with the entire joint for maximum stability. Generally, wetting can be separated into the categories: non-reactive wetting and reactive wetting. Non-reactive wetting encompasses all inert wetting systems which are controlled solely by physical

phenomena such as surface and interface energies, surface chemical and physical heterogeneity, solid elasticity, and surface absorption. Reactive wetting systems are more complex, being influenced by both physical phenomena as well as the chemical reaction occurring between the reactive liquid and substrate. It is precisely this complexity that has caused the analytical description of reactive wetting processes to remain elusive.

Of course, a complete analytical description would provide the ability to predict the outcome of reactive wetting processes, including both reactive wetting kinetics and the final equilibrium state. This could vastly improve the efficiency for improving existing and developing new solder joint technologies. For this reason research on reactive wetting behavior has continued throughout past decades and recent years. In past decades, seminal works include those of Eustathopoulos and Yost who separately conceptualized contrasting models describing the kinetics of reactive wetting.

1.1 Scope of this work

This work aims to:

1. Corroborate existing, yet inconclusive concepts in reactive wetting science, in particular regarding the relationship between contact angle, adhesion strength, and product phase formation (**chapter 4**).
2. Find and apply an accurate thermodynamic predictive model describing the work of adhesion of reactive solder joints (**chapter 4**).
3. Through various experiments using both structured and unstructured solderable substrates, quantify the relationship between reactive wetting equilibria and reactive solder joint size (**chapter 5**).
4. Provide a phenomenological explanation for any observed size/surface effects, and describe how these effects relate to the driving force of reactive spreading (**chapter 5**).
5. Investigate the relationship between reactive spreading kinetics and intermetallic formation (**chapter 6**).

2 Material physical background

2.1 Properties of surfaces and interfaces

2.1.1 Surface tension

Surfaces are often described as imperfections due to the addition of energetic broken bonds (solids) or lower coordination (liquids) compared to bulk material. Consequently, surfaces of liquids and solids have associated excess energy which is quantified per unit area. This excess energy, also called surface energy can be understood similarly for solids and liquids, although it more commonly used in the context of solids. The surface energy γ is the work W required to stretch the surface area A by a small amount.

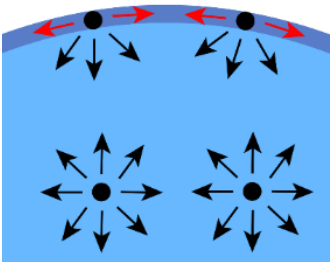

Figure 2.1: Surface tension experienced by water molecules. Molecules at the surface of a liquid body experience anisotropic intermolecular interactions causing a net force towards the bulk.

$$\gamma = \frac{\delta W}{\delta A} \tag{1}$$

In a liquid, atoms (the following theoretical explanations can also be applied to molecules) exhibit cohesive forces on each other causing them to remain as a single body. These cohesive forces are isotropic in the liquid bulk, but at the discontinuous surface, this is not the case. Surface atoms experience both inward cohesive forces causing the liquid to be under hydrostatic pressure and lateral cohesive forces causing the surface to be under tension (see Figure 2.1). These anisotropic surface forces give rise to the term surface tension. Unlike surface energy, surface tension σ, is typically used when describing liquids and is defined as the force F acting parallel to a liquid surface per length l.

$$\sigma = \frac{F}{l} \tag{2}$$

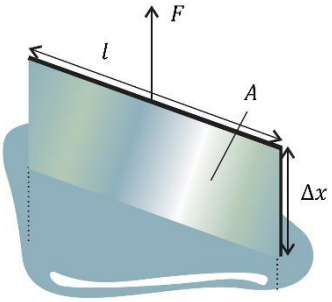

Figure 2.2: Exemplary surface tension experiment [1].

Unlike a solid, as the surface of a liquid is stretched, atoms from the bulk flow to the surface filling the newly formed area, resulting in a constant atomic surface density. For this reason, surface tension and surface energy are both constant properties of liquids (where pressure and temperature are also constant). Now consider a simple experiment where an infinitely thin wire is placed in contact with a body of water and then pulled to a height x forming a thin film of liquid (see Figure 2.2). It can be shown mathematically that surface tension is equivalent to surface energy.

$$2\sigma = \frac{F}{l} = \frac{F}{l}\frac{\Delta x}{\Delta x} = \frac{W}{A} = 2\gamma \tag{3}$$

Here, the factor 2 is a consequence of the two surfaces formed in the experiment. The main consequence of surface tension and the continuous nature of liquids is that liquid bodies tend to minimize their surface area. Droplets on a flat surface for example tend to become more spherical.

2.1.2 Young-Laplace pressure

The inward pressure applied by surface atoms causes a pressure difference across the surface. This can be easily exemplified thermodynamically for a spherical droplet. Consider first the Helmholtz Free Energy F for a droplet [2].

$$dF = -SdT - pdV + \sigma dA \tag{4}$$

Here S is entropy, T is temperature, p is pressure, V is volume, and A is surface area. In equilibrium and for a system with constant temperature it follows that:

$$dF = -pdV + \sigma dA \tag{5}$$

The consequence of this formula is that the Helmholtz Energy decreases with volume, but increases with surface area. For a system in equilibrium, these two energy terms must be balanced.

$$pdV = \sigma dA \tag{6}$$

Taking the derivative of the volume and surface area and then simplifying yields

$$p \cdot 4\pi r^2 dr = \sigma \cdot 8\pi r dr \tag{7}$$

$$\Delta p = \frac{2\sigma}{r} \tag{8}$$

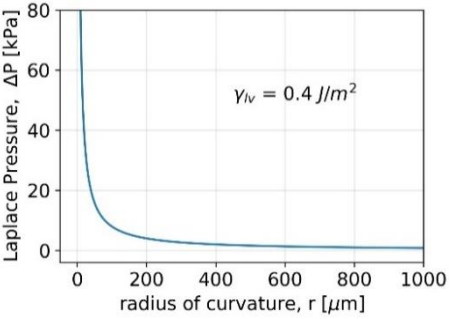

Figure 2.3: Laplace pressure of a spherical droplet with surface tension $\gamma_{lv} = 0.4\ \mathrm{J/m^2}$ as a function of a spherical cap droplet radius of curvature.

Where $\Delta p = p_{concave} - p_{convex}$ is the difference in pressure between the concave interior and convex exterior of the droplet (or bubble) surface and is commonly named the Laplace pressure. The consequence of this equation is that as droplets decrease in radii, Δp can become very large and thus the surface tension causes droplets to become significantly less stable at smaller sizes. The impact of surface tension for small droplets is depicted in Figure 2.3. Furthermore by deriving the pressure difference instead for a curved surface with two radii of curvature, $r_1 \neq r_2$, one arrives at a more general form of equation (8) which is called the Young-Laplace equation.

$$\Delta p = \gamma \left(\frac{1}{r_1} + \frac{1}{r_2} \right) \tag{9}$$

2.1.3 Capillary action

When a liquid body comes into contact with a solid surface, it may spontaneously spread or recede across the solid surface without the application of any external forces (eg. gravity, external pressure). This effect is called capillary action and is a consequence of surface and interface tensions, which due to the physical interactions between atoms of the liquid and solid, do spontaneous work lowering the system free energy. In other words, capillary action is a surface/interface phenomenon, which is typically the dominant force controlling the fluid dynamics of solid-liquid systems with sufficiently small liquid volumes relative to the solid-liquid and liquid-vapor interface areas (e.g. water droplets, absorbent sponges). A hollow cylinder (tube) is a useful system to exemplify the process of capillary action. They can be found in both macroscopic applications (thermometers), and throughout microporous systems.

When a glass tube is partially submerged in a body of liquid, the liquid will either climb up or recede down the tube walls. If the adhesive forces between the atoms of the liquid and glass are stronger than the cohesive forces between liquid atoms, the liquid will climb. The opposite is true for stronger cohesive forces. In the case of a glass tube in water (re. Figure 2.4a), the water will climb the tube walls resulting in a meniscus forming with a pressure difference across the meniscus as defined by equation (8). Here the radius of the meniscus—which directly relates to the Laplace pressure—is dependent first on the tube radius, a, but also on the balancing of the transverse components of the liquid/vapor surface tension σ_{lv}, solid/vapor surface tension σ_{sv}, and solid/liquid interface tension σ_{sl} (re. Figure 2.4b), and forming the equilibrium wetting angle θ_0.

$$0 = \sigma_{sv} - \sigma_{sl} - \sigma_{lv}\cos\theta_0 \tag{10}$$

Equation (10) is more commonly written in terms of the angle,

$$\cos\theta_y = \frac{\sigma_{sv} - \sigma_{sl}}{\sigma_{lv}} \tag{11}$$

Which is known as Young's equation and where the Young's contact angle $\theta_y = \theta_0$ is the equilibrium contact angle in the ideal state. The equilibrium height of the meniscus in the tube is controlled by the hydrostatic constraint that the liquid

pressure is constant for any given height within a single liquid body. The height dependence of hydrostatic pressure ΔP_h is given by

$$\Delta P_h = hg\rho \tag{12}$$

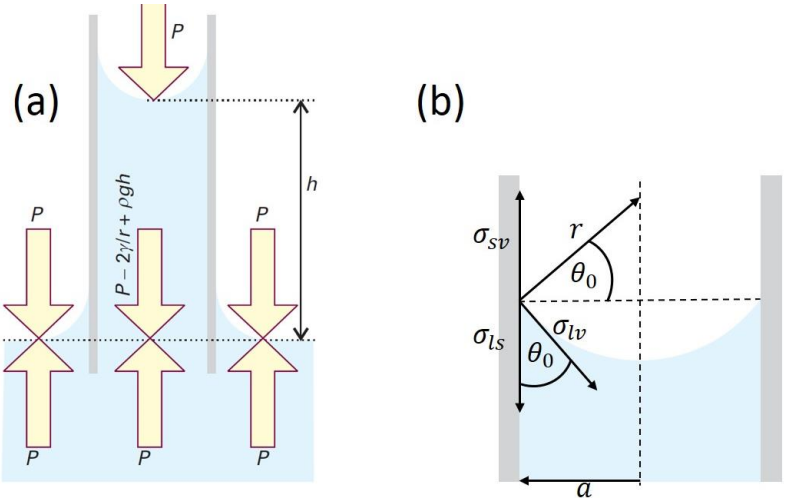

Figure 2.4: (a) Capillary action depicted for water in a partially submerged glass tube [1]. (b) The wetting contact angle is defined by the balance of the capillary forces at the meniscus three-phase triple line.

Where g is the acceleration of gravity and ρ is the liquid density. In equilibrium, the balance of the hydrostatic and Laplace pressures gives:

$$hg\rho = \frac{2\gamma}{r} = \frac{2\gamma \cos\theta_0}{a} \tag{13}$$

The main consequences of equation (13) are first, the liquid height magnitude is most significantly influenced by the tube radius and secondly, the direction of the movement in the tube is controlled by sign of the $\cos\theta_0$ term. For $\theta_0 < 90°$ the liquid will rise and for $\theta_0 > 90°$ the liquid will fall.

2.2 Equilibrium Wetting

Wetting is generally defined as the capability of a liquid to adhere to a solid surface due to intermolecular or interatomic interactions. Figure 2.4 offers an example of wetting where water is climbing or "wetting" the glass tube. The following sections will describe equilibrium wetting phenomena more closely, including important definitions required to distinguish between contrasting wetting systems. Furthermore, for simplicity and relevance, only planar solid surfaces will be discussed here forth.

2.2.1 Work of adhesion

Research on wettability is often driven by the goal of better understanding the adhesive (or lack thereof) properties between a liquid and solid. The adhesion tension or work of adhesion W_a describes the thermodynamic bonding strength of a joint between two phases and is defined by the Dupre equation as the work required to separate two phases from each other per unit area.

$$W_a = \sigma_{sv} - \sigma_{sl} + \sigma_{lv} \tag{14}$$

For a liquid-solid two-phase wetting system, combining equations (11) and (14) yields the Young-Dupre equation:

$$W_a = \sigma_{lv}(1 + \cos\theta_0) \tag{15}$$

Consequently, to quantify the work of adhesion for a system, at the very least both the contact angle and the liquid surface tension must be determined. This happens to be the simplest approach to calculate W_a since the right side of equation (14) contains solid interface tensions which are not easily measured. Finally, although the work of adhesion is the most accurate quantification of a wetting joint's stability, it is not always necessary or practical to determine the surface tension (or interface tensions for that matter). Instead, the wettability of a system is often judged solely by the magnitude of the resulting SLV (solid-liquid-vapor) contact angle, or more precisely the wetting angle.

2.2.2 Sessile drop method

The most common method for measuring wetting angles is the sessile drop method.

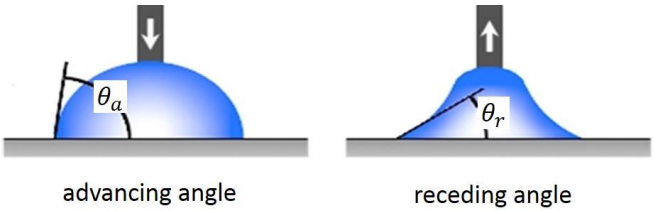

Figure 2.5: The sessile drop method for wetting angle determination. The advancing and receding contact angles are determined by adding (Left) and removing (Right) liquid to and from the substrate. Image adapted from [3].

The measurement process is simple: liquid is transported close to the surface of a substrate via a feeding tube with a syringe tip; the liquid is slowly ejected onto the substrate; a CCD camera images the silhouette of the droplet which is backlit by a lamp; the wetting angle it determined from the image. Both advancing and receding contact angles can be determined with the sessile drop method (see Figure 2.5). By continuously ejecting liquid onto the substrate the droplet will eventually begin to spread outwards and θ_a can be recorded. By drawing the liquid back into the tube, the liquid will eventually recede and θ_r can be recorded.

2.2.3 Ideal wetting

For a system to exhibit ideal wetting, the solid surface must be infinitely rigid, atomically smooth, chemically homogeneous, non-absorbent, and non-reactive. Additionally, to attain meaningful contact angle measurements, gravitational forces must be negligible. An ideal system exhibits only a single stable equilibrium contact angle, although meeting every condition for ideal wetting is of course practically unachievable. Consequently, all real wetting systems will behave non-ideally (to varying degrees) and exhibit a range of meta-stable contact angles (more on this in section 2.3.1). Nonetheless, the theoretical ideal system offers a strong foundation to build on and can be used as an approximation in some cases.

An ideal contact angle can be described by Young's equation (11) since only the competing surface and interface tensions control the spreading and final

equilibrium of the liquid droplet. Here, the term "spreading" is loosely used to mean, the advancing (outward) movement of a droplet triple line. In other studies, "spreading" is sometimes defined as perfect wetting ($\theta = 0°$), although this is not the case throughout this work. Considering a small droplet on an ideal substrate, the Young's contact angle is measured directly at the solid-liquid-vapor triple junction. Contact angles can range from 0° – 180° and for convenience, the wettability is categorized based on discrete ranges of contact angles. For contact angles below and above 90° the systems are said to be wetting and dewetting, respectively (see Figure 2.6). Furthermore in the extreme cases: a contact angle of 0° is said to be perfectly wetting which occurs when $\sigma_{sv} - \sigma_{sl} \geq \sigma_l$; conversely a contact angle of 180° where $\sigma_{sl} - \sigma_{sv} \geq \sigma_{lv}$ is described as completely dewetting.

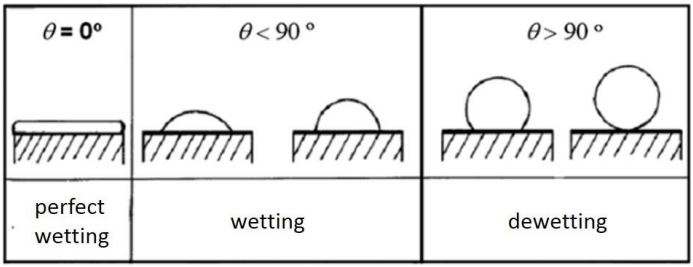

Figure 2.6: Different wetting states are depicted. The perfect wetting case is sometimes also called the spreading case. Figure adapted from [4].

2.2.4 Non-ideal wetting

Non-ideal wetting is defined as any deviation from Young's wetting theory. In literature, non-ideal wetting is generally attributed either to roughness or chemical heterogeneity of the wetted surface, although other cases exist [5]. These two contributions to non-ideal, equilibrium wetting behavior will now be discussed separately.

2.2.5 Wenzel's roughness model

The first notable advancement in understanding the wetting behavior of rough surfaces came from Robert Wenzel who introduced the roughness parameter R which represents the ratio of the true surface area to the projected surface area.

The roughness parameter essentially accounts for the increase in solid/vapor and solid/liquid interface tensions because of the increased surface area and can be included in Young's equation as a correction. The theoretical angle resulting from this model is called the Wenzel angle θ_w which is valid for an ideal rough wetting system in equilibrium.

$$\cos\theta_w = R\cos\theta_0 = R\frac{\sigma_s - \sigma_{sl}}{\sigma_l} \tag{16}$$

The main consequence of Wenzel's model is that for a given system, roughening of the substrate surface will cause wetting systems ($\theta_0 < 90°$) to wet better and dewetting systems ($\theta_0 > 90°$) to exhibit stronger dewetting. Although theoretically instructive, Wenzel's model is limited to describing equilibrium contact angles. In practice, equilibrium contact angles on rough surfaces are rarely achieved as will be discussed in section 2.3.1.

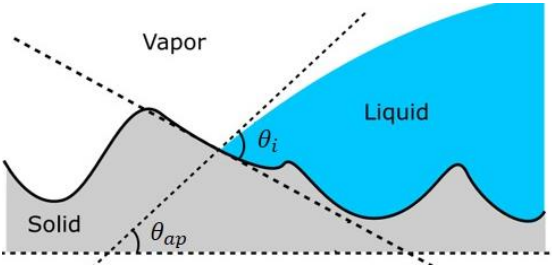

Figure 2.7: Depiction of a rough wetting surface, adapted from [6]. The intrinsic contact angle θ_i is governed by Young's equation at the microscopic scale. The apparent contact angle θ_{ap} is the macroscopically measured contact angle and depends on several factors which effect non-ideal wetting.

The precise definition of contact angles is imperative when considering non-ideal surfaces. For a rough surface, the microscopic angle formed at the triple line between a liquid surface and rough solid interface is called the intrinsic contact angle θ_i and is defined by the balance of the three interface tensions (see Figure 2.7). Conversely, the contact angle formed between the liquid and the projected average surface height is called the apparent contact angle θ_{ap}.

2.2.6 Cassie's composite rule

A composite wetting system is one with a chemically heterogeneous solid substrate. Cassie [7] first postulated composite (or Cassie) contact angles, θ_c, defined as the summation of the cosine of the contact angles on the individual solid-substrate-phases weighted by the partial surface areas of each phase.

$$\cos(\theta_c) = \sum_{i=1}^{N} f_i \cos(\theta_j) \tag{17}$$

Here f_i is the partial surface area and θ_j is the contact angle of component j. Cassie's rule which only considers area fractions and equilibrium contact angles of pure phases is applicable for both smooth and rough surfaces, so long as the equilibrium contact angles are known. Furthermore, there are cases where Cassie's rule is applied to chemically homogeneous wetting systems with synthetic, periodic, steep rough surfaces. For example, a surface comprising an array of micro-pillars may be considered a composite surface, insofar as a droplet sitting on the pillars shares different interface energies with the pillar tops compared with the air pockets. Of course, this assumes that the air pockets remain unfilled. Per convention, the filling of such air pockets from a droplet that initially lay to rest above them is called the Cassie-Wenzel transition and is a topic of some interest [8,9], but will not be further discussed here.

2.3 Non-equilibrium wetting

2.3.1 Wetting hysteresis

In the previous two sections, we have learned that equilibrium wetting angles on otherwise ideal rough or heterogeneous substrates can be thermodynamically described by Wenzel and Cassie's equations. But numerous findings have shown that wetting systems often demonstrate not one, but a range of metastable wetting angles, ranging from the so-called advancing contact angle to the receding contact angle [10–12]. This contradicts the simple and largely accepted concepts of Wenzel and Cassie and throws into question the extent to which equations (16) and (17) are applicable. The advancing angle, θ_a, is the maximum wetting angle formed as a droplet spreads outwards. Conversely, the receding contact angle, θ_r, is the minimum wetting angle formed as a droplet recedes inwards. Alternatively,

for a droplet on an inclining surface, θ_a and θ_r are respectively the maximum and minimum contact angles formed at the front and back of the droplet before the droplet slides (see Figure 2.8). The difference between the advancing and receding angles $\Delta\theta$, is called contact angle hfysteresis (CAH).

$$\Delta\theta = \theta_a - \theta_r \tag{18}$$

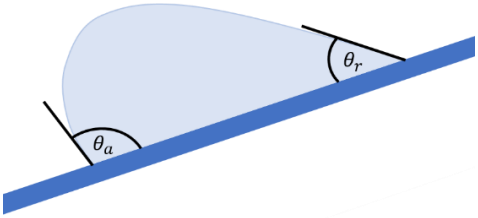

Figure 2.8: Depiction of contact angle hysteresis, where a wetted surface is continuously tilted. The advancing and receding (maximum and minimum) contact angles are determined at the front and back of the droplet the moment before the droplet begins to slide.

But why does CAH occur? Take the following example: a spherical cap droplet on a non-ideal, rough surface exists initially in an unstable non-equilibrium state and satisfies $\theta > \theta_a$. In this case, the unbalanced surface and interface tensions will drive the triple line to advance in an attempt to satisfy Young's equation. The droplet will spread until the triple line eventually pins (ceasing to advance), at which point the system remains in a meta-stable state where $\theta = \theta_a$. The general phenomenon where a spreading triple line ceases to advance before reaching equilibrium is called triple line pinning and is generally attributed to morphological or chemical energy barriers. In other words, it is generally claimed (although vaguely) that rough and chemically heterogeneous surfaces tend to pin droplets in position, whether they are advancing or receding, as long as $\theta_a > \theta > \theta_r$. This is of course quite a vague definition, and although wetting hysteresis is well documented [13,14], the decisive phenomena which cause it are complex. Consequently, a universally predictive description for advancing/receding wetting angles or contact angle hysteresis remains elusive. Thus, research on and debate concerning the precise cause of CAH, as well as the limits of Wenzel and Cassie's equations, continues [15–18].

2.3.2 Huh and Mason Model

Before continuing our discussion on the shortcomings of Wenzel's and Cassie's concepts, it is worth taking a look at an instructive theoretical wetting model by

Huh and Mason. For rough surfaces, the model of Huh and Mason offers an insightful initial look at how a periodically undulating (i.e. artificially rough) surface influences the apparent CA [19]. They investigate the apparent contact angle of a liquid droplet of varying radius on a 2-dimensional sinusoidal perpendicular cross-grooved surface (see inset in Figure 2.9). Their nearly smooth perturbation model has the following conditions: (i) The Young-Laplace condition is satisfied by the droplet; (ii) along the contact line, the equilibrium CA θ_0 exists; (iii) volume is conserved; (iv) within these constraints, they determine the apparent contact angle θ as:

$$\cos(\theta) = \cos(\theta_0) + \frac{\omega l_d}{R}\left(xJ_1(x) + J_0(x)\right), \qquad x = \frac{\pi R \sin(\theta_0)}{l_d} \tag{19}$$

where J_0 and J_1 are the zeroth and first-order Bessel functions, ω is the ratio of sinusoidal (defect) amplitude to wavelength, l_d is the sinusoidal defect half-wavelength, and R is the droplet radius.

The sinusoidal cross-grooved surface model of Huh and Mason is the logical best starting point for investigating size dependencies of CAs on rough surfaces since it represents the simplest theoretical 2-dimensional periodic surface. Simpler 1-dimensional models (including those with radial symmetry, c.f. [19]) do not manifest size dependencies. Furthermore, as mentioned by the authors briefly, their results very much resemble size dependent contact angle hysteresis. Although their model does not strictly evaluate hysteretic effects (i.e. their CA results are independent of the path taken by the droplet), the periodicity of the model results in an increase in fluctuations between maximum and minimum CAs as the droplet radius

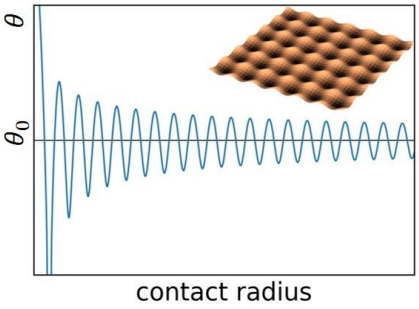

Figure 2.9: Solution of the model of Huh and Mason who investigated the relationship between drop size and drop contact angle on a 2-dimensional perpendicular sinusoidal cross-grooved surface (see inset) [19].

decreases (see Figure 2.9). Since CAH is defined as the difference between θ_a and θ_r, which are by definition maximum and minimum values, we may consider the results of Huh and Mason to mimic contact angle hysteresis at least approximately.

2.3.3 Where Wenzel and Cassie were wrong

Although wetting hysteresis has been studied for decades [20,21], it was only in the 21st century that a deeper discussion around the discrepancies between Wenzel's and Cassie's concepts and wetting hysteresis began. For example, a study by Extrand [22] found that, for a droplet placed directly over a single chemically heterogeneous island on an otherwise homogeneous surface, if the heterogeneity was completely contained within the droplet perimeter, then the droplet demonstrated CAH as if there were no island heterogeneity. In a similar study by Gao and McCarthy [23], they found that for a single smooth spot in a rough field and a single rough spot in a smooth field, a droplet covering either spot would exhibit CAH independent of the rough/smooth area portions. So long as the droplet perimeter extended beyond the heterogeneous spot, the droplet would exhibit CAH as if the heterogeneous spot was non-existent. But others argue [24,25] that the equations of Wenzel and Cassie have been wrongly applied in these instances and that they are simply extensions of the capillary energy balance (Young's equation) at the triple line. In this way, they correctly argue that Wenzel's and Cassie's concepts should not be used to describe heterogeneities within the perimeter of a droplet. Rather they claim that Cassie's equation is valid when considering the area fractions under the triple line and that Wenzel's equation is similarly only valid when considering the roughness under the triple line. In the end, the whole discussion surrounding the observations of Extrand and Gao and McCarthy is largely a matter of semantics. What is clear, is that the observed wetting angle of a droplet on a substrate is controlled by the activation energy required for the triple line to move from one configuration to the next (hysteresis). Furthermore, it is highly likely that, for a macroscopic droplet placed either (i) on a surface of nanoscopic 2-phase heterogeneities or (ii) on a nanoscopic rough surface, the wetting driving force would be controlled by (i) the area fractions of the 2-phase regions or (ii) the surface roughness ratio (non-hysteretic).

2.3.4 Stick-slip phenomenon

The stick-slip wetting phenomenon is observed when the triple line of a wetting droplet remains static for extended periods but occasionally exhibits abrupt movements. This can for example occur when a static droplet on a solid surface gradually evaporates. Assuming the triple line of a droplet is pinned ("stick" case), as the droplet volume decreases due to evaporation, the CA necessarily decreases also. Eventually, the CA decreases to the minimum receding angle θ_r at which time the triple line overcomes the pinning energy barrier and "slips" (recedes), manifesting a new reduced contact radius with a new CA, $\theta > \theta_r$. The stick-slip phenomenon can be evaluated as a technique for determining pinning energy barriers, as has been outlined by Shanahan [26,27]. First, the capillary Gibbs free energy, *G*, of a circular symmetric droplet is given by

$$G = \gamma_{lv}\pi a^2 \left(\frac{2}{1+\cos\theta} - \cos\theta_0\right) \tag{20}$$

Where γ_{lv} is the surface energy, a is the contact radius, and θ_0 is the equilibrium CA, and θ is the measured, non-equilibrium CA. The absolute excess Gibbs free energy, i.e. the difference between the Gibbs energy of the measured and equilibrium states, δG, is calculated as $\delta G = G(a) - G(a_0)$, where a_0 is the equilibrium contact radius. Normalizing by the triple line length, $2\pi a$, yields the excess Gibbs free energy per line length $\delta\tilde{G}$.

$$\delta\tilde{G} = \frac{G(a) - G(a_0)}{2\pi a} \tag{21}$$

Now, as the pinned droplet evaporates, $\delta\tilde{G}$ gradually increases until the triple line slips. It should however be noted that the triple line does not slip into the equilibrium configuration, but rather somewhere between the "stick" (θ_r) and equilibrium (θ_0) configurations. Unfortunately, the lack of a thermodynamically well-defined "slip" contact angle makes it difficult to compare measurements accurately, as has been demonstrated by Bormashenko [28]. Fortuitously, as the volume of an evaporating droplet decreases, a critical contact radius, a_c, is typically reached, after which the droplet demonstrates severely reduced slip motion. This ultimate pinned state was proposed to be a consequence of the excess Gibbs free energy per line length decreasing below a critical value G_c, below which the droplet possesses insufficient energy to overcome the potential energy

barrier for depinning U. It would then follow that a droplet can no longer overcome the depinning energy barrier if the following condition is met,

$$G_c = \gamma_{lv}\pi a_c^2\left(\frac{2}{1+\cos\theta} - \cos\theta_0\right) \leq 2\pi a_c U \qquad (22)$$

Where U has units of energy per line length. It seems that there is a size dependence implied here, although it is only acknowledged, but not discussed in the works of Shanahan [26] and Bormashenko [28]. Finally, rearranging eq. (22), U may be approximated:

$$U \sim \gamma_{lv} a_c \left(\frac{1}{1+\cos\theta} - \frac{\cos\theta_0}{2}\right) \qquad (23)$$

Using this approach, Bormashenko [28] measured potential line energy barriers of $U \sim 1 \cdot 10^{-5}$ J/m for droplets of water on various polymer substrates. Shanahan [26] observed a similar result for ethanol on PTFE of $U \sim 1 \cdot 10^{-5}$ J/m . But it must be stressed that, although we have defined a final pinning state which remains approximately "stuck" as the droplet evaporates, in fact there still exists minor slip motion (at least after sufficient evaporation) which is neglected. The accuracy of eq. (23) should be judged accordingly. Finally, the present discussion of stick-slip hysteresis and triple line pinning is found within the context of a receding, evaporating droplet. One might however consider if the same excess Gibbs energy theory is better applied to the advancing wetting case, where the surface at the spreading triple line is not yet adulterated by the liquid (which is the case for receding experiments). By this method, one may more readily elucidate potential size dependencies of contact angle hysteresis.

2.3.5 Spreading: overcoming local energy barriers

Until now, we have discussed pinning and depinning energy barriers of hysteretic wetting systems with regular surface heterogeneities and comprising only surface and interface energy properties. Within this context, advancing or receding droplets will inevitably come to rest exhibiting a maximum, θ_a, or minimum, θ_r, CA. Now let us discuss irregular, "random" heterogeneous surfaces (e.g. real rough surfaces), the excess energy required to overcome local heterogeneities may vary vastly. Figure 2.10 depicts the influence of chemical and physical heterogeneities on the free energy diagram for the spreading of a 2-dimensional

(cylindrical) sessile drop [13]. Starting from the right of Figure 2.10 at $\theta = 80°$, the hypothetical droplet will spread, advancing as long as the slope of the free energy remains negative. Once the spreading droplet reaches $\theta = 70°$ the free energy slope becomes positive and the triple line is pinned in position unless external energy is supplied.

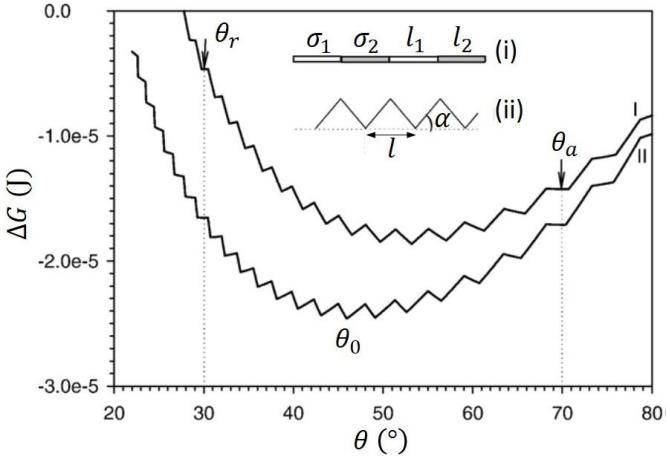

Figure 2.10: Depiction of energy barriers to the advancing/receding of a hypothetical 2D liquid droplet (altered version of the original graphic from Long et al [13]). Energy barriers are caused by (i) chemical heterogeneity and (ii) surface roughness. ΔG is the change in Gibbs free energy and θ is the droplet CA. The inset at the top of the figure exemplifies 2D surfaces with (i) chemical heterogeneities and (ii) periodic asperities, which would typically exhibit hysteretic behavior. The subscripted σ and l in inset (i) represent the surface tension and characteristic length of solid phases 1 and 2. In inset (ii) α and l represent the roughness angle and roughness wavelength. The two curves represent surface cases (i) and (ii), although they may be evaluated equivalently in this model.

Various causes of CAH have been demonstrated in literature. As previously addressed, surface roughness [28–31] and chemical surface heterogeneity [32,33] are the two most studied contributions to CAH. Moreover, the impact of these surface properties looks quite similar on the microscopic scale. In both cases, there are high energy and low energy microscopic (or nanoscopic) regions through which a spreading droplet must navigate. Naturally, the droplet triple line will seek the most energetically favorable path as it spreads. Take for example an advancing

wetting system ($\theta < 90°$): on a chemically heterogeneous surface the triple line will prioritize spreading over and eliminating high energy regions, and on a rough surface, the triple line will prioritize spreading through crevasses and troughs. On randomly heterogeneous surfaces, the "most energetically favorable path" may cause the droplet contact area to "more than slightly" deviate from a perfect circle, as is commonly observed.

Another phenomenon causing wetting hysteresis is surface reconstruction, or "ridge" formation at the triple line. Ridge formation at the droplet triple line has been reported to occur as a consequence of the substrate normal component of surface tension, which is otherwise ignored for rigid, inert substrates. More specifically, ridge formation, as demonstrated in literature, may occur in one of two scenarios: (i) the normal component of the surface tension σ_{lv} is sufficient to directly deform elastic substrates (e.g. elastomers) [5,34–37]; (ii) at sufficiently high temperatures, ridging of metal/ceramic wetting systems was reported to result from local diffusion or solution precipitation [38,39]. The relationship between surface reconstruction and CAH is quite different from that of rough or chemically heterogeneous surfaces. Pinning due to ridge formation at the triple line is by its nature a dynamic phenomenon, strongly linked to both the rate of triple line spreading and rate of ridge formation. Pinning on rough or chemically heterogeneous non-reactive surfaces is however independent of spreading rate.

Unfortunately, due to the complexity of the phenomenon causing CAH, no predictive model exists for the determination of θ_a or θ_r. Furthermore, no analytical link exists between θ_a, θ_r and θ_0. As a rule of thumb, the equilibrium CA can be approximated as $\theta_0 = (\theta_a + \theta_r)/2$, but relation should be applied cautiously since deviation from θ_0 may vary largely between advancing and receding contact angles [40]. Nonetheless, θ_a and θ_r can be readily determined as they represent the maximum and minimum angles a wetting system can attain. Strangely, it is the equilibrium contact angle, θ_0, which is most difficult to determine faithfully, in particular for strongly hysteretic systems. One method which can assist in determining θ_0 is by offering a source of acoustic vibrational energy. The effect vibrational energy has on CAH and equilibrium wetting has been studied previously [41–43]. Long et al. theoretically investigated the relationship between vibrational energy, pinning energy barriers, and CAH. They showed that, when vibration energy is supplied to a non-equilibrium droplet, it may be "bumped" into a lower energy state, approaching equilibrium (see Figure 2.10). It is although possible that, if an excess of vibrational energy is supplied, a

droplet may get bumped out of equilibrium and come to rest in a non-equilibrium state after the energy source is removed. Ironically, perhaps the most serious problem hindering the accurate measurement of θ_0, is that the equilibrium angle is a highly theoretical concept and is difficult to define in experiments.

2.3.6 The triple line energy

Before ending our discussion of non-equilibrium wetting, one additional model which is occasionally found in literature for evaluating hysteretic CAs must be mentioned. As a logical progression of the concept of a pinning energy barrier opposing movement of the triple line, one might consider whether or not the triple line tension causes the observed deviation from equilibrium wetting angles. With this hypothesis, the triple line tension term is added to Young's energy balance and can be fitted to experimental data. But here we already run into trouble, because the triple line tension must invert its sign if we are to describe CAH for both the advancing and receding cases. This is of course nonsense; nonetheless, several studies have investigated the utility of this concept in describing hysteresis. They typically measured triple line energies orders of magnitude larger than would be expected from the broken atomic bonds along the triple line [28,44–46]. Thus, the picture is not so simple and the measured triple line energy has been attributed to energy barriers caused by surface heterogeneities as discussed in section 2.3.5. Moreover, it is not yet clear if this triple line energy is in fact constant (i.e. a property of the triple line). To differentiate from the traditional meaning of triple line energy, we will call this the "effective" triple line energy, ϵ_t. Although the triple line energy has clear drawbacks, it can be easily incorporated into Young's equation and is an advantageous parameter for quantifying and comparing CAH in different wetting systems.

2.4 Reactive wetting

So far we have only discussed chemically inert wetting systems (i.e. liquid and substrate atoms do not form covalent/ionic bonds). Moreover, although models for non-reactive wetting systems offer a strong foundation for modelling reactive systems, there are important intricacies relevant solely to reactive wetting systems which must be considered to accurately and analytically describe the wetting behavior of reactive systems.

These differences stem of course from the defining feature of reactive wetting; a reactive product phase is continuously formed at the solid-liquid interface. Unfortunately, the interfacial reaction which is decisive in controlling the wetting behavior is impractical to evaluate in-situ, primarily because it would require the in-situ microscopic chemical and crystallographic analysis of (i) the substrate-liquid interface which is hidden by molten metal and; (ii) the triple line which is moving. Nonetheless, the interface reaction is not instantaneous, so it is desirable conceptually to consider the reactive wetting processes stepwise. According to studies investigating spreading kinetics, multiple stages of reactive spreading have been proposed [47]. As visualized in Figure 2.11, reactive spreading is typically argued to progress as follows: (1) a molten droplet is first in contact with a substrate; (2) the droplet triple line spreads rapidly without significantly reacting and until equilibrium is achieved between the substrate-liquid-vapor phases (i.e. the droplet is in equilibrium with the unreacted substrate); (3) the spreading rate decreases, subsequently controlled by the radial growth rate of the product phase which is generally accompanied by a reduction in the interface tension and a consequent shift of the triple line equilibrium [48].

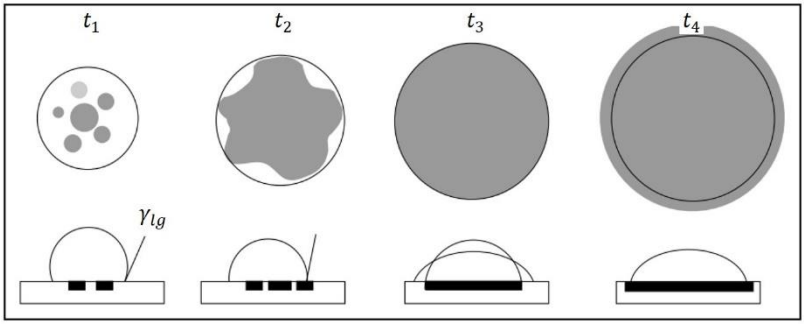

Figure 2.11: General timeline of reactive spreading. The black and grey colors represent the product phase. At t_1 the molten alloy first contacts the substrate. By t_2 the droplet triple line is spreading quickly across the largely unreacted substrate. At t_3 the initial fast spreading has ended and the reactive product phase covers the entire contact area. Finally at t_4 the reactive product phase grows ahead of the triple line. Figure adapted from Meier et al. [49]

2.5 Soldering systems

2.5.1 Metal joining techniques

Techniques for joining metals vary depending on the metal system. Two components made from similar metals and both of sufficient thickness can be joined via welding where the components are heated above their melting point locally at the joint position. For dissimilar metals or for thinner metal components which are easily deformed, soldering is generally preferable. Soldering is the process by which a filler alloy is used to bond two metal components. In this case, only the filler alloy is melted and not the joining components. Thus the filler alloy must first, have a lower melting point than the joining components and secondly, be able to wet and react with the joining components. Numerous filler alloys are available that meet the criteria for joining various metal combinations. For systems that require a high melting point filler metal—higher than 450 °C—the process is called brazing per convention. For example, aluminum-based fillers like 4043 and 5356 alloys are commonly used for brazing aluminum components.

2.5.2 Tin-based solders

Sn-based solders are predominant in low-temperature soldering applications and have the following advantages:

- They can be alloyed with various metals for specific applications.
- They form intermetallics with various high output industrial metals.
- They have relatively low melting points.
- Their cost is relatively low.

Typical alloying elements include lead, silver, copper, magnesium, antimony, zinc, and indium, although lead is now banned in Europe from usage in commercial products.

2.5.3 Cu/Sn system

The Cu/Sn system has considerable value in many industries, most particularly the PCB (printed circuit board) industry, where industrial processes for bonding of Cu with Sn-based solders are advanced. When Cu is bonded with Sn, two intermetallic

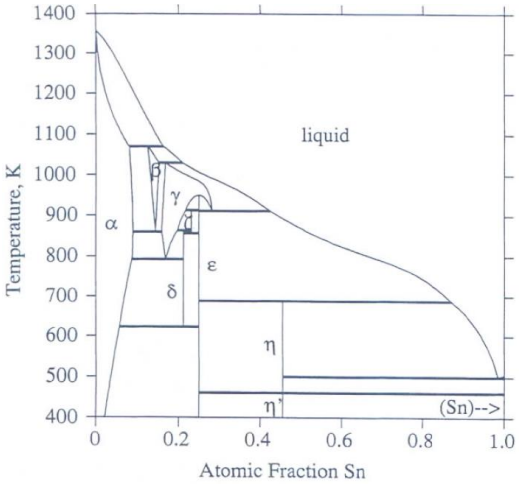

Figure 2.12: Thermodynamic calculation of the Cu-Sn phase diagram [50].

phases are typically formed at the bonding interface (see Cu/Sn phase diagram in Figure 2.12). The Sn-rich Cu_6Sn_5 (η) phase forms at the Sn interface and the Cu-rich Cu_3Sn (ε) phase forms at the Cu interface. For sufficiently low soldering temperatures and short bonding times of a few minutes—assuming there is no shortage of Sn—the Cu_6Sn_5 phase typically grows much thicker than the Cu_3Sn phase. Furthermore, the Cu_6Sn_5 phase forms an easily identifiable scallop morphology (see Figure 2.13) whereas the Cu_3Sn phase remains relatively planar. The rounded scallop geometry of the Cu_6Sn_5 phase is purported to occur because the rate of Gibbs free energy minimization in a Cu/Sn reflow system is higher if Cu can freely dissolve between Cu_6Sn_5 scallops into the solder.

In other words, the prevailing morphology is defined by the reaction path with the fastest reduction in Gibbs free energy. Tu and Gusak outlined the "Flux Driven Ripening" (FDR) model to describe such ripening which exhibits constant surface area and increasing volume as opposed to the Lifshitz-Slezov-Wagner (LSW) theory which describes constant volume, surface area minimization ripening [51]. Finally, the

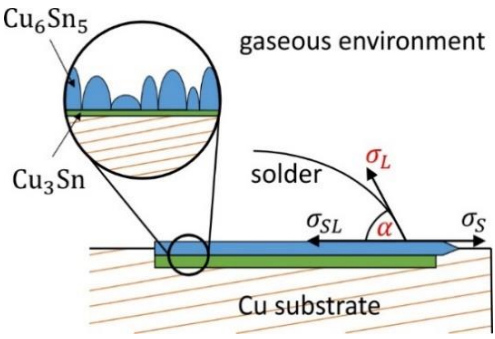

Figure 2.13: Depiction of the grain morphology of the Cu/Sn reflowed solder system [53].

rounded scallop grain shape likely results from the Cu_6Sn_5 interface tension equilibrium [52].

2.5.4 Ni/Sn system

The Ni/Sn system allows three stable intermetallics, nonetheless only the Sn-rich Ni_3Sn_4 phase forms during reflow of Sn on Ni substrates (see Ni/Sn phase diagram in Figure 2.14). The growth of the Ni_3Sn_4 phase differs slightly from the Cu_6Sn_5 of the Cu/Sn system. Initially, Ni_3Sn_4 grains form at the substrate with channels between them through which Ni can dissolve and diffuse into the Sn. But as the reaction time extends, new Ni_3Sn_4 grains form and push the existing grains perpendicularly away from the Ni substrate. This eventually results in the transformation of the channels—at least partially—into grain boundaries, which does not follow the FDR model [54]. For the same reason, the rate of growth of the intermetallic compound (IMC) thickness is slower for the Ni/Sn system than for the Cu/Sn system.

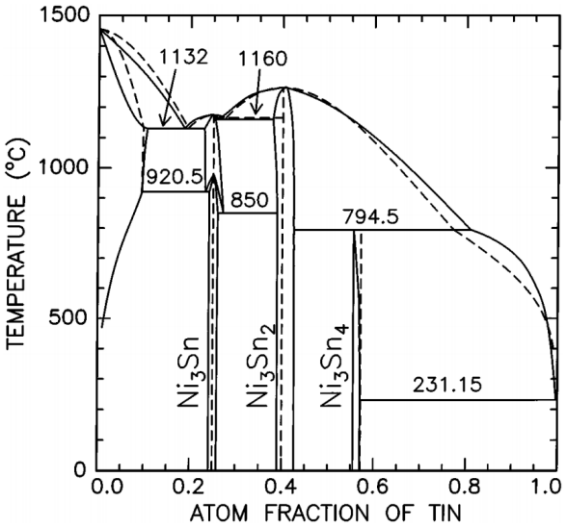

Figure 2.14: Thermodynamic calculation of the Ni-Sn phase diagram [55].

3 Experimental methods

3.1 Sample preparation

3.1.1 Silicon and silicon dioxide substrates

To prepare samples for reactive wetting experiments using electrodeposition, it was necessary to choose a suitable substrate that would provide highly reproducible surfaces. Factory polished 6" (111) and (001) silicon wafers (thickness ≈ 1 mm) were used for this purpose from which chips of suitable size were cut (typical polished top surface dimensions were 1-3 cm depending on the experimental requirement).

Silicon wafers were oxidized in some cases where a thick oxide passivation layer was desired. Silicon wafers were annealed in a box oven in standard atmosphere at ca. 1100 °C for 30 minutes. The silicon wafers could be identified as oxidized by a change of color from silver to multi-colored. The thickness of the oxide was not critical in the present study since its purpose was to act as a wetting barrier; as such a visual inspection of oxidation was sufficient.

3.1.2 Ion-beam sputtering

Ion beam sputtering is a variety of physical vapor deposition used for producing thin films whereby—as the name suggests—the material to be deposited is bombarded with accelerated ions which sputter evaporate the target material onto the sample substrate. The sputter chamber used in the present work (schematic provided in Figure 3.1) was prebuilt and custom-designed and comprises a DC operation ion gun from Roth and Rau, a neutralizer for neutralizing the impinging ions, a revolving target holder with four slots, a sample lock to load samples, and a sample holder and adjacent quartz crystal balance for thickness recording. The DC operation ion gun compared with an RF gun has the advantage of simplifying maintenance, but has the disadvantage of being incompatible with insulating target

materials which are prone to charging artifacts. The sputter chamber was typically operated in the manner subsequently described. The desired targets (typically pure metals) are inserted into the chamber and the chamber is evacuated to at least $p < 10^{-6}$. Silicon chips are prepared by washing with acetone followed by isopropanol and drying with a pressurized air gun. The Si-chips are attached to a sample plate and transferred into the sample holder of the chamber via the sample lock.

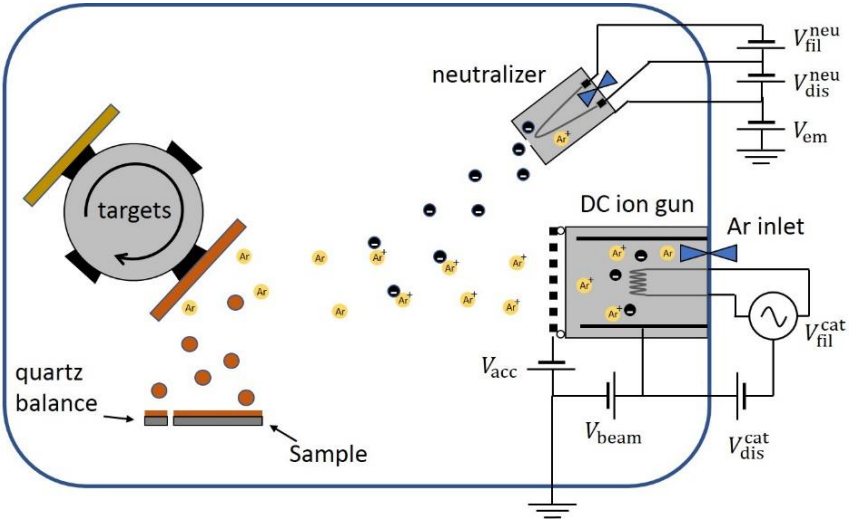

Figure 3.1: Schematic of the DC ion gun sputter chamber used for thin film deposition.

A target is rotated into position for cleaning and the sample is initially protected with a shutter cap. Argon gas flow is switched on to the DC gun and neutralizer to assist plasma generation. The cathode discharge voltage $V_{\mathrm{dis}}^{\mathrm{cat}}$ is turned on and the cathode filament current is increased until sufficient discharge current is measured. The beam is activated by switching on the beam voltage V_{beam} and accelerator voltage V_{acc}. The ion beam is neutralized by setting the neutralizer emission current I_{em} to ca. 1.5 – 2.5 times the beam current I_{beam} and the neutralizer filament heating voltage $V_{\mathrm{fil}}^{\mathrm{neu}}$ is automatically regulated.

Table 3.1: Ion-beam sputtering parameters for silicon chip cleaning/activation and thin film deposition.

	Cleaning / surface activation	Sputter deposition
Beam voltage [V]	600	1000
Acceleration voltage [V]	100	100
Beam current [mA]	10	20
Neutralizer Current [mA]	15 – 25	30 - 50
Time [s]	30	-
Thin-film thickness [nm]	-	~10(Cr) / ~20 (Cu/Ni)

The targets are cleaned of surface contamination by sputtering for ca. 5 minutes each. The Si-chips are also briefly exposed to the ion beam to improve adhesion, although only for 30 seconds and using a reduced voltage and current (see sputtering/cleaning parameters in Table 3.1). Finally, the required metals are sputter deposited onto the samples with the deposition thickness being monitored via the quartz microbalance display unit. The ion beam and neutralizer are switched off similarly to the process of switching on only in reverse. The samples are removed via the sample lock.

3.1.3 Direct laser writing photolithography

Photolithography is a technique used to microfabricate surfaces, typically thin films, and is widely applied in the microelectronics industry. A photosensitive polymeric solution called a photoresist is coated on a surface and exposed to light of a critical wavelength which acts to either degrade (positive photoresist) or cross-link (negative photoresist) the polymer coating, leaving the surface partially protected and partially exposed. The exposed surface is typically etched or coated with a thin film after which the photoresist is removed. This process may be repeated numerous times to produce complex 3D layered systems. One must also differentiate between photolithography with or without photomasks. Photomasks function as a stencil for light. They are placed on the process surface and are exposed to a homogeneous large area parallel light source; light is partially

transmitted and partially photoabsorbed by the template. Photomasks are generally processed using electron beam lithography which offers a significantly higher spatial resolution than photolithography. Conversely, maskless photolithography or direct laser writing photolithography is a probing technique where a laser writes directly into the photoresist, offering immediate patterning flexibility.

In the present work, sputtered silicon substrates were patterned using a custom-built near-UV lithographic laser writer (see Figure 3.2 for a description of components). Pattern geometries will be discussed later in section 5.2. The silicon substrates were cut sufficiently large so that the patterned areas were unaffected by the uneven photoresist at the substrate edges. The lithographic process as applied in this work will now be outlined: (1) a sputter-coated silicon substrate was cleaned by first lightly wiping with an acetone wetted lint-free tissue, followed by rinsing in acetone and then isopropanol before finally drying with a pressurized air-gun to avoid residue of the substrate. (2) the substrate was fastened on the spin-coater suction hole and a few drops of positive photo resist (AR-P 3210 from AllResist, Germany) were poured directly onto the substrate to avoid bubbles that may form when dispensing with a pipette. (3) The substrate was spin-coated using the manufacturer specified time and rotation rate for a film thickness of ~10µm (1 min @ 4000rpm for AR-P 3210). (4) The photoresist was pre-baked to improve adhesion (4 min @ 95 °C for AR-P 3210). After the photoresist film quality was deemed homogeneous by visual inspection, the sample was transferred onto the lithography sample stage. (5) The height of the objective lens was adjusted to position its focal point in the photoresist film. This was achieved during the laser beam, whereby the focal length was aligned by observing the spot size in the CCD camera imaging software. To avoid disruption of the fidelity of the final pattern geometries, the focal point was aligned near the edge of the substrate far from the center where the final patterning was done. (6) The pre-designed bitmap pattern image was loaded into the laser writer software, and the sample was repositioned on the stage so that the center of the substrate was patterned. (7) After processing, the photoresist was developed in the manufacturer-recommended development solution, AR 300-26, typically for 3-6 minutes while regularly stirring the solution. Longer or shorter development times generally meant under or overexposure resulting in irregular structure patterning. Developed samples were finally rinsed in deionized water and dried with a pressurized air gun.

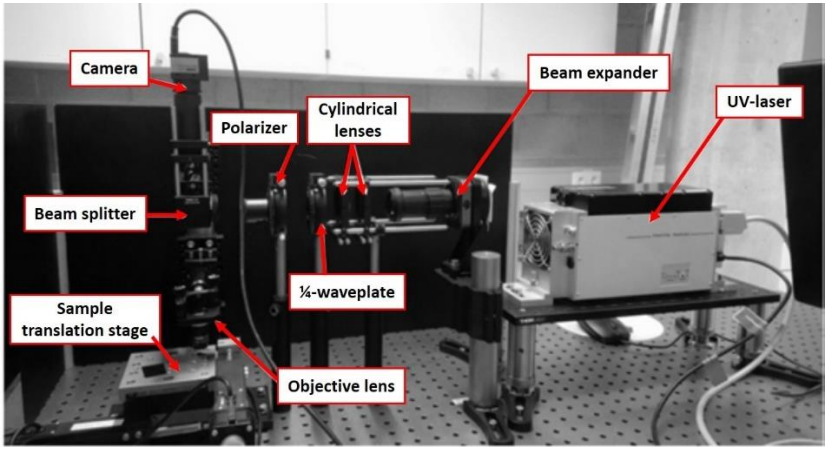

Figure 3.2: Photolithographic laser writer. The laser writer operates as follows: (1) a 355nm Q-switched laser pulses UV-radiation, (2) the spatial energy profile of the pulse is circularized by two cylindrical lenses, (3) the pulse power is attenuated using a quarter waveplate and polarizer, and (4) the beam is reflected to the objective lens by a beam-splitter and focused onto the sample. The reflection from the sample surface can be observed through the beam splitter via a CCD camera. Both the sample stage x-y axes and the objective z-axis positions translate via software controlled stepper motors. The trigger voltage for pulsing the laser is software controlled using an intermediate TTL (Transistor-Transistor-Logic) circuit board for regulating the voltage. The stepper motors have a resolution of 50 nm, yet the minimum reproducible focused laser-pulse spot size is ca. 10 µm, which defines the spatial resolution for complex patterning.

3.1.4 Electroplating

Many of the samples prepared within the scope of this work required partially or completely metalized substrates with either copper or nickel. Partial metallization of substrates was assisted by lithographic patterning. A simple two-electrode electrolytic cell was used for electrodeposition, with a prepared substrate as the cathode and a copper or nickel plate as the anode (see Figure 3.3 for the setup and Table 3.2 for electrolytes and typical deposition parameters). The electrodes were fastened using alligator clamps and if necessary the contact resistance was improved by etch-cleaning the clamps in formic acid or cleaning the substrate

contact point with acetone/ethanol. A magnetic stirrer in the electrolyte served to reduce the influence of hydrogen bubbles degrading the quality of the deposited layer. Undesired H_2 bubbles form in the acidic electrolyte as a side reaction at the cathode surface by hydrogen reduction, $2H^+ + 2e^- \rightarrow H_2$, particularly during nickel deposition.

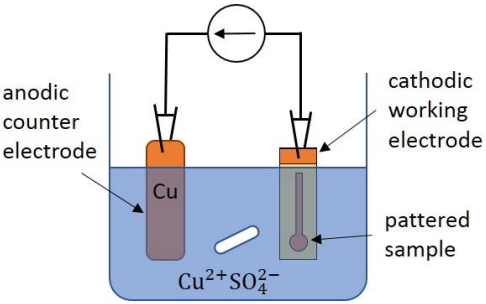

Figure 3.3: Setup of the electrolytic cell used to metalize patterned substrates with copper.

For optimal reactive wetting experiments on patterned microstructures, it was necessary to maximize deposition thickness without photoresist overgrowth occurring. Applying Faraday's law for an ideal system (equation (24)) to calculate the deposition mass m, it is possible to approximate the time t required to deposit the desired metallization thickness d assuming the anode material density ρ, the cathode surface area A, and the deposition current I are known.

$$m = \frac{QM}{Fv}, \qquad Q = \int_0^t I(\tau)dt\,, \qquad d = \frac{m(t)}{A\rho} \tag{24}$$

Here F is Faraday's constant, v is the ion valence, and M is the electrolyte molarity. To improve the reproducibility of the expected deposition time, it is advisable to protect the Si-chip edges from undesired heterogeneous metallization, i.e. growth outside the patterned area. In cases where sample edges cannot easily be protected, heterogeneous electrodeposition may occur. Consequently, the current density cannot be accurately known and a sequence of trial and error experiments must be conducted to attain the optimal deposition time. Furthermore, the deposition can be intermittently paused and the sample retracted to visually inspect whether the deposition is complete or needs more time. The typical parameters used for electrodeposition are provided in Table 3.2.

Table 3.2: Typical parameters used for the metallization of substrates using a two-electrode electrolytic cell.

	Copper	Nickel
Electrolyte	Copper sulfate pentahydrate ($CuSO_4 \cdot 5H_2O$), 2.5% Sulfuric acid (H_2SO_4), pH: 0	Nickel sulfate hexahydrate ($NiSO_4 \cdot 6H_2O$), 25% acetic acid (CH_3COOH), pH: 2
Deposition mode	Chronopotentiometry	Chronopotentiometry
Deposition current	5 mA	5 mA
Deposition time	~45 min	~30 min

3.2 Reflow measurements

3.2.1 Vacuum furnace

Solder reflow experiments were conducted in a vacuum furnace (see Figure 3.4 schematic). The furnace housed a resistance heated stage with an external transformer controlling the voltage/heating rate and an inbuilt thermostat assisting temperature regulation. A rotary pump provided the chamber with vacuum and a gas valve separated the pump from the chamber. A gas inlet provided the option for either pure nitrogen atmosphere or a mixture of nitrogen/formic acid gas and an outlet relief valve regulated the chamber to standard pressure. A binocular microscope with a CCD camera was fastened either at the top or side chamber viewing windows depending on the requirement. A backlight was additionally positioned directly behind the heating stage providing a high contrast silhouette of the sample during Sessile Drop measurements imaged with the microscope and camera positioned in the horizontal plane.

3.2.2 Reflow procedure

The general procedure for operating the vacuum furnace was as follows: a sample is placed onto the heating stage and the chamber is closed (all valves of Figure 3.4 are closed unless otherwise stated); the chamber is pumped to a pressure of

approximately $2 \cdot 10^{-2}$ mbar (V1 open); the chamber is purged with nitrogen gas until atmospheric pressure is reached (V2, V3, V6, V_r open); the nitrogen gas is then redirected through a formic-acid-filled glass bubbler creating a N_2/formic acid gas mixture which continuously purges the chamber throughout the experiment minimizing oxygen contamination (V2, V4 - V6, V_r remain open); the solder alloy is then typically heat-treated at 150 °C for 30 minutes accelerating the reducing effect of the N_2/acetic acid atmosphere, removing surface oxides from the solder; finally, the solder is melted at the desired temperature and any required in-situ images or videos are recorded. Before retrieving the sample, the chamber was purged with nitrogen to remove any toxic fumes.

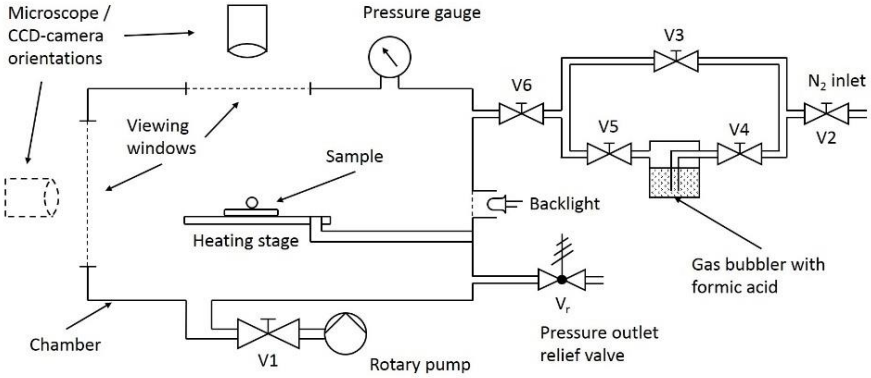

Figure 3.4: Vacuum furnace used to conduct reactive wetting and surface tension measurements.

4 Work of adhesion and reactive wetting of SnPb and SnBi solder on Cu and Ni substrates

4.1 Introduction

In recent years, continued research into solder joint technologies has been motivated by the phasing out of toxic lead-containing solders and the search for lead-free alternatives. Furthermore, due to the ever-present desire to reduce solder joint sizes, a fundamental understanding of interface thermodynamics is required. Consequently, properties like the adhesive strength of a joint—which is one critical indicator of joint quality—may be predicted. For a liquid-solid wetting system, the adhesion strength at the liquid-solid interface can be principally described by the work of adhesion W_a and the balance of the surface and interface tensions (see eq. (14), Dupre equation). For a solidified solder joint, W_a represents the minimum energy required to cleave the interface, although in practice the mechanical strength of the joint may additionally be influenced by bulk material properties such as Kirkendall void density or fracture toughness. Often the adhesion strength of a liquid-solid joint is evaluated by its contact angle, although this provides only a rough approximation. Alternatively, by measuring both the liquid surface tension and contact angle, the work of adhesion can be quantified according to the Young-Dupre equation (15). Nonetheless, it is rare to find work of adhesion data of solder alloys comprehensively quantified, particularly in dependence of temperature and solder composition [56–58].

Describing the wetting behavior of solder alloys comes with additional complications due to the formation of one or more reactive product phases. Take for example the $Sn^{(l)}/Cu^{(s)}$ system (where Sn can represent various Sn-based solder alloys), which upon joining form two characteristic intermetallic phases as depicted in Figure 2.13. The Sn-rich Cu_6Sn_5 phase takes on a rough heterogeneous scallop-like morphology which both increases the solid-liquid interface area as described by Wenzel (c.f. section 2.2.5) and typically causes hysteretic results (c.f.

section 2.3.1), and although such phenomena are well documented [59–62], no universal predictive model exists to describe contact angle hysteresis. This is largely due to the random nature of surface heterogeneities, but in the case of reactive wetting also because of their sensitivity to the immediate environment (temperature and atmosphere) and oxidation. Furthermore, reactive systems may exhibit time-variant properties at the spreading triple line including the concentration of the reacting alloy component, the spreading rate which becomes slower towards equilibrium, and surface roughening due to the formation of rough IMCs. For these reasons, debates regarding the driving force of reactive wetting and the predictability of contact angles continue.

4.1.1 The reactive spreading driving force

Until the late 1980s, few articles were concerned with describing the driving force for reactive wetting. One of the first noteworthy models was conceived in 1987 by Yost and Romig [63], who postulated that the product phase free energy of formation ΔG must be included in the interfacial energy balance to account for the driving force of product formation. They derived the following revised energy balance

$$\frac{1}{2\pi r}\frac{dE}{dr} = \Gamma(\theta) + l_p \Delta G \tag{25}$$

Where the component $\Gamma(\theta)$ represents the driving force of the interface tensions and l_p is the product phase thickness assumed to be homogeneous.

$$\Gamma(\theta) = \gamma_l(\cos\theta - \cos\theta_0) \tag{26}$$

Yost argued that the triple line of a reactive droplet on a substrate is driven to spread predominantly by the free energy of formation of the product phase which reduces the Gibbs energy significantly more (ca. 1 order of magnitude or more) than the balancing of the interface energies. This model has the logical consequence that, for reactive wetting systems with equivalent product phases and differing only in solder alloy concentration, the alloy concentrations with the larger free energy of product formation would result in smaller equilibrium wetting angles and a thicker product phase. A study by Tu et al. [64] investigated this condition, but their results were inconclusive and seemed to dispute the model

of Yost. They found that, for SnPb solder on Cu substrates, the wetting angle was lower at intermediate compositions although the IMC thickness became larger with higher Sn concentration. They claim that the short time required for the molten droplet to reach equilibrium (~1s) is too short for the Gibbs energy of IMC formation to be an impactful wetting driving force. Instead, they recommend the alternative use of the IMC growth rate as a term, additional to the imbalance of the interface tensions, describing the wetting driving force. Although they did not elaborate on this idea.

Another model was proposed by Eustathopoulos [48,65] who did not include a term for the free energy of product phase formation, but simply corrected Young's energy balance replacing the solid-liquid and solid-vapor interface tensions with σ_{pv} and σ_{pl}, the product-vapour surface tension and product-liquid interface tension respectively, where the uppermost product layer is decisive.

$$F_d(t) = \sigma_{pv} - \sigma_{pl} - \sigma_{lv}\cos\theta(t), \qquad \cos\theta_0 = \frac{\sigma_{pv} - \sigma_{pl}}{\sigma_{lv}} \qquad (27)$$

Here $F_d(t)$ is the driving force for spreading at time t which will approach 0 as the wetting angle $\theta(t)$ approaches equilibrium. The model of Eustathopoulos requires that the product phase extends ahead of the spreading triple line (see Figure 2.13). This is generally energetically favorable as product-liquid interfaces are predominantly less energetic than initial solid-liquid interfaces and result in a reduction of the contact angle. Furthermore while investigating reactive wetting of liquid aluminum on a vitreous carbon substrate Eustathopoulos observed an approximately linear spreading (constant radial spreading rate) period, which he attributed to the lateral product phase growth rate which limited the radial spreading rate, and which served at least as confirmation that the product phase rather than the initial solid phase is decisive in the reactive wetting interfacial energy balance equation (27). A study of Saiz [66] investigating Sn-3Ag-xBi solders on Fe-42Ni similarly concluded the product phase, not the initial substrate phase, to be decisive in controlling reactive wetting equilibria, although he claims that during reactive spreading the product phase first nucleates behind the spreading triple line and only as equilibrium is approached does the product phase begin to nucleate ahead of the triple line.

The following investigation aims to clearly outline the relationship between reactive alloy composition, reactive product phase, wetting equilibria, and adhesion strength. To this end, the surface tension and equilibrium wetting angles

of $Sn_{1-x}Pb_x$ and $Sn_{1-x}Bi_x$ are measured on Cu and Ni substrates at two temperatures over the entire composition ranges. Moreover, by keeping the environmental conditions constant across all measurements, it is possible to calculate $W_a(x)$ via equation (15) for all material systems over the entire composition range, for which there is limited data. The two substrate metals are commonly implemented in electronic packaging technologies just as Sn is most commonly used industrially as the predominant reactive component in soldering alloys. The choice to use bi-metallic solder alloys with Pb and Bi as alloying components offers the ability to easily vary the chemical potential over the entire alloy composition range. Furthermore, with the additional variation of temperature, it becomes possible to evaluate, compare, and draw conclusions on the dependence of the adhesion strength on the thermodynamics and phase stabilities at the reaction interfaces for several systems.

Additionally, thermodynamically modeled work of adhesion data is calculated to support our experimental findings and thermodynamic information for the various material systems is provided to support our conclusions. Finally, it should be noted that previous seminal studies in this field were largely focused on slower spreading high-temperature flux-free brazing material systems [48,67,68] which are simpler to evaluate kinetically and may behave differently to high spread rate low-temperature solder material systems such as those investigated presently.

4.2 Experimental

Surface tension and contact angle measurements were originally conducted by Wedi using the Sessile drop method in the vacuum furnace schematized in Figure 3.4. The raw data although was evaluated within a meaningful thermodynamic frame in this work [53]. For a detailed description of the vacuum-furnace operation see section 3.2.2.

4.2.1 Surface tension measurements

The surface tensions of each alloy composition were measured separately. The method applied for determining the surface tension requires that the droplet form exhibits two principal radii, but it is also desirable that the droplet contact angle is maximized. To assure that the droplet was not spherical it was made sufficiently large to be flattened by gravitational force. Thus for each composition, a piece of

$Sn_{1-x}Pb_x$ and $Sn_{1-x}Bi_x$ was prepared with sufficient mass to form a droplet larger than the capillary radius. The capillary length or capillary radius R_c relates surface tension to gravity and is useful in defining menisci which are deformed by gravity ($R > R_c$) and those where gravitational deformation is negligible ($R < R_c$).

$$R_c = \sqrt{\sigma_{lv}/\Delta\rho g} \tag{28}$$

Here $\Delta\rho$ is the density difference between the sample liquid and surrounding gas environment and g is the acceleration of gravity. The piece of solder was then placed onto a quartz glass microscope slide on the heating plate of the vacuum furnace. The quartz glass served both as a chemically passive substrate and as a strongly dewetting surface (at least in combination with the presented alloys) maximizing the contact angle of the molten solder droplet. The solder alloys were reflowed at various temperatures starting at 500 °C and decreasing in 50°C steps down to their respective melting points and in-situ images of the molten solder droplet silhouettes were recorded for every alloy at each temperature step. The surface tension was determined from these images using the Laplace pressure which relates surface tension to droplet radius. The Laplace pressure at the apex of a droplet can be simplified as $\Delta P_{apex} = \frac{2\sigma_{lv}}{R_{apex}}$. Furthermore, for a liquid body in hydrodynamic equilibrium, the pressure difference within the body is directly related to the depth and the liquid density. Therefore the difference between the pressure at the apex of the droplet and some other reference depth is given by the substitution of equations (9) and (12) and assuming axis symmetry as:

$$\Delta P_{\text{apex}} - \Delta P_{\text{ref}} = \sigma_{lv}\left(\frac{2}{R_{\text{apex}}} - \frac{1}{R_1} - \frac{1}{R_2}\right) = z\Delta\rho g \tag{29}$$

Where R_1 and R_2 are the two principal radii of curvature at the reference height z. The droplet contours were fitted using the Low-Bond Axisymmetric Drop Shape Analysis plugin of ImageJ developed by Stalder et al. [69]. The molten solder density was determined simply from the measured initial mass and the volume determined from the droplet contour (see Figure 4.1 (a)). Finally, equation 29 was solved for the surface tension by determining the droplet radii from the droplet contour.

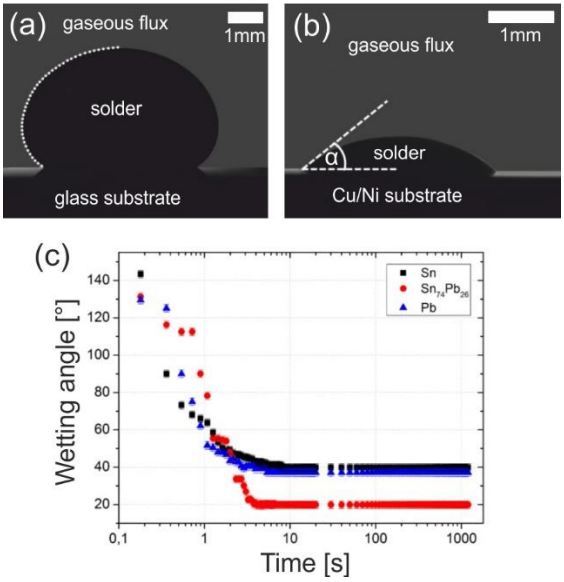

Figure 4.1: In-situ solder measurements in the vacuum furnace: (a) surface tension measurement, solder is melted on a glass plate; (b) wetting angle measurement, molten solder wets a metallic substrate; (c) the temporal development of the reactive wetting angle of three different solder compositions [53].

4.2.2 Wetting angle measurements

The wetting angles were determined similarly to the surface tensions in the vacuum furnace, only that the solder alloy pieces were first melted into balls on glass slides before being melted on the polished Cu/Ni metal plates. In this case, the solder balls were made sufficiently small to avoid gravitational effects (see Figure 4.2 (b)). Each $Sn_{1-x}Pb_x$ and Sn_{1-x} Bi_x solder composition was reflowed for 20 minutes on both Cu and Ni substrates and at both (350±2) °C and (500±2) °C. In-situ images of the reactive wetting angles were recorded (see Figure 4.1 (a)) and the angles were measured by fitting the droplet contour using ImageJ.

4.2.3 Thermodynamic modelling of surface and interface energies

To test the reliability of our experimental results, it was desirable to test their consistency with theoretical thermodynamic expectations. For binary liquid

systems, it is practical and commonplace to model solution thermodynamics by applying the regular solution model or extensions thereof. From statistical thermodynamics, we know that the molar Gibbs energy G of a binary solution is given by

$$G = c_A G_A + c_B G_B + RT(c_A \ln c_A + c_B \ln c_B) + \Delta G_{mix}^{XS} \tag{30}$$

Where c_i is the molar concentration and G_i is the molar Gibbs energy of pure component i, R and T are the universal gas constant and absolute temperature, and ΔG_{mix}^{XS} is the excess Gibbs enthalpy of mixing. The definition of the chemical potential μ_A of component A follows as

$$\mu_A \equiv \left(\frac{\delta G}{\delta n_A}\right)_{T,P,n_B} = \mu_{A,0} + RT \ln c_A + \Delta^{\mathrm{XS}} G_A \tag{31}$$

Where n_A is the moles of atom A, $\mu_{A,0}$ is the molar Gibbs energy of pure component A, and $\Delta^{\mathrm{ex}} G_A$ is the partial molar excess Gibbs energy of component A. Now considering two components of a binary mixture each with different interface energies, it is well established that the component with lower excess energy will segregate to the interface. In 1931, Butler conceptualized a method accounting for interface segregation [70] which differentiates between the chemical potential of component i in the bulk $\mu_i^{(b)}$ and the chemical potential in the surface or interface regions $\mu_i^{(i)}$ [71], defined as

$$\begin{aligned} \mu_A^{(i)} \equiv \left(\frac{\delta G^{(i)}}{\delta n_A^{(i)}}\right)_{T,P,n_B} - a_A\sigma &= \mu_A^{*(i)} - a_A\sigma \\ &= \mu_{A,0}^{*(i)} + RT \ln c_A + \Delta^{XS} G_A - a_A\sigma \end{aligned} \tag{32}$$

Where $\mu_A^{*(i)}$ we call the reduced partial molar Gibbs energy of A at the interface, $\mu_{A,0}^{*(i)}$ is the reduced partial Gibbs energy of pure A at the interface, and a_A is the partial molar interface area of component A. Note that $\mu_A^{*(i)}$ contains the energy of broken bonds at the interface whereas $\mu_A^{(i)}$ does not. Rearranging eq. (32) and considering $\mu_A^{(i)} = \mu_A^{(b)}$ in equilibrium (where (b) represents the bulk), it follows that

$$\sigma = \frac{\mu_A^{*(i)} - \mu_A^{(b)}}{a_A} = \frac{\mu_B^{*(i)} - \mu_B^{(b)}}{a_B} \tag{33}$$

Which related the interface tension of a mixture to the chemical potentials of either/both components. This is the basis on which the surface and interface tensions can be modeled. The partial molar surface areas a_k are calculated from the atomic density of the melts as $a_k = f \cdot (m_k/\rho_k)^{2/3} N_A^{1/3}$, where f is the packing factor ($f = 1.091$ representing the densely packed FCC {1 1 1} plane is used as is commonplace for liquids) [72,73], m_k and ρ_k are the molar mass and density of pure liquid k and N_A is Avagadro's number. Substituting the chemical potentials $\mu_k^{*(i)}$ and $\mu_k^{(b)}$ from eqs. (31) and (32) into (33) yields

$$\sigma_A^0 + \frac{RT}{a_A}\ln\left(\frac{c_A^{(i)}}{c_A}\right) + \frac{1}{a_A}\left(\Delta^{XS}G_A^{(i)} - \Delta^{XS}G_A^{(b)}\right) = \sigma_B^0 + \frac{RT}{a_B}\ln\left(\frac{c_B^{(i)}}{c_B}\right) + \frac{1}{a_B}\left(\Delta^{XS}G_B^{(i)} - \Delta^{XS}G_B^{(b)}\right) \quad (34)$$

Where σ_k^0 represents the interface energies of the pure components which necessary result from the case where $c_k = c_k^{(i)} = 1$, and $\Delta^{XS}G_k^{(i)}$ and $\Delta^{XS}G_k^{(b)}$ are the excess partial Gibbs energies of component k at the interface and in the bulk respectively. As usual $c_B = 1 - c_A$. As already outlined by Picha et al. [76], the excess partial Gibbs energies in eq. (34) can be derived from Redlich-Kister polynomials [77] and bulk interaction parameters. Since the excess energy of broken bonds at the interface is contained in the interface energies of the pure metals, we expect the interaction parameter at the interface to be the same as in the bulk, reduced by a factor representing the reduction of nearest neighbor bonds at the interface. Thus we have set the interaction parameters at the interface equal to the bulk interaction parameters multiplied by the factor $\lambda < 1$. By inserting the Redlich-Kister polynomials for a sub-regular solution into eq. (34) and rearranging yields

$$\begin{aligned}\sigma_B^0 - \sigma_A^0 = \frac{RT}{a_A}\ln\left(\frac{1-c_B^{(i)}}{1-c_B}\right) \\ -\frac{RT}{a_B}\ln\left(\frac{c_B^{(i)}}{c_B}\right) + \frac{L_0}{a_A}\left(\lambda {c_B^{(i)}}^2 - c_B^2\right) \\ -\frac{L_0}{a_B}\left(\lambda\left(1-c_B^{(i)}\right)^2 - (1-c_B)^2\right) \\ +\frac{L_1}{a_A}\left(\lambda {c_B^{(i)}}^2\left(3-4c_B^{(i)}\right) - c_B^2(3-4c_B)\right) \\ -\frac{L_1}{a_B}\left(\lambda\left(1-c_B^{(i)}\right)^2\left(1-4c_B^{(i)}\right)\right. \\ \left. -(1-c_B)^2(1-4c_B)\right)\end{aligned} \tag{35}$$

Where L_0 and L_1 are the zeroth and first-order interaction parameters, respectively. Equation (35) can be solved for the surface or interface concentration $c_B^{(i)}$ which differs from the bulk concentration c_B due to segregation. Furthermore, for the solid-liquid interface, it is assumed that the contacted solid is a stoichiometric phase, independent of solder composition. All other variables are known from the experimental surface tension and contact angle measurements, except for the bulk interaction parameters which were taken from literature. With all other variables known, the surface and interface tensions were calculated as

$$\begin{aligned}\sigma(c_B) = \sigma_B^0 + -\frac{RT}{a_B}\ln\left(\frac{c_B^{(i)}}{c_B}\right) \\ +\frac{L_0}{a_B}\left(\lambda\left(1-c_B^{(i)}\right)^2 - (1-c_B)^2\right) \\ +\frac{L_1}{a_B}\left(\lambda\left(1-c_B^{(i)}\right)^2\left(1-4c_B^{(i)}\right)\right. \\ \left. -(1-c_B)^2(1-4c_B)\right)\end{aligned} \tag{36}$$

Which is obtained similarly to eq. (35) by substituting the chemical potential terms of eq. (33). Finally, it should be noted, strictly speaking, and unless otherwise stated, that wherever the interface tension is discussed in the present chapter, the term $\Delta\sigma_s = \sigma_{sv} - \sigma_{sl}$ is meant. This is because, the two solid interface tension terms are not easily measured or separated.

Table 4.1: Thermodynamic model fixed and free fitting parameters.

Solder / Temperature [°C]		SnPb		SnBi	
		350	500	350	500
Fixed parameters					
$L_0^{bulk\ liquid}$ [J/mol] *		5940	5877	1092	1237
$L_1^{bulk\ liquid}$ [J/mol] *		-402.7	-689.8	-176.4	-211.7
Partial molar surface area [m²/mmol]		$a_{Sn} = 61.70,\ a_{Pb} = 66.44,\ a_{Bi} = 70.13$			
Free fitting parameters					
$\sigma_l^{Sn,0}$ [mJ/m²]		515.7	487.9	515.8	487.9
$\sigma_l^{x,0}$ [mJ/m²] (x=Pb, Bi)		398.7	379.0	342.5	325.8
Copper substrate	$\Delta\sigma_{Cu_3Sn}^{Sn,0}$ [mJ/m²]	403.4	465.8	406.4	425.8
	$\Delta\sigma_{Cu_3Sn}^{x,0}$ [mJ/m²]	321.7	328.9	149.3	187.1
	$\Delta\sigma_{Cu_6Sn_5}^{Sn,0}$ [mJ/m²]	411.4	-	-	-
	$\Delta\sigma_{Cu_6Sn_5}^{x,0}$ [mJ/m²]	359.7	-	-	-
	Atomic fraction Sn consumed $\kappa = 1 - n_i^{Sn}/n_f^{Sn}$ (*)	0.25	0.5	0.45	0.5
Nickel substrate	$\Delta\sigma_{Ni_3Sn_4}^{Sn,0}$ [mJ/m²]	431.1	444.3	406.1	417.3
	$\Delta\sigma_{Ni_3Sn_4}^{x,0}$ [mJ/m²]	343.5	374.4	96.2	153.4
	Atomic fraction Sn consumed $\kappa = 1 - n_i^{Sn}/n_f^{Sn}$ (*)	0.05	0.1	0.45	0.5

*bulk interaction parameters are literature values. [74] for SnPb and [75] for SnBi.

Furthermore, since σ_{sv} is constant, any observed variation in $\Delta\sigma_s$ as a function of concentration fully describes the change in σ_{sl} as a function of concentration. Thus, for interface tension modelling, the anchoring concentrations required as initial parameters in eqs. (35) and (36) were determined via Young's equation as $\Delta\sigma_s = \sigma_{lv}\cos\theta$ from the raw data of surface tension and contact angle.

4.3 Results

4.3.1 Surface Tension

Experimental data of liquid alloy surface tensions already exist for various solder alloys, including the present systems of SnPb and SnBi [78,79]. Nonetheless, differences in measurement environment between studies of otherwise equivalent systems may cause significant deviations between the measurement outcomes. Thus, it was necessary to remeasure both surface tensions and wetting angles of all solder alloy systems under equivalent environmental conditions for consistency. Figure 4.2 contains all surface tension results for SnPb and SnBi solder alloys as a function of composition and temperature. One can observe a general decrease in surface tension with increasing temperature across all alloy compositions. This is an expected outcome; as the temperature of the melt increases, it approaches the temperature of vaporization at which point the surface ceases to exist and $\sigma \rightarrow 0\ \mathrm{Nm}^{-1}$. Furthermore, the surface tension of the alloys exhibits a linear dependence on temperature for all compositions to a good approximation.

Figure 4.2 (b,d) presents the dependence of surface tension on composition for the highest (500 °C) and lowest (350 °C) temperatures measured at which all compositions were in the liquid state. For all cases (both temperatures and solder alloys) the slope $\frac{\delta\sigma}{\delta c_x}$ (where x = Pb or Bi) is varying and exhibits a steep decrease at high Sn concentrations and a flattening at higher Pb and Bi concentrations. Now comparing the modeled curves: firstly the trend of the ideal solution model curve is similar to the trend of the measured data, with a consistent bending of the surface tension curve towards the values for pure Pb and Bi, although this trend is underpredicted by the ideal solution model. By contrast, the sub-regular solution model shows greater similarity to the measured results. For the sub-regular solution model, the parameter λ defining the portion of nearest neighbor atomic bonds remaining at the surface was chosen as $\lambda = 0.7$ (i.e. assuming that for a surface atom, approximately 30% of its nearest neighbor bonds are broken). This seems to be a reasonable approximation given the good agreement with experiment. Any remaining quantitative discrepancies may be attributable to the inherent limitations of the sub-regular solution model, which for a binary system assumes equivalent atom sizes and ignores nearest neighbors beyond the first-order. The strong bending of the surface tension curve as a function of

composition, as observed by measurement and model, confirms the tendency for the element of a binary system with lower surface energy to segregate to the surface, minimizing the alloy surface tension surface segregation. This showcases the utility of Butler's concept in predicting segregation with a minimal set of free parameters.

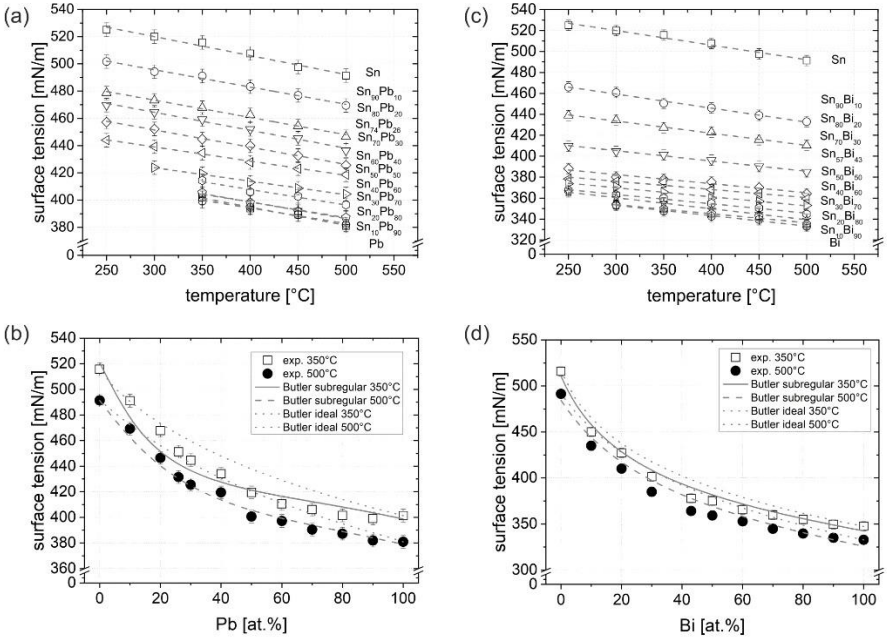

Figure 4.2: Surface tension data as a function of composition and temperature for (a,b) $Sn_{x-1}Pb_x$ and (c,d) $Sn_{x-1}Bi_x$. (b,d) additionally contain modeled curves representing the ideal solution model (dotted lines) and sub-regular solution model (solid and dashed lines) at 350 °C and 500 °C [53].

Finally, it is worth comparing the measured surface tension data with literature data for the same solder alloys, which may although be less complete or measured under different environmental conditions. An investigation of SnPb at 400 °C in a gas atmosphere of Ar/H_2 was conducted by Howie and Hondros [80] for various compositions. Although the trend of their results is similar, the values are shifted approximately 30-40 mJ/m^2 higher, presumably because of the weaker reducing strength of Ar/H_2 compared with N_2/formic acid. Mills [81] recently extended the work of Keene [82] recommending mean temperature dependencies for pure

element surface tensions, based on literature data from a variety of sources. Although their suggested temperature dependencies for Pb, Bi, and Sn are similar to ours, the absolute values are also shifted higher by ca. 20-40 mJ/m^2. A meaningful quantitative comparison is prevented by the variety of gaseous environments considered in their mean analysis. Gasior and Moser [83,84] applied the bubble pressure method to measure the surface tension of SnPb and SnBi in an atmosphere of 1% H_2 in Ar. Again we find their results to be biased approximately 20-30 mJ/m^2 higher than ours, presumably because of the weaker reducing properties of their measurement environment. This conclusion is well supported by the aforementioned study of Howie and Hondros [80], who additionally investigated the influence of different flux environments and observed that the application of organic liquid flux depressed the surface tension of molten solder relative to the same solder in a simple gaseous flux environment of Ar/H_2.

4.3.2 Wetting angle

Here, the measured wetting angle results and corresponding modeled curves will be presented. Wetting angles were measured for four combinations of substrate and solder and at two temperatures. The solders are stable in the liquid state over the entire composition range at both temperatures. Furthermore, for the Sn/Ni system, the Ni3Sn4 phase is stable at both temperatures. Conversely for the Sn/Cu system, the dominant Cu6Sn5 phase becomes unstable at the higher temperature (500 °C).

For a direct comparison, the wetting angle, interface tension, and work of adhesion results are presented side by side. Figure 4.3 and Figure 4.4 present these results for all combinations of solder alloy and temperature on Cu and Ni substrates respectively. Please be reminded that, although we discuss the interface tension σ_{sl}, the data presented in the aforementioned figures is actually $\Delta\sigma_s = \sigma_{sv} - \sigma_{sl}$, the difference between σ_{sl} and the solid surface tension σ_{sv}. This difference is although not critical since σ_{sv} is a constant.

Copper substrate

For the SnPb/Cu system at 350 °C, the wetting angles for pure Sn and Pb are almost equal (Figure 4.3(a)). For all other Cu systems, the Pb wetting angle is significantly larger than the Sn angle. All solder systems on Cu exhibit their lowest wetting angles at intermediate compositions. For SnBi on Cu the wetting angle minimums are found around $c_{Bi} = 0.3$ for both temperatures, whereas for SnPb

the wetting angle minimums are found close to $c_{Pb} = 0.5$. Although at 500 °C no precise minimum is visible but rather a range $0.2 < c_{Pb} < 0.7$. Finally, a clear discontinuity is observed at ca. $c_{Pb} = 0.65$ in the curve of the SnPb/Cu system at 350 °C, contrary to the other systems which remain continuous.

Nickel substrate

The general forms of the wetting angle curves for the Sn/Ni system (Figure 4.4) are at first glance similar to the Sn/Cu system. Although after closer observation some key differences are visible: i) the curve of the SnPb/Ni system at 350 °C shows no discontinuity, contrary to the SnPb/Cu system; ii) the smallest wetting angle for the SnBi/Ni system occurs for pure Bi at both temperatures, contrary to the SnBi/Cu system which exhibits the largest wetting angle for pure Bi; iii) while the wetting angle is generally smaller at 500°C, the case of pure Bi in the SnBi/Ni system is one exception where the wetting angle is larger (13±1)° at the higher temperature of 500 °C than at 350 °C (5±1)°.

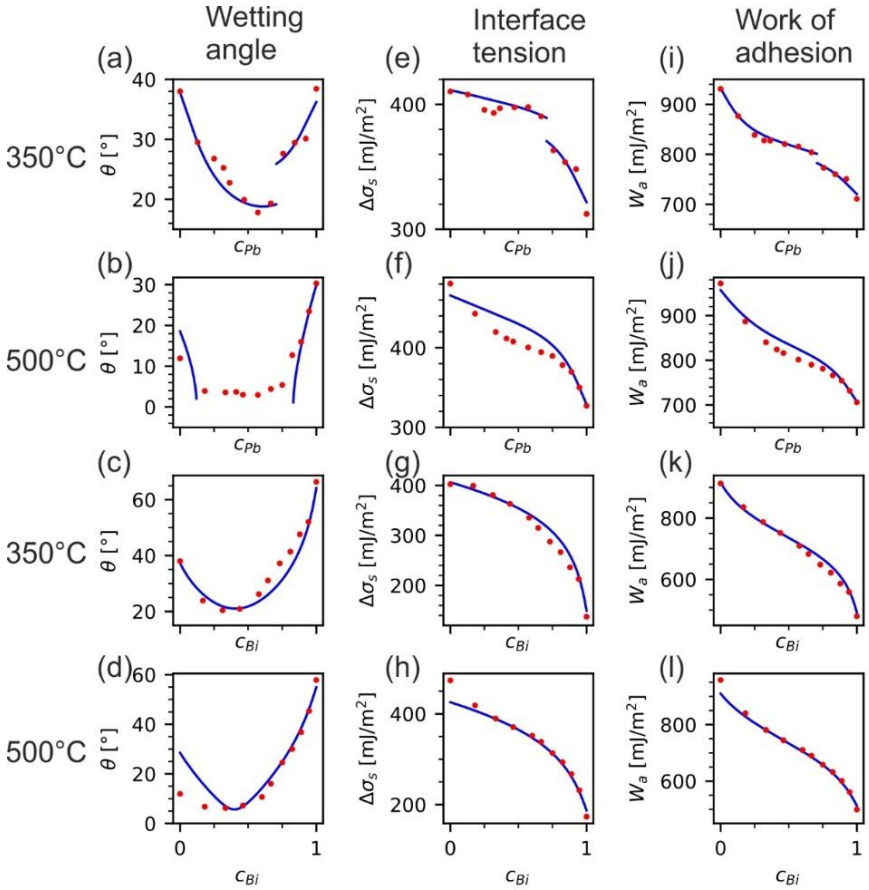

Figure 4.3: (a-d) Wetting angle, (e-h) interface tension $\Delta\sigma_s = \sigma_{sv} - \sigma_{sl}$ ($\sigma_{sv} = \text{constant}$), and (i-l) work of adhesion measurement data (red circles) for SnPb (top two rows) and SnBi (bottom two rows) on Cu substrates. All curves (blue lines) are solutions for the wetting angle, interface tension, and work of adhesion of the melts according to the thermodynamic model previously described using Butler's approach [53] for a sub-regular solution (see section 4.2.3).

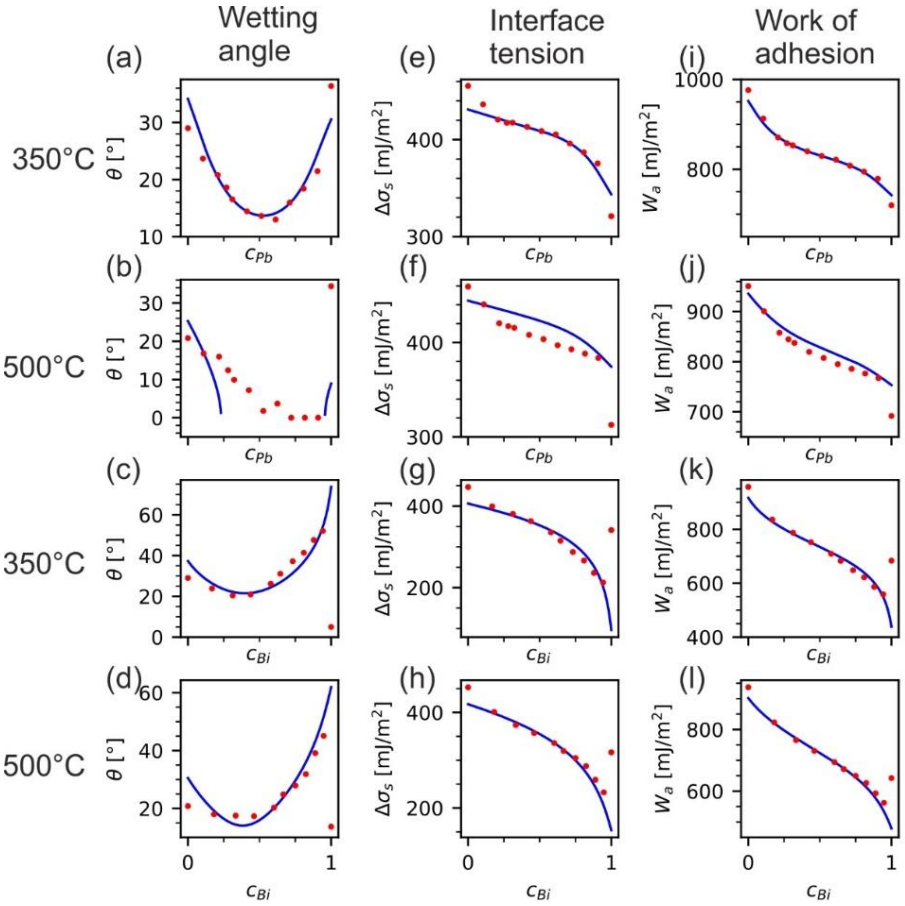

Figure 4.4: (a-d) Wetting angle, (e-h) interface tension $\Delta\sigma_s = \sigma_{sv} - \sigma_{sl}$ ($\sigma_{sv} = \text{constant}$), and (i-l) work of adhesion measurement data (red circles) for SnPb (top two rows) and SnBi (bottom two rows) on Ni substrates. All curves (blue lines) are solutions for the wetting angle, interface tension, and work of adhesion of the melts according to the thermodynamic model previously described using Butler's approach [53] for a sub-regular solution (see section 4.2.3).

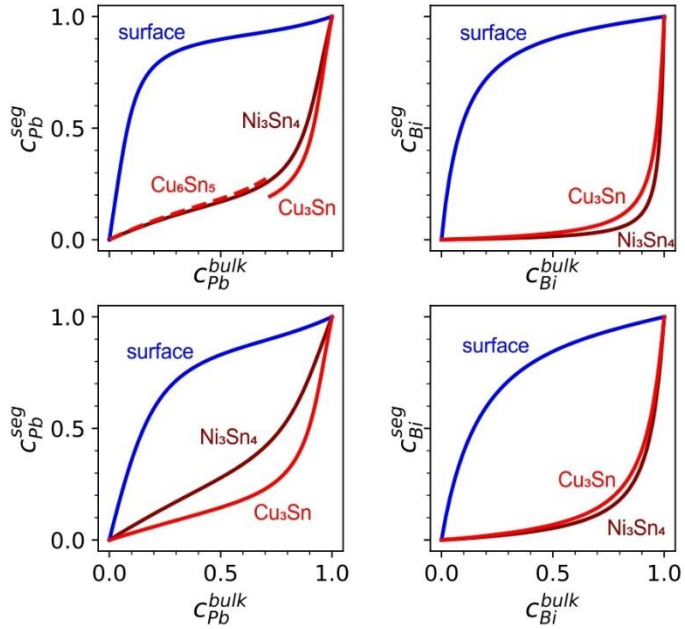

Figure 4.5: Segregation isotherms predicted by sub-regular solution modelling using Butler's approach. (Left side) SnPb solder systems. (Right side) SnBi solder systems. (Top row) modeled based on 350 °C measurement data. (Bottom row) modeled based on 500 °C measurement data [53].

Consumption correction

As mentioned, the thermodynamic model outlined in section 4.2.3 is quite inflexible, only taking the surface tensions of the terminating concentrations as free parameters. This minimizes the possibility of overfitting and maximizes the predictive power of the model. When comparing the measurements with the thermodynamic model, a systematic deviation was found, caused by the reduced Sn concentration in the solder alloys after IMC formation. The quantity of Sn consumed by intermetallic growth is of course dependent on the initial concentration of the solder alloy, requiring a relative correction approach. The solder concentration was corrected as $c_x' = \frac{c_x}{(1-\kappa)c_{Sn}+c_x}$ (x=Pb, Bi), where the fraction of Sn consumed κ was chosen to best match the thermodynamic prediction to the measurements (see Table 4.1). This correction was not required for the modelling of surface tension measurements which is a non-reactive process.

Thermodynamic model

The thermodynamic model predictions of the wetting angles are visible as solid lines in Figure 4.3 and Figure 4.4. The general agreement with the measured results is good. Significant discontinuities over large composition ranges where the model results were undefined are visible in the SnPb/(Cu/Ni) systems at 500 °C which do not otherwise exist in the measurements. These discontinuities define composition ranges which theoretically demonstrate perfect wetting. Thus one may now understand the plateaus of the measured data at $\theta < 3°$ as a range of compositions demonstrating perfect wetting ($\theta \approx 0°$). Furthermore, a discontinuity is observed in the SnPb/Cu system at 350 °C which occurs in no other system. This is a consequence of the composition-dependent stability of the prevailing Cu/Sn IMCs; a detailed discussion follows in section 4.4.3. Some additional deviations are noticeable at high Sn concentrations, particularly at the higher temperature (500 °C). This might arise from the solubility of Cu and Ni in molten Sn which becomes more significant at higher temperatures but is not considered in our binary thermodynamic analysis.

4.3.3 Work of adhesion

Since the same flux environment was used in the surface tension and wetting angle measurements, the work of adhesion could be determined via the Young-Dupree eq. (15). Note that the modeled work of adhesion was calculated via the Dupree eq. (14) as the summation of the modeled surface tension and interface tension $W_a^{model} = \Delta\sigma_s^{model} + \sigma_{lv}^{model}$. The $\Delta\sigma_s^{model}$ term was modeled similarly to the surface tension whereby the terminating terms $\Delta\sigma_{s,x}^{model}$ (x=Sn, Pb, Bi) required as fitting parameters were calculated from the terminating wetting angle and surface tension measurements via eq. (15). The measured and modeled interface tensions and work of adhesions are plotted in Figure 4.3 and Figure 4.4 for Cu and Ni substrates respectively. Some general trends are instantly recognizable: (i) in all cases, the work of adhesion for pure Sn starts at ~950 mNm^{-1}; (ii) in all cases, the work of adhesion then decreases continuously towards the Pb/Bi richer concentrations, first with a steep gradient, than with a slightly flattened gradient at an inflection point, and finally again with a steep gradient; (iii) high lead solders have a work of adhesion ~200 mNm^{-1} higher than bismuth rich solders.

A closer analysis also reveals an increase in the work of adhesion at the transition to Bi pure solder in the SnBi/Ni system, contrary to all other systems. These clearly

contrasting cases highlight the importance of the intermetallic product layer in improving the adhesive properties of solder joints. Aside from the Sn intermetallics formed by all Sn-containing systems, pure Bi/Ni is the only other system to form an intermetallic. A discontinuity is observed in the SnPb/Cu 350 °C case as already seen for the wetting angle. To understand the complex dependence of the work of adhesion on composition, it was also necessary to consider the modeled curve discontinuously; i.e. each continuous portion of the curve was modeled separately, with unique parameters (terminating surface and interface tensions) assigned to each function branch.

4.4 Discussion

Quantitative data and corresponding model predictions for the work of adhesion are presented for the four material systems in Figure 4.3 (i-l) and Figure 4.4 (i-l). In general, the agreement between the measurements and thermodynamic model is good, with measurements at 350 °C showing better consistency with modeled data than 500°C measurements. The lower consistency at 500 °C is likely due to the higher solubility of Cu and Ni in the solder alloys at raised temperatures, which is not considered in our binary thermodynamic model. Nonetheless, the predictive powers of the model with minimal free parameters is impressive (see Table 4.1 for a list of fixed and free fitting parameters). Better fits may be achieved for example by allowing the Redlich-Kister coefficients to vary, although we prefer a more rigid model.

4.4.1 Thermodynamic model and intermetallic roughness

To avoid any influence of surface heterogeneities on the outcome of the wetting angle measurements the metal substrates were initially ground and polished to remove chemical and physical surface defects. This is effective at homogenizing the initial solid substrate, but it has little influence on the inherently random roughness of the intermetallic product phase which forms during the wetting process. The IMC roughness may cause non-ideal effects particularly at the wetting triple-line which are not included in our thermodynamic model. Influences like Wenzel's roughness model or the more complex wetting of grain boundaries [85] should be considered. Yet such dynamic influences can be difficult to quantify thermodynamically. Fortuitously, any influences from the IMC roughness are already contained in the wetting angle measurements, and via eq.

(15) also the work of adhesion, which—at least for the terminating concentrations—are required as fitting parameters for the thermodynamic model. Furthermore, the quality of the fit, particularly at intermediate concentrations, is a strong indication that any compositionally dependent influences of IMC roughness are negligible, although a constant, compositionally independent dependency may exist. Furthermore, advancing contact angles were measured across all datasets, assuring maximum consistency.

4.4.2 Segregation

To completely understand the composition dependence of the work of adhesion, analysis of segregation at the liquid-vapor surface and solid-liquid interface is required. Surface and interface concentration data is obtained as a consequence of thermodynamically modelling the work of adhesion according to eq. (35). The resulting segregation isotherms are provided in Figure 4.5, with bulk concentrations plotted against surface/interface concentrations, providing valuable insight into the segregation tendencies of the different study systems. For example, in all cases segregation is more severe at the lower temperature of 350 °C, resulting as expected from the decreased impact of entropy. Also at the surface, the lower surface energy Pb/Bi components are observed to segregate, whereas Sn conversely segregates to the solid-liquid boundary. This is also to be expected from the increased reactivity and solubility of Cu and Ni with/in Sn. Furthermore, the SnPb solder demonstrates greater surface segregation than the SnBi solder. Conversely, SnBi solder demonstrates greater segregation at the interface than SnPb solder. The effect of segregation on the work of adhesion is clearly visible by the inflection points at $c_{Sn} \approx 0.5$ in the work of adhesion plots (see Figure 4.3 (i-l) and Figure 4.4 (i-l)). The inflection points separate the Sn-rich concentrations for which surface segregation is greater than interface segregation, from Sn-poor concentrations where the opposite is true. This can for example also be visualized by the gradient of the surface tension curves (steeper at Sn rich concentrations) vs the gradient of the interface tension curves (steeper at Sn poor concentrations). This inflection of the work of adhesion curve occurs when the gradient of the individual components are equal $\left(\frac{d\sigma_{lv}}{dc} = \frac{d\Delta\sigma_s}{dc}\right)$. Finally, the SnPb/Cu system at 350°C demonstrates a discontinuous function separating the interface segregation. Sn is observed to segregate more strongly at the Cu_3Sn interface compared with Cu_6Sn_5. A detailed confirmation of this composition-dependent phase transition follows in section 4.4.3. In general, it can be concluded that reactive wetting of the

Sn-rich solders is stabilized by the segregation of Pb or Bi to the surface, whereas Sn-poor solders are stabilized by the segregation of Sn to the interface.

4.4.3 The impact of phase stability on reactive wetting equilibrium

The large set of material systems tested at two temperatures over the full composition range offers a unique opportunity to investigate Eustatopolous' concept [47,67], that reactive wetting equilibria are defined by the energy balance of the triple line resting on the product phase (see Figure 2.13), not the solid phase. Valuable insights are attained from discontinuities in the interface tension and work of adhesion curves. This includes not only the exceptional case of SnPb/Cu at 350 °C but also the Pb/Bi terminating side of all systems which jumps abruptly at pure Pb/Bi. By varying composition, the thermodynamic stability of the product intermetallic can be altered, causing transitions between stable intermetallic compounds at certain critical compositions, which is exemplified as discontinuities in the measurements. These discontinuities can be interpreted as support of Eustathopoulos' concept, that the prevailing intermetallic in contact with the liquid is decisive in the outcome of reactive wetting equilibria.

To confirm the composition-dependent stabilities of the various intermetallics formed by the study systems, phase stability calculations were made. Only binary systems (SnCu, SnNi, SnPb, and SnBi) were considered, based on published CALPHAD (Computer Coupling of Phase Diagrams and Thermochemistry) data, which is a fair approximation since the solder alloys and intermetallics are quasi-binary. The molar Gibbs energy curves were calculated within the CALPHAD scheme based on SGTE (Scientific Group Thermodata Europe) data [53]. The molar Gibbs energy of the binary solutions was calculated by Redlich-Kister polynomials and literature data [86,87] was chosen for the Gibbs energy of pure elements $G_{A,B}^{\phi}$ ($\phi =$ liquid, fcc….)) and the interaction parameter coefficients L_i^{ϕ} which were required as input parameters. Please refer to [74,88,89] for all required models and coefficients.

$$\begin{aligned} G_m^{\phi} = {} & c_A \, {}^0G_A^{\phi} + (1 - c_A) \, {}^0G_B^{\phi} \\ & + RT(c_A \ln(c_A) + (1 - c_A) \ln(1 - c_A)) \\ & + c_A(1 - c_A) \sum_{i=0}^{n} L_i^{\phi} \left(c_A - (1 - c_A)\right)^i \end{aligned} \tag{37}$$

Figure 4.6 presents the calculated molar Gibbs energy curves vs concentration showing various composition-dependent phase stabilities [53]. The Cu/(SnPb/SnBi) system is plotted in (a) for 350 °C and (b) for 500 °C, and the Ni/(SnPb/SnBi) system is plotted in (c) for 350 °C and (d) for 500 °C.

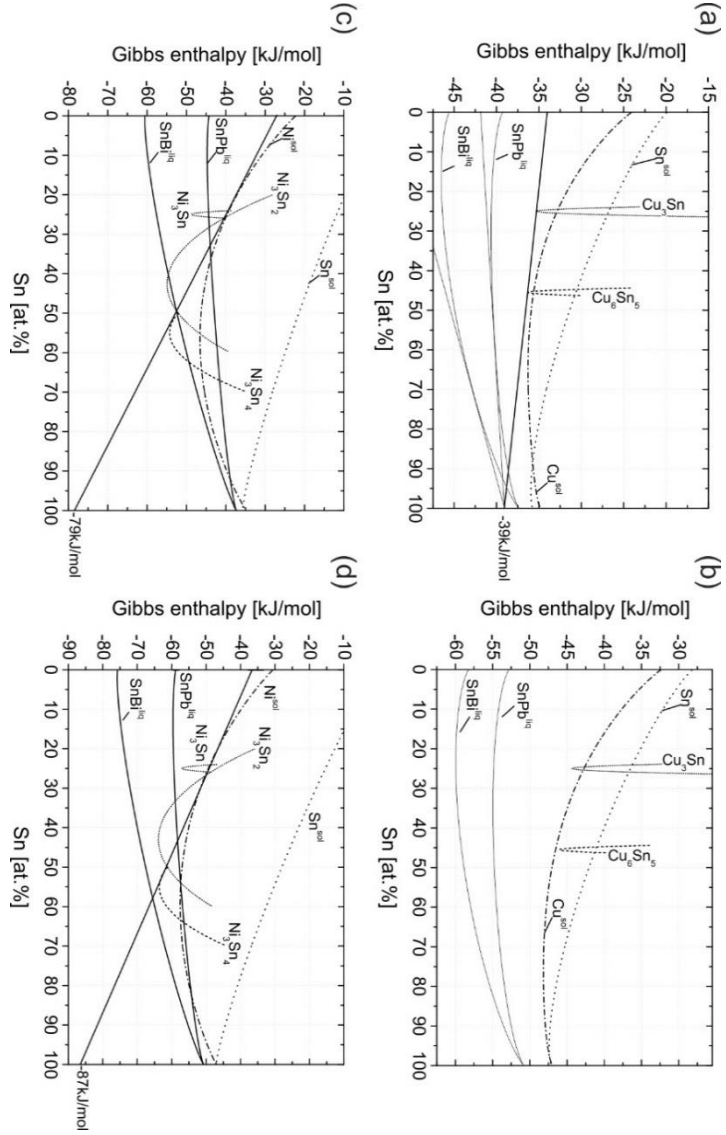

Figure 4.6: Molar Gibbs energy curves calculated with the CALPHAD approach. Each plot contains both SnPb and SnBi solders and one substrate temperature combination: Cu substrates at (a) 350 °C and (b) 500 °C. Ni substrates at (c) 350 °C and (d) 500 °C[53].

Note that although the calculated liquid solder curves (SnPb, SnBi) contain one component (Pb, Bi) which is not quantified in these binary plots, there is utility in plotting them because the relative phase stabilities at the pure Sn right-hand side of the phase diagram are well defined. Nonetheless, the left-hand sides of the liquid curves were set arbitrarily. Considering first the system of Cu substrate at 350 °C, it is clearly visible that both the Cu_6Sn_5 and Cu_3Sn phases may coexist. Drawing a double tangent between the intermetallic Gibbs energy curves determines a minimum Sn chemical potential of -39 kJ/mol necessary to form the Cu_6Sn_5 phase. As seen by the tangent on the $SnPb^{liq}$ curve, this minimum chemical potential of Sn is exceeded for Sn concentrations larger than 57 at%. A similar evaluation of Cu_3Sn stability reveals a minimum necessary chemical potential of -72.5 kJ/mol for Sn (tangent not displayed). Such a low Sn chemical potential is already exceeded by a Sn-based solder with a concentration of 1 at% Sn. Thus from a thermodynamic standpoint, one would expect the Cu_6Sn_5 intermetallic to be stable for high Sn concentrations above 57 at% Sn, and the Cu_3Sn intermetallic to be stable at all other concentrations, except for almost pure Pb/Bi at which composition the inherent Cu substrate remains stable.

The conclusions drawn from the CALPHAD calculations deviate slightly from the measured data. Contrary to the CALPHAD predicted Cu_6Sn_5/Cu_3Sn phase transition at 57 at% Sn, the measured data for the work of adhesion demonstrates a transition from 40 at% Sn where Cu_6Sn_5 appears to be stable, to 30 at% Sn where only Cu_3Sn appears to be stable. This deviation may be a consequence of kinetic effects, for example, the higher mobility of Cu in Cu_6Sn_5 compared with Cu_3Sn. The solubility of Cu in the SnPb liquid phase may also shift the phase stabilities to different concentrations. Independent of these theoretical considerations, SEM micrographs and composition profiles from EDX line-scans were obtained from sample cross-sections (see Figure 4.7(a-l)). For the Cu/SnPb system at 350 °C the prevailing intermetallics are clearly observed: for 40 at% Sn (a, b) thick layers of both Cu_6Sn_5 and Cu_3Sn are formed; whereas for 30 at% Sn (c, d) only Cu_3Sn is formed. Thus the Cu_6Sn_5 phase is suppressed for concentrations at least below 30 at% Sn, at which concentration the SnPb solder no longer rests on the Cu_6Sn_5 IMC but rather the Cu_3Sn IMC. This transition corresponds to the discontinuous shift in the work of adhesion vs concentration curve in Figure 4.3 (a). These composition profiles completely support the utility of Eustatholoulus' concept in predicting the wetting and adhesive properties of binary solder alloys.

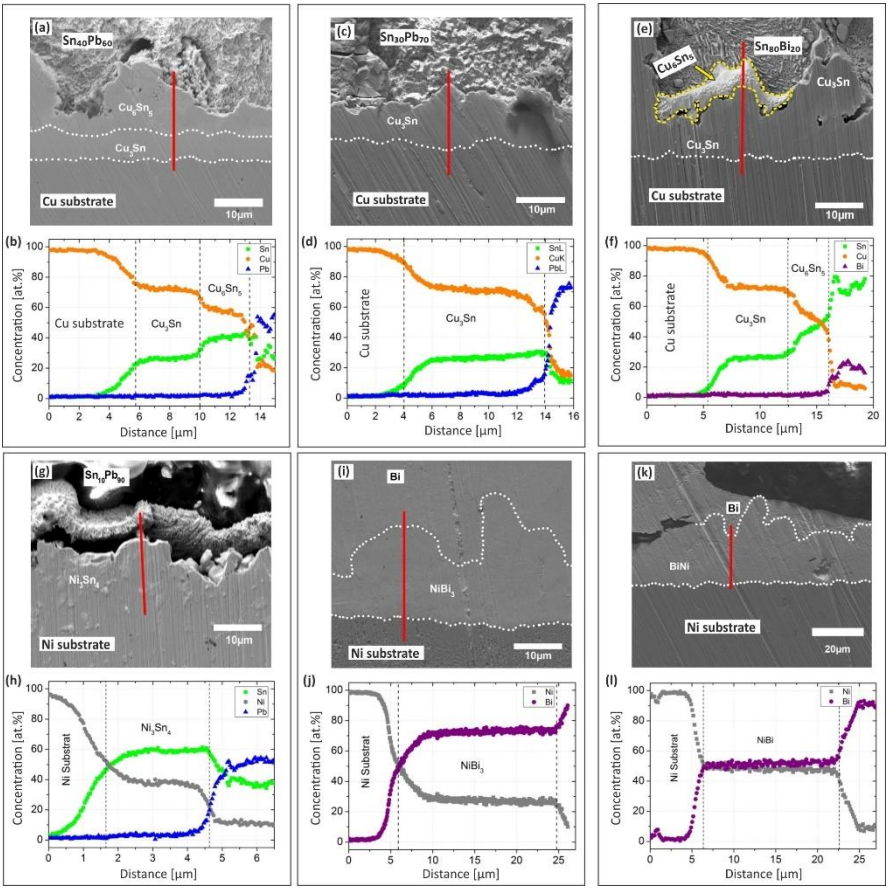

Figure 4.7: SEM micrographs and corresponding composition profiles by EDX directly below. (a, b) $Sn_{40}Pb_{60}$/Cu system at 350 °C. (c, d) $Sn_{30}Pb_{70}$/Cu system at 350 °C. (e, f) $Sn_{80}Bi_{20}$/Cu system at 350 °C. (g, h) $Sn_{10}Pb_{90}$/Ni system at 350 °C. (i, j) Bi/Ni system at 350 °C. (k, l) Bi/Ni system at 500 °C [53].

Considering the SnPb/Cu system at 500 °C, the Gibbs energy curves (Figure 4.6 (b)) confirm only the Cu_3Cn intermetallic phase to be stable. As expected, there are no discontinuities in the corresponding work of adhesion curve (Figure 4.3 (j)), contrary to the lower temperature case. For SnBi solder on the same Cu substrate at 500 °C system, the thermodynamic expectations are analogous, as is the measured work of adhesion trend (Figure 4.3 (l)). The two solders do not although

result as similarly at 350 °C on Cu, where the work of adhesion of SnBi contrary to SnPb displays a continuous trend with varying concentration (Figure 4.3 (k)). This is surprising when considering the Gibbs energy curves (Figure 4.6 (a)). The chemical potential of Sn is sufficient ($\mu_{Sn} > -39$ kJ/mol) to form the Cu_6Sn_5 phase at ca. 70 at% Sn, yet no discontinuity is visible in the measured data. Thus we again look to the interface cross-section (Figure 4.7 (e,f)) and find that the Cu_6Sn_5 phase does exist above 70 at% Sn but only partially covers the interface. So the solder logically contacts both intermetallics, indicating that there may be a broader IMC transition range where the fraction of interface covered by Cu_6Sn_5 gradually increases with at% Sn, resulting in a continuous transition.

Now we consider the two solders on Ni substrates. From the thermodynamic plots, Gibbs energy curves of several stable IMC phases are visible at both temperatures. Although from experiment we find that only the Ni_3Sn_4 intermetallic is formed during the reflow process across all Sn-containing solder alloys, even with as little as 10 at% Sn (Figure 4.7 (h)). This is likely a result of a superior kinetic growth rate compared with the other phases. Furthermore referring to the thermodynamic plots (Figure 4.6 (c,d)), the Sn chemical potential required to form the Ni_3Sn_4 phase is so low ($\mu_{Sn}^{350\,°C} = -79$ kJ/mol and $\mu_{Sn}^{500\,°C} = -87$ kJ/mol) that it will already be formed by solders with a Sn content of 1 at%. Logically the only possible exception occurs for the cases of pure Pb and Bi solder. Indeed the measured data for both solders on Nickel substrates do demonstrate continuous trends across the entire composition range, deviating only at the pure Pb and Bi concentrations. Strikingly, the measured data for the Sn-free concentrations display deviations in the exact opposite directions. For example for pure Pb, the work of adhesion exhibits a sudden drop (ca. -100 mJ/m^2), whereas a significant increase (ca. 100 mJ/m^2) is observed for pure Bi (Figure 4.4 (i-l)). So we may conclude that the adhesion strength of Bi on Ni is not only stronger than pure Pb but also SnBi solder alloys with a low Sn fraction. This exceptional case results from the reactivity between Bi and Ni. According to the Bi-Ni phase diagram [90] two IMCs are stable: BiNi below 614 °C and Bi_3Ni below 470 °C. Obviously, the Bi_3Ni phase is thermodynamically unstable at 500 °C and by examining the relevant interface cross-section (Figure 4.7 (k)) the BiNi phase is indeed the only IMC observed. So we may expect that both IMCs are formed for the 350 °C measurements of pure Bi on Ni, but in fact, only the Bi_3Ni phase is observed (Figure 4.7 (k)), at least within the resolution on the EDX measurement. It may be concluded that the NiBi phase is suppressed owing to poorer growth kinetics relative to Bi_3Ni. Furthermore, comparing the work of adhesion measurements of pure Bi on Ni at

both temperatures, we observe a small increase in the joint adhesion strength owing to the temperature-driven transition between BiNi at 500 °C and Bi_3Ni at 350 °C. This is caused by the lower interface tension of the Bi_3Ni phase relative to the BiNi phase (Figure 4.4 (g,h)).

To summarize, the combination of the presented measurements, thermodynamic investigations, and chemical analysis strongly corroborate the concept of Eustathopoulos that reactive wetting equilibria are best defined by considering the interface tension of the uppermost IMC in contact with the liquid phase, rather than the surface tension of the inherent substrate. For a bi-metallic system on a metallic substrate, this can be well modeled using the approach of Butler with a sub-regular solution model, and only requiring prior measurement of the pure components of the alloy. It may provide good predictions of experiment with minimal corrections required, and independent of any neglected phenomenon (triple-line effects, spreading rate, IMC roughness). Alternatively, including a term for the Gibbs energy of formation in Young's equation seems less reasonable.

5 Effects of miniaturization and surface roughness on reactive solder joints

In the previous chapter, we broadly focused on the relationship between reactive wetting equilibria and the stabilities of the intermetallic compounds which are produced during reactive wetting processes. The results clearly highlighted that reactive wetting equilibria (wetting angles, interface energies) in dependence on solder composition vary most abruptly across concentration-dependent transitions of the uppermost interface in contact with the liquid solder. In other words, reactive wetting equilibria are largely controlled by the prevailing product phase. It should be noted that the size of the solder balls used in the measurements was constant and logically the main conclusion of the study was size independent. Nonetheless, this does not mean that solder reflow behavior is generally size independent. In this chapter, we investigate how reactive wetting behavior is influenced by solder joint miniaturization

5.1 Introduction

Technological research and development relating to micro-soldering continues to be driven by the microelectronics industry. As manufacturing technologies improve, the size of solder joints inevitably continues to decrease. Many recent scientific studies are aimed at understanding and finding solutions to the difficulties inherent to the increasingly miniaturized solder joints. The research efforts are predominantly focused on such phenomena as electromigration [44,91,92], thermomigration [44], and joint embrittlement [93]. Yet the influence of joint miniaturization of the reactive wetting behavior has been largely overlooked. The contact angle (CA) is the most common metric used for evaluating a joint's wettability since the measurement of other quantities like the interface tension can only be done indirectly (e.g. via eq. (15)) and are experimentally more demanding. Contact angles are described by Young’s equation (11) for ideal systems. The surfaces of real systems are although generally heterogeneous. To better describe wetting on rough surfaces, Wenzel

extended Young's equation (16) by including a roughness parameter r, which defined the ratio of the real rough surface area to the projected planar surface area (see section 2.2.5). In other words, the roughness parameter accounts for the increased surface area of a rough surface relative to a smooth surface. As discussed in section 2.2.5, the roughening of a surface causes wetting systems ($\theta < 90°$) to wet better ($\theta_{\text{rough}} < \theta_{\text{ideal}}$) and dewetting surfaces ($\theta > 90°$) to wet worse ($\theta_{\text{rough}} > \theta_{\text{ideal}}$). This phenomenon is by definition non-hysteretic; i.e. it is independent of the path taken to arrive at the final C. But contact angles for a given wetting system are inevitably hysteretic, demonstrating a range of CAs ranging from the advancing CA, θ_{a} to the receding CA, θ_{r}. The degree of CAH may vary significantly dependent on the system and cause of hysteresis, yet to the best knowledge of the author, no study exists proving the existence of a non-hysteretic wetting system. This may simply be a result of practical limitations concerning the preparation of ideal substrates and measurement environments, which are a prerequisite for measuring non-hysteretic contact angles. Nonetheless, past studies investigating the influence of the elastic deformation of a wetted substrate surface in the normal direction at the triple line suggest that wetting systems will always exhibit a degree of CAH [5,38], since no solid is perfectly rigid. In real wetting systems, substrate surface imperfections like surface roughness and chemical heterogeneity are generally the predominant cause of CAH. From this point on we will only discuss rough hysteretic systems, although the main concepts, arguments, and conclusions that follow are to a large extent transferable to the case of chemical heterogeneity.

Although somewhat contentious, it is generally understood that CAH results from defects in the vicinity of the triple line during the spreading process. These defects may be pre-existing or have formed during spreading. As discussed in section 2.3.1, the spreading triple line must overcome these defects which act as energy barriers to the continued movement of the triple line. For an advancing droplet on a rough substrate, the CA decreases as the triple line advances towards equilibrium. Logically, if the triple line is hindered to reach equilibrium then a metastable state will ensue and the resulting CA will be larger than the equilibrium CA. In other words, for an advancing triple line surface asperities or undulations cause an increase in the static CA. Shuttleworth and Bailey [21] first popularized the theory of CAH on rough undulating surfaces. Their theory was later extended by Johnson and Dettre [20] who measured advancing and receding CAs of water on wax substrates of differing roughness and found varying degrees of CAH as well as shifts in θ_w. Huh and Mason [19] later conducted a deeper theoretical

evaluation whereby they used perturbation theory to predict the apparent CA of a liquid droplet on a 2-dimensional right-angled periodic sinusoidal surface (cross-grooves). They predict that: (i) the CAs fluctuated with droplet size; (ii) the fluctuations decreased with increasing drop volume. The trends of the volume-dependent CA fluctuations were suggestive of CAH, and they recommended that experiments should be conducted to test the utility of their model in predicting CAH. Joanny and De Gennes investigated triple line pinning by designing a mathematical description for individual Gaussian-shaped surface defects which acted as pinning centers. Furthermore, they introduced the spring constant k of the bending triple line at local perturbations [94]. Their microscopic description is insightful, yet difficult to scale up and apply as a predictive model for real surfaces with densely packed defects.

Generally, the form and evolution of the triple line during spreading is not well understood and although studies have shown that surface irregularities directly at the triple line critically influence CAH [20], the ability to predict the outcomes remains incomplete. This is largely a result of the random nature of real rough surfaces and the complex interaction between surface irregularities and the triple line. Nonetheless, attempts have been made to model CAH, for example by investigating simulated or artificial surfaces of identical periodic asperities [29,60,61,95–98]. The predictive precision of such descriptions is although limited by the regularity of the rough surfaces. Some groups have alternatively introduced an effective triple line energy term ϵ_t as a property of the triple line, which although does not represent the real excess energy of atoms with broken bonds along the triple line [28,44–46]. The effective triple line energy can be applied as an extension to Young's equation and is thus an advantageous parameter offering a simple method to describe CAH and size related effects. Furthermore, one could consider modelling ϵ_t based on the geometry and distribution of the surface asperities as an extension to the model. Unfortunately until now, the drop size dependence of CAs has only scarcely been discussed [99,100], and even then only for polymeric substrates without providing information about the materials surface topology.The majority of past wetting hysteresis studies concerned non-reactive systems (including those cited in this section thus far) and the relationship between surface roughness and reactive wetting CAs has been largely overlooked, probably due to the added complexity of the dynamic reactive product phase. Some past reactive wetting studies have concerned themselves with composition dependencies [53,64,101]. Other studies have focused on reactive wetting kinetics [102–104] (although many questions remain unanswered, see chapter 6) and

further experimentation is required to corroborate their interpretations of the rate-limiting phenomena. But the effect of droplet size or roughness on reactive wetting equilibria remains unanswered.

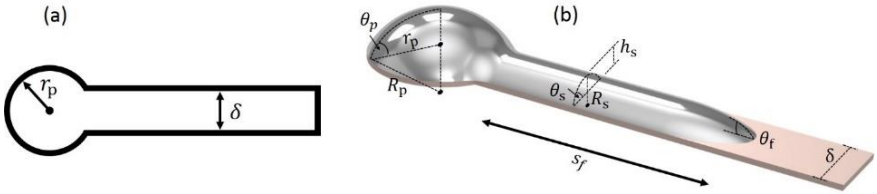

Figure 5.1: (a) Geometry of the metallization lollipop structure. (b) 3D schematic of solder on a metallization after reflow (not to scale). The molten solder (silver color) first forms a cap on the circular pad (left side) and then flows from the pad along the strip (right side) until the liquid equilibrates.

The present study seeks to elucidate the relationship between solder size and reactive wetting behavior. To achieve this broad goal, we conduct reactive wetting measurements on both structured and unstructured substrates. The unstructured substrate measurements are primarily aimed at investigating surface roughness as an additional free parameter (see section 5.3), whereas the structured substrate measurements are focused solely on the impact of solder joint miniaturization. Our reactive wetting experiments on structured substrates are based on a technique introduced by Hosking et al. for investigating the spreading behavior of solder [105]. They produced "lollipop" shaped metallization test geometries along which solder could spread, consisting of a circular reservoir which we call the "pad" attached to a long track which we call the "strip" (see Figure 5.1). The pad and strip of the test structure are similar to the contact pads and surface traces of printed circuit boards in surface-mount design [106]. By placing solder on the pad and raising the temperature above the solder melting point, the ensuing molten solder first spreads to the pad perimeter forming a spherical cap, and then precedes to spread along the strip under the condition that the Laplace pressure of the solder on the pad ΔP_p is larger than the pressure along the strip ΔP_s:

$$\Delta p_p - \Delta p_s \geq 0 \tag{38}$$

Once this condition is no longer fulfilled, the solder will cease to flow. Neglecting gravitational effects, the Young-Laplace equation for the pad and strip pressures take the form:

$$\Delta p_p = \frac{2\gamma_{lv}}{R_p} = \frac{2\gamma_{lv}\sin\theta_p}{r_p} \tag{39}$$

$$\Delta p_s = \frac{\gamma_{lv}}{R_s} = \frac{2\gamma_{lv}\sin\theta_s}{\delta} \tag{40}$$

Where R_p and R_s are the radius of curvature of solder on the pad and strip, r_p is the pad radius, δ is the strip width, and θ_p and θ_s are the contact angles of solder on the pad and strip respectively. The factor of 2 in eq. (39) comes from the pad solder geometry which approximately forms a spherical cap, for which by definition both principal curvatures are equivalent. R_s and θ_s are measured on the cross-sectional-plane normal to the length of the strip. The solder along the strip is approximated to form a horizontal cylindrical segment and so the Laplace pressure is fully defined by one principal radius term. The factor of 2 in eq. (40) represents a halving of the strip width δ. At equilibrium ($\Delta p_p = \Delta p_s$), the combination of eqs. (39) and (40) define a necessary geometric condition:

$$\frac{\sin\theta_p}{r_p} = \frac{\sin\theta_s}{\delta} \tag{41}$$

Lastly, the solder front contact angle θ_f is the only true wetting angle for which triple line spreading is uninhibited, i.e. θ_f is ideally controlled by the equilibrium of surface and interface tensions rather than the metallization geometry and relates intimately to properties of the material system we aim to study. Logically, the free spreading front wetting angle also has some control over the final shape of the solder including its height on the pad h_p and strip h_s which are closely related to the solder geometry parameters in eqs. (39) and (40).

In the original work of Hosking et al. [105], they only argued their results qualitatively and did not provide any phenomenological arguments for their findings. They found the statistical error to increase for the narrower strip widths and attributed this to hysteresis without further microscopic analysis. Furthermore, their experiments were limited to only one material system (eutectic SnPb solder on Cu) using test structures with a smallest pad radius of 1 mm. With this study, we intend to (i) extend the work of Hosking by further decreasing the sizes of the

structures, measuring an additional material system (eutectic SnPb on both Cu and Ni substrates), and completing a deeper phenomenological analysis; and (ii) investigate the relationship between joint size, surface roughness, and CA by conducting various measurements on unstructured substrates. In this way, we may offer a more complete description of the relationship between the geometric and energetic properties and the prevailing reactive wetting equilibria.

5.2 Experimental – structured substrates

Reactive wetting experiments were conducted by reflowing eutectic SnPb solder balls on Cu and Ni metallization strips upon which the solder would spread. The geometry of the metallization samples including the key defining parameters r_p and δ are depicted in Figure 5.1 (a). Rather than scaling down the entire metallization structure, variation of the sample size was achieved by varying δ and holding r_p constant, thus the samples were defined by their δ/r_p ratio. In this way the influence of solder width on wetting equilibrium could be investigated while keeping the solder volume constant. Furthermore, the pad radius is decisive in controlling the initial pressure of the molten solder which forms a cap on the pad. It was important to choose the geometrical dimensions of the metallizations carefully, since each metallization of a chosen δ/r_p ratio was measured several times for improved statistics. In choosing the geometries the following considerations were necessary:

- The chosen geometries should be equivalent for Ni and Cu metallizations for comparability, although the interface energies and wettability of the two systems vary.
- The array of different sizes should be sufficiently dissimilar to maximize any size effects.
- The ratio δ/r_p should be sufficiently large so that the conditions (38, 41) are satisfied.

Based on these considerations, the chosen geometries are provided in Table 5.1. The following sections will briefly outline the methods of sample preparation, as well as post-measurement sample evaluations.

Table 5.1: List of metallization geometries used in the solder reflow wetting experiments.

Geometric ratio, δ/r	Pad radius, r [μm]	Strip width, δ [μm]	Substrate
0,4	250	100	Cu only
0,6	250	150	Cu/Ni
0,8	250	200	Cu/Ni
1,0	250	250	Cu/Ni
1,2	250	300	Cu/Ni
	500	700	Cu only

5.2.1 Metallization preparation

For a detailed description of the sample production procedures, please refer to Chapter 3, Experimental methods. An approximately 1 cm x 3 cm silicon dioxide chip was cut from a polished wafer. Using sputter deposition, a ca. 10 nm adhesion layer of Cr and a ca. 12 nm seed layer of Cu or Ni were coated on the chip. The Cr layer thickness was not critical, but the seed layer thickness was minimized since it would be later etched. Using direct laser writing lithography, the form of the desired metallization geometry was structured into positive photo-resist. The metallization was electrodeposited onto the exposed portion of the substrate using an electrolytic cell. The photoresist was removed with acetone and the Cu or Ni seed layer was etched exposing the Cr or oxide layer of the substrate, neither of which interacts strongly with eutectic SnPb solder.

5.2.2 Solder ball preparation

Eutectic SnPb solder balls were prepared for wetting experiments on both Cu and Ni substrates since it offers a low melting point and favorable wettability promoting the flow of solder along the metallization. Nonetheless, the findings of this study are probably applicable to other reactive wetting systems. Generally one may choose a solder ball mass corresponding to the volume of a hemisphere with the same radius as the pad since this will provide the maximum initial pad pressure promoting the flow of solder. Alternatively, we produced solder balls weighing 400 ± 15 μm which corresponds to ¾ the mass of the sphere of radius $r_p = 250$ μm, whereby we offer more material, sacrificing the initial pad pressure to maximize the flow distance. The solder balls were produced by cutting and

weighing small shards of solder and melting them into balls using the reflow procedure outlined in section 3.2.2.

5.2.3 Reflow experiment

A sample metallization was thinly coated with RMA flux, then a solder ball was placed on the metallization pad which was also coated with a drop of RMA flux. The sample was placed on the heating plate of the vacuum furnace and the reflow experiment was conducted using a reflow temperature of 300 °C and otherwise as outlined in section 3.2.2. The solder spreading along the metallization was observed in-situ and a video was recorded through the top chamber window. The spreading generally ceased after 2-3 minutes and the heating stage was switched off about 30 seconds after the spreading had visibly stopped, which is sufficient time for the wetting angles to equilibrate according to trial experimental as well as a previous study of the Cu/SnPb system [53]. Finally, the contact angles of the solder (see Figure 5.1 (b)) could not be measured in-situ, primarily due to resolution limitations and vision impairment from smoke given off by the flux.

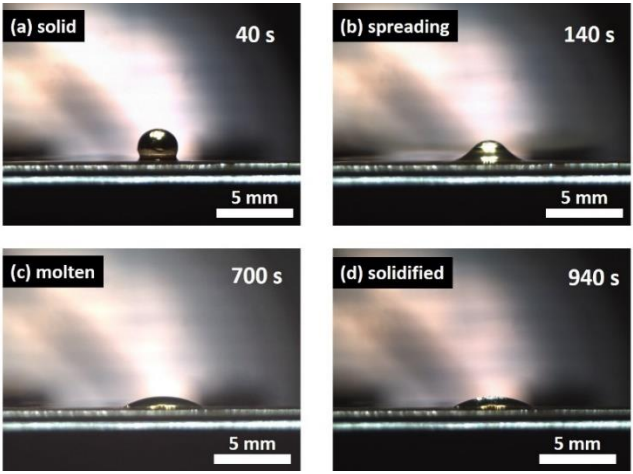

Figure 5.2: The evolution of RMA flux coated eutectic SnPb solder during reflow on an unstructured Cu surface. Within the optical microscope resolution, no variation of the wetting angle was measured after solidification of the solder cap (bottom sub-figures). The CAs of both the molten and solidified droplets (after spreading had ceased) were measured to be 30°.

A reflow measurement of a larger solder ball was conducted to compare the wetting angle of the droplet in both the molten state and solid-state after solidification (see Figure 5.2). No resolvable variation of the CA was measured before and after solidification of the solder cap, confirming that ex-situ measurements of solidified CAs (at least for SnPb solder) are a sufficiently accurate representation of real wetting angles.

5.2.4 Wetting evaluation

After the reflow experiment, various geometric properties of the solder were measured. The spreading or flow distance s_f was measured via optical microscopy, defined as the length between the solder front and the boundary between the pad and strip. Side-view SEM micrographs of the pad and solder front (see Figure 5.3 (a,b)) were imaged using an FEI Quanta 250 SEM and the CAs (θ_p, θ_f) were measured from the micrographs using the wetting angle fitting plug-in of Image-J, "Low Bond Axisymmetric Drop Shape Analysis" (LBADSA) [69].

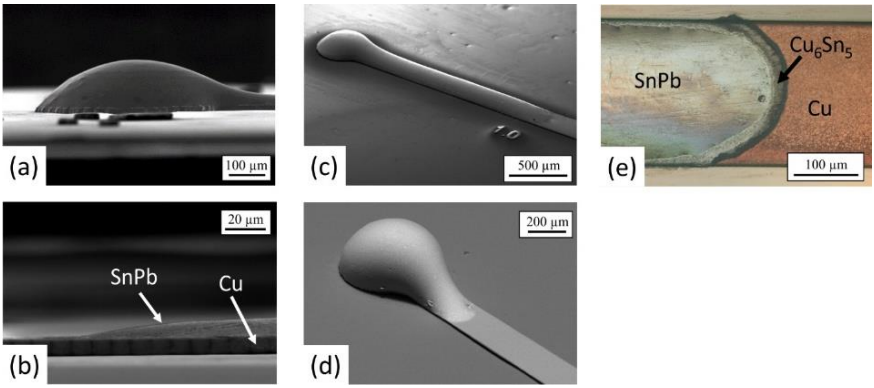

Figure 5.3: SEM and optical micrographs of Cu/Ni samples after reflow and solder spreading. SE-SEM micrographs of (a) solder on a Cu pad and (b) solder at the spreading front. BSE-SEM micrographs of solder on Ni metallizations were (c) $\delta/r_p = 1.0$ and (d) $\delta/r_p = 0.6$. The larger pressure on the narrower strip hinders spreading. (e) A top-view optical micrograph of a solder front showing the typical intermetallic phase extending beyond the triple line [106].

The final CA θ_s was difficult to measure directly due to the sample geometry and was instead determined trigonometrically from the solder height on the strip assuming a constant radius of curvature across the strip as:

$$\theta_s = 2\tan^{-1}\left(\frac{2h_s}{\delta}\right) \quad (42)$$

5.2.5 Cu grain microstructure investigation

As can be seen in Figure 5.3 (e), the surface of the electroplated samples were microscopically rough. Considering that this roughness is probably directly related to the grain size, the grain size distribution of the electrodeposited Cu metallizations was determined using Electron-Backscatter-Diffraction (EBSD). EBSD is the technique by which an electron beam (typically in an SEM) directed onto the polished surface of a sample penetrates the surface and scatters within the volume, emitting backscattered electrons (BSE) forming diffraction patterns that can be detected by a phosphorous screen and CCD camera. The BSE diffraction patterns are characteristic of a particular crystal structure and orientation and can be used to compose a 2D grain orientation map of a material's microstructure.

The Cu metallization was electrolytically etched in an aqueous solution of 50% sulfuric acid (H_3SO_4) by applying a manually controlled pulsating voltage of ca. 5 V. An EBSD measurement was conducted on the smooth etched surface of the Cu metallization using an FEI Scios Dual-beam microscope and the obtained EBSD micrograph is presented in Figure 5.4 (a). To extend our investigation of the surface structure, the surface roughness was directly measured via white light interferometry. This technique relies on the interference between a static reference beam and a measurement beam which scans normal to the sample surface plan. When the path length of the reference and measurement beam to the CCD camera are equal, all wavelengths will constructively interfere. In this manner, the relative height (roughness) across the sample surface can be determined by tracking the relative displacement of the maximum interference fringe. A topological roughness map of a Cu metallization sample obtained by white light interferometry is presented in Figure 5.4 (b). Finally, due to the low resolution of

Figure 5.4 Surface microstructural and morphological evaluation of Cu metallizations. (a) EBSD micrograph of a Cu (FCC) metallization sample, demonstrating some texturing. (b) Topographic height map obtained by white light interferometry. (c) Atomic force micrograph providing higher spatial resolution exposing the finer nanoscopic details which are not resolved by white light interferometry.

white light interferometry, AFM investigations were also conducted. This method is restricted to investigating smaller areas but provides a transverse resolution approximately 2 orders of magnitude higher than white light interferometry. The results are provided in Figure 5.4 (c).

From the EBSD investigation, the number average and area average grain sizes were determined to be $\overline{d_N} = 6.38\,\mu m$ and $\overline{d_A} = 11.29\,\mu m$ respectively. As determined from the white light interferometry measurement, the maximum roughness height was $s_z \approx 1.5\,\mu m$ and the arithmetical mean roughness and root mean square roughness were $S_a = 82$ nm and $S_q = 104$ nm respectively. These values should although only be considered as estimations, as white light interferometry has difficulty resolving steep slopes of rough surfaces, which do not back-reflect light effectively. The AFM measurement shows a height variation of ca. 1 µm and provides a more detailed picture of the surface roughness which demonstrates surface asperities with a heterogeneous distribution of magnitudes. Although the AFM measurement provides a high resolution, the sampled area is limited. Thus we gain insight into the expected magnitude of the roughness of the electroplated Cu substrates. But this information should only be considered as an approximation across all samples, from which we may later draw upon in discussions of the influence of roughness on reactive wetting.

5.3 Experimental - unstructured substrates

5.3.1 Sample preparation

Additional to the experiments conducted on structured electrodeposited substrates, reactive wetting has also been investigated on unstructured substrates. In this case, the impact of substrate surface roughness is of foremost interest. To this end, we investigate reactive wetting of pure Sn on both rough electrodeposited Cu substrates and smooth polished Cu platelets. The polished substrates were prepared from 1×2 cm Cu platelets which were ground with incrementally-finer-grained grinding paper until 4000 grit and finally polished using a polishing cloth with 0.25 µm Struers diamond paste. The rough samples were prepared by electrodeposition of Cu (see section 3.1.4) onto sputtered silicon chips (see section 3.1.2). Two electrolyte compositions were used to achieve surface finishes of different roughness. The standard copper sulfate electrolyte listed in Table 3.2 produced surface finishes similar to the structured lollipop substrates. The addition of boric acid (H_3BO_3) and extra sulfuric acid (H_2SO_4) to the standard electrolyte allowed for a different, rougher surface finish. Generally, boric acid is used as a pH buffer and the additional sulfuric acid increases the electrolyte conductivity and the Cu ion solvability which impacts the surface finish.

Sn micro solder balls were used as solder on the unstructured substrates. They were produced from 99.99% purity bulk Sn. Sn particles were created by grinding the bulk Sn on SiC grinding paper and catching and storing the ground Sn particles. The Sn particle size was varied by using grinding paper of varying grit. The captured Sn particles were melted on quartz glass transforming them into spheres, according to the reflow procedure outlined in 3.2.2.

5.3.2 Reflow experiment

Contrary to using eutectic SnPb solder for the structured substrate wetting experiments, for the unstructured substrates, we have chosen to use pure Sn. The reason is simple; solder systems which exhibit small CAs are favorable within the context of our narrow structured samples, as they promote spreading along the strip of the lollipop structure (this will become clearer in results section 5.4.1). In the case of unstructured substrates, it is favorable to investigate wetting systems that demonstrate moderate wetting CAs ($30\,° < \theta < 60\,°$). This is firstly, because CAs in this range are easily measured (here, the favorable wettability requirements of the structured substrates are no longer required) and secondly, because deviations of the measured CA from the ideal CA (i.e. $\Delta\theta = \theta_{ap} - \theta_0$) which result from surface irregularities are more sensitive compared to cases where $\theta_0 \rightarrow 0°, 90°$.

Reflow experiments were conducted similarly to the patterned samples (and as outlined in section 3.2), except that several solder balls (up to ca. 20) of varying volume were melted on a single sample. This assured consistent measurement conditions for all solder balls. Due to the minute volume of the smaller solder balls and the potential for high consumption of Sn to the reaction phase, it was necessary to reduce the reflow time. But the spreading state of the smaller solder balls could not be resolved in-situ in the optical microscope. Accordingly, the reflow holding time was reduced to 1 min for all measurements (compared to ca. 2-3 min for the structured samples) which, based on experimental observations, is sufficient time for the largest measured solder balls to visibly stop spreading and by extrapolation also the smaller solder balls. The CAs of all solder caps were evaluated similarly to the structured substrate measurements: the CAs were imaged with an SEM and measured using ImageJ. Table 5.2 provides an overview of the preparation and measurement conditions of each sample.

Table 5.2: Overview of the measurement conditions and preparation details of each sample.

Sample #	Surface finish	Reflow holding temperature [°C]	Preparation	Electrodeposition	
				I [mA]	*t* [min]
1	rough	280	electrodeposited	30	60
2	rough	350	electrodeposited	20	60
3	rough	350	electrodeposited	50	15
4	rough	270	electrodeposited (boric acid + sulfuric acid added to standard electrolyte)	100	20
HT	smooth	350	ground/polished	-	-
LT	smooth	242	ground/polished	-	-

5.3.3 Brief in-situ reactive wetting observation

To assist in the evaluation of reactive wetting behavior, it would be beneficial to understand how the spreading triple line behaves dynamically. To achieve this, it is necessary to observe the triple line configuration and movement locally and in-situ. At the microscopic scale, such fine processes can be best resolved in an SEM. For this purpose, we investigate reactive spreading behavior in-situ, employing an FEI Quanta 250 environmental SEM with an exchangeable heating stage. In environmental mode, the SEM can operate with a chamber pressure between 0.1 and 1.4 mbar. Forming gas (Ar-0.95-H_2-0.05) was chosen as chamber atmosphere for its favorable properties, offering a slight reductive environment for the experiment, yet not endangering the SEM components to corrosion. The standard sample holder was replaced with the heating stage which was water-cooled and could heat up to 1000 °C. A self-made Cu crucible was manufactured for the small heating stage furnace to assure the conduction of electrons from the SEM primary beam through the sample/crucible to ground.

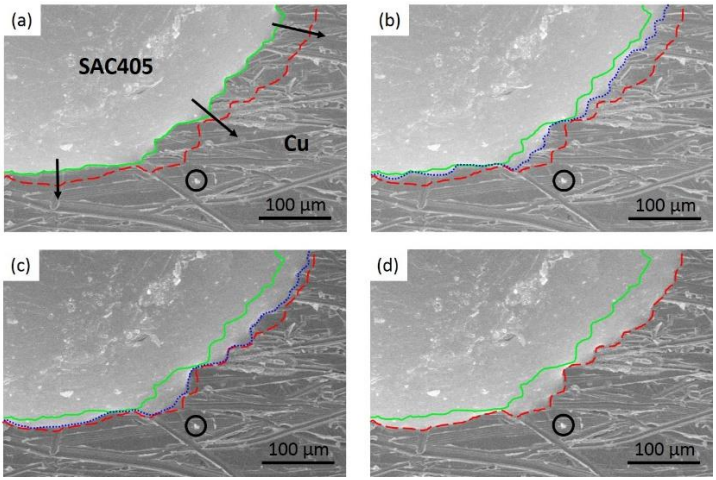

Figure 5.5: In-situ reactive spreading of SAC405 solder on coarsely ground Cu. The temporal movement of the triple line is observed from (a) to (d) and the black solid circle is an orientation marker. The green solid line represents the starting triple line configuration in (a). The red dashed line represents the final configuration in (d). The blue dotted line represents the intermediate configurations. The triple line demonstrates heterogeneous radial stick-slip movement bending around the undulations of the rough surface.

For this investigation, a particle of Sn-Ag(4%)-Cu(0.5%) (SAC405) solder was wetted on a coarsely ground Cu plate. Liquid RMA flux could not be used to reduce surface oxides as it significantly increased the chamber pressure and also emitted gas during annealing which contaminated the chamber. Alternatively, to reduce the impact of oxidation, the SAC405 particle was etched in HCl and the Cu surface was ground directly before the measurement. Figure 5.5 depicts the configuration of the reactive spreading triple line as a function of time from (a) to (d). Although the heterogeneity of the coarsely ground Cu surface in this measurement is accentuated, the observed spreading behavior is proof of the kind of heterogeneous triple line movement generally expected for a reactive wetting system on a rough surface. This is an important conclusion that will serve as a foundation for discussions in 5.6.

5.4 Results – structured substrates

5.4.1 Check of wetting equilibrium

As discussed in section 5.2.4, all CA and spreading distance measurements were completed ex-situ via SEM or optical microscopy after the reflowed solder had reached the steady-state and recrystallized. Unlike the wetting angle formed at the spreading solder front θ_f, the CAs θ_p and θ_s are both restricted by the metallization geometry. A summary of θ_p and θ_s on Cu and Ni metallizations as a function of δ/r_p is provided in Figure 5.6. The independent variable δ/r_p is chosen here because the ratio of the metallization strip and pad sizes is decisive in controlling the strip-pad pressure difference (r.f. Figure 5.1 and eq. (41)).

For both substrate metals, θ_p and θ_s demonstrate increasing trends with decreasing δ/r_p ratio. Furthermore, both θ_p and θ_s are clearly larger on Ni metallizations than on Cu for all geometric ratios. This results from the superior wettability of Sn-based solder on Cu which forms the lower interfacial energy Cu_6Sn_5 intermetallic phase at 350 °C compared to Ni which forms Sn_3Ni_4 with a relatively higher interfacial energy [53]. Consequently, the solder pressure on the metallization strips is significantly higher in the case of Ni, in particular for narrower strips (smaller δ/r_p ratio). For this reason, spreading is significantly hindered on Ni metallizations where $\delta/r_p \leq 0.8$, whereas on Cu metallizations extensive wetting is demonstrated for all measured δ/r_p ratios. Subsequently, only small solder tongues ($s_f \leq 2r_p$) were formed protruding from the pad onto the strip of Ni metallizations where $\delta/r_p = 0.6, 0.8$ (see Figure 5.3 (d)). In this special case, the solder did not spread onto the strip sufficiently far to form a horizontal ridge of constant height, making the measurement of θ_s impractical. Finally we would like to test if our measurements obey the condition of steady state pressure equilibrium defined by eqs. (39-41). Accordingly, additional θ_s data points were calculated from θ_p measurement data via eq. (41) and are presented as red stars in Figure 5.6 (b). The consistency between the measured and calculated data points is remarkable, indicating that our results are reliable and consistent with the equilibrium condition.

We would now like to evaluate the spreading distance vs substrate size, but first, it is helpful to evaluate the relationship between h_s and δ. A direct plot of h_s vs δ is provided in Figure 5.7. (Note that the x-axis does not contain the term r_p and an additional measurement point is included at $\delta \approx 700$ µm.) Within the range of δ

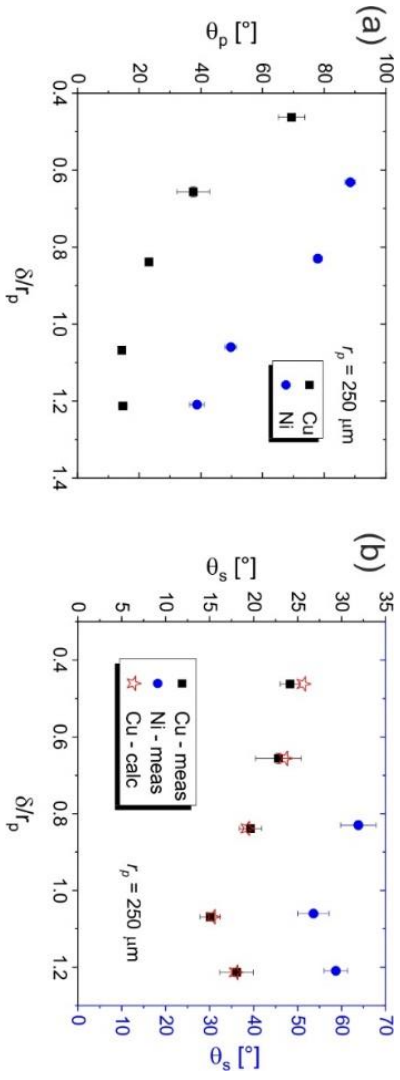

Figure 5.6: Measurements of the (left) pad CAs, θ_p, and (right) strip CAs, θ_s, for eutectic SnPb solder on Cu (black squares) and Ni (blue circles) metallizations after solder reflow, spreading, and recrystallization. Cu data points for θ_s were additionally calculated (red stars) from eq. (41) to compare with the measured data. The CAs on Ni metallizations are significantly larger than on Cu [106].

measured, the trend appears to be linear to a good approximation, yet the y-intercept of the linear regression is non-zero (5.12 µm). This is to be expected since $\theta_s(\delta)$ is not constant (see Figure 5.6 (b)), nonetheless it indicates some form of non-ideal behavior, where there exist multiple solutions to eq. (42) for a seemingly immutable material system. To extend our understanding of the

relationship between spreading distance and metallization geometry, a continuous solution can be calculated based on the measured results. The equilibrium spreading distance s_f can be calculated via eq. (43) below from the metallization dimensions, the initial solder volume V_0, and the $h_s(\delta)$ relationship previously determined (see Figure 5.7).

$$s_f = \frac{V_0 - \frac{\pi}{3} r_p^3 \left(1 - \cos\theta_p\right)^2 \left(2 + \cos\theta_p\right) - \pi r_p^2 \tau}{(A_s + \tau\delta)} \tag{43}$$

Here τ is the effective thickness of Sn consumed by the formation of intermetallic with Cu or Ni and A_s is the cross-sectional area of solder on the strip normal to the direction of spreading. A_s is given by:

$$A_s = R_S^2 \sin^{-1}\left(\frac{\delta}{2R_s}\right) - \delta\frac{(R_s - h_s)}{2} \tag{44}$$

$$R_s = \frac{(\delta/2)^2 + h_s^2}{2h_s} \tag{45}$$

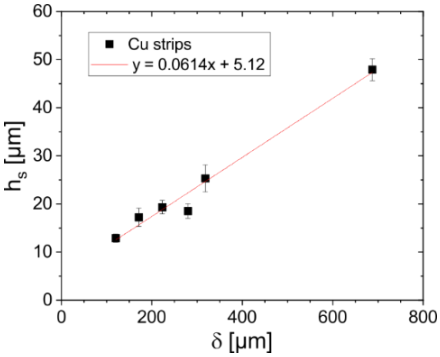

Figure 5.7: The average height of solder along the Cu metallizations strips in the steady-state is plotted against the strip width. The pad radius was $r_p \approx 250$ µm for the measurements on strips with $\delta < 400$ µm, whereas for the additional data point for $\delta \approx 700$ µm the solder volume was scaled up and the pad radius was increased to $r_p \approx 500$ µm, to ensure a sufficient supply of solder consistent with the narrower metallization experiments [106].

Since the measurement conditions were held constant across all material and metallization combinations, τ was assumed constant for all measurements of a

given substrate material. Figure 5.8 presents micrographs of polished and etched cross-sections of the strip post-measurement revealing the underlying intermetallic. In the Ni case, only the Ni_4Sn_3 IMC is formed, as expected thermodynamically. For the Cu case, only the Cu_6Sn_5 phase is visible although Cu_3Sn is also stable. The growth rate of Cu_6Sn_5 is significantly faster than Cu_3Sn, due to Cu diffusion from the substrate to the surface of the scallop-shaped Cu_6Sn_5 grains via molten solder in the channels between the grains [107]. Hence, there may exist a thin layer of Cu_3Sn between the Cu substrate and Cu_6Sn_5 phase, yet because of the relatively low reflow times and temperatures, the Cu_3Sn phase in these samples was too thin to distinguish either with SEM or chemically with EDX. Subsequently, for the sake of calculating τ we assume all visible Cu-Sn intermetallic is Cu_6Sn_5. For both substrate types, τ is calculated as the cross-sectional area of the IMC divided by the length of the cross-section. Finally, after correcting for the lower density of Sn in Cu_6Sn_5, the effective thickness of consumed Sn was found to be $\tau_{cu} = 3.0$ µm for Cu and $\tau_{ni} = 2.2$ µm for Ni metallization strips.

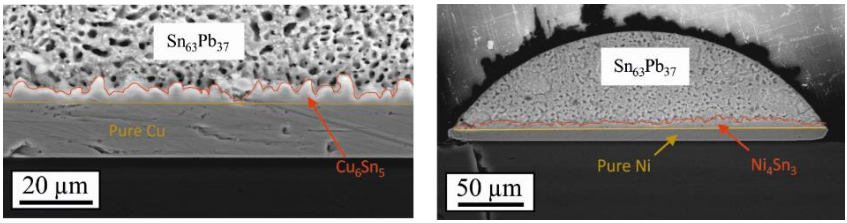

Figure 5.8: SEM micrographs of a polished (a) copper strip and (b) nickel strip cross-section post-measurement. The solder was selectively etched in HCL to reveal the unadulterated underlying IMCs. The scallop-like microstructure of the Cu_6Sn_5 and Ni_4Sn_3 phases is typical for these systems. The porous microstructure of the solder results from the Pb etching faster than Sn [106].

Now that both the $h(\delta)$ function (see Figure 5.7) and τ for both substrates is known, it is possible to predict s_f as a function of metallization geometry via eqs. (43-45). Given that s_f is the equilibrium spreading distance, s_f must be determined under the equilibrium geometric condition defined by eq. (41). Thus, to determine s_f for a given geometric ratio δ/r_p: θ_s is first determined form $h(\delta)$ via eq. (42); θ_p is then determined via eq. (41); finally s_f can be calculated from eqs. (43-45). In this way, s_f can be determined continuously as a function of δ/r_p. The results are plotted in Figure 5.9, showing both the measured and calculated equilibrium

spreading distances on Cu and Ni metallizations as a function of δ/r_p with a constant pad radius $r_p \cong 250$ µm.

Being able to visualize the spreading distance as a function of metallization geometry continuously provides more complete information. For example from the measured data in Figure 5.9, one might interpret the Cu points as demonstrating a simple linear trend and the Ni points as demonstrating no trend. Yet from the calculated curves obtained from geometric considerations it becomes clear that both the Cu and Ni points follow the expected trends. One may nonetheless deepen the analysis and separate the curves into three characteristic spreading regimes (I, II, III) which are controlled by the pad/strip pressure difference. In regime I, $\Delta P_p^{init} < \Delta P_s$ and as a consequence in theory no spreading is expected. The dotted line between regime I and II represents the case where $\Delta P_p^{init} = \Delta P_s$. The dotted line between regime II and III represents the case where $s_f = s_f^{max}$. Spreading is expected in both regimes II and III as $\Delta P_p^{start} > \Delta P_s$, yet they are differentiated

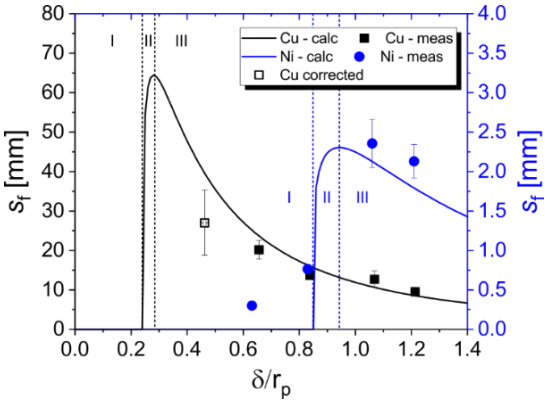

Figure 5.9: Comparison of the directly measured steady-state spreading distances (solid points) vs the spreading distances calculated as a continuous function of δ/r_p (solid lines) from eq. (43) for eutectic SnPb on Cu (black, squares) and Ni (blue, circles) metallizations. Dotted lines separate different wetting regimes (I, II, III) which are characterized by different degrees of spreading as controlled by the pressure difference between pad and strip. The extra data point for Cu (black hollow square) is corrected for the reduced solder volume which was required for the measurement of the narrowest metallizations (to avoid the solder spreading to the end of the metallization strip) [106].

by the dominating phenomena which cause $s_f < s_f^{max}$ in each case. In regime II, δ is narrow and s_f is limited by ΔP_s which is relatively large according to eq. (40) and hinders s_f from reaching s_f^{max}. Conversely in regime III, δ is wider and thus more solder volume is required to cover the same distance along the strip according to eq. (44). The maximum spreading distance can be achieved by compromising these phenomena.

The measured data and calculated curves are in good agreement particularly for Cu, validating the simple model and geometric assumptions made (constant curvature at the pad and strip). Nonetheless, some deviations may be addressed. In the case of Ni, spreading is observed experimentally for $\delta/r_p = 0.6$ and 0.8 although no spreading is predicted by our model. This results directly from the model approximation that h_s forms a constant plateau along the strip. This is clearly not the case for the solder front which curves downwards to the substrate. Consequently, the approximation becomes increasingly inaccurate as the spreading distance reduces (see Figure 5.3 (d)), which would explain both the discrepancy between measured and calculated data for Ni structures within regime I and the generally better accuracy of the model in predicting spreading on the Cu metallizations which exhibited significantly larger spreading distances (ca. 10 fold). As a consequence of the shorter spreading distances and lower accuracy of the Ni system measurements, subsequent quantitative analysis and discussion will focus solely on the Cu system.

5.4.2 The contact angle at the solder front

The wetting angle at the solder front θ_f is the only CA that is measured in a direction where spreading is unrestricted by the edges of the metallization structure. Consequently, any size dependencies observed for θ_f may be considered a direct result of the material properties, making the investigation of θ_f the primary interest of this study. The experimental data for θ_f is plotted in Figure 5.10; a clear size-dependent trend is visible with θ_f increasing with decreasing δ, which demonstrates a remarkable systematic deviation from Young's equation. To provide a comparison at the macroscopic limit, an additional measurement was conducted of ca. 10 mg (ca. 25 times more than the patterned sample measurements) eutectic SnPb solder on a ca. 1 x 1 cm electroplated Cu substrate. This calibration sample was produced similarly to Cu strip samples without the patterning step and the reflow measurement was also conducted as outlined in

section 3.2.2. The average CA was determined ex-situ from polished embedded cross-sections of the samples via optical micrographs. The calibration data point has an average measured equilibrium diameter of 3000 µm and although the spreading solder was not restricted by the metallization geometry in this case, the measurement point was correspondingly given an effective strip width of $\delta = 3000$ µm (see Figure 5.10, note the broken x-axis) which is sufficiently large to minimize microscopic hysteretic effects and closely represents Wenzel's equilibrium (eq. 16).

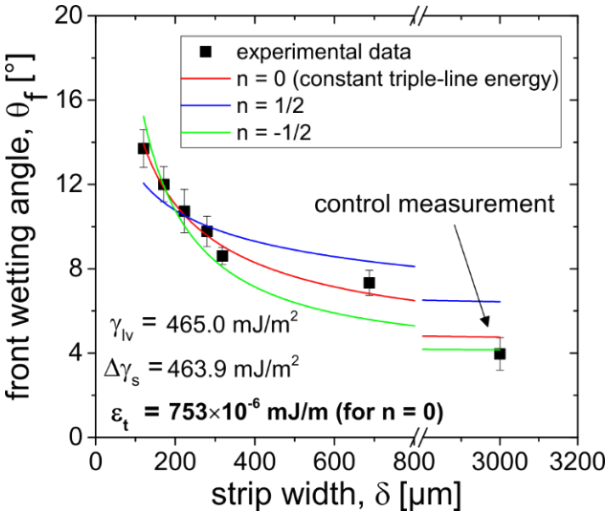

Figure 5.10: Experimentally measured θ_f on Cu metallizations as a function of δ. The solid lines represent fits of data to the model equation (47). Each line is characterized by a different exponent n. $n = 0$ defines a triple-line energy independent of size, whereas $n = 1/2, -1/2$ represent inverse and direct size dependencies of ϵ_t respectively. $\gamma_{lv} = 465.0\ \mathrm{mJ/m^2}$ was predetermined (see section 4.2.1: Surface Tension) and $\Delta\gamma_s = 463.9\ \mathrm{mJ/m^2}$ was predetermined from the calibration measurement assuming ideal behavior. The best model prediction was for a constant triple-line energy of $\epsilon_t = 753\ \mathrm{nJ/m}$ [106].

The trend demonstrated in Figure 5.10 is non-trivial and requires a suitable model to assist in its interpretation. Considering the non-linear relationship observed, there is a strong probability that hysteretic phenomena are responsible, although this cannot be demonstrated experimentally without also measuring the receding

wetting angles. Nonetheless, from the conclusions and observations of past studies, it is understood that hysteretic phenomena occur almost entirely at the spreading triple line. Consequently, to quantify this trend predictively, we extend Young's equation by including an effective triple line energy term ϵ_t with units of J/m.

$$0 = \Delta\gamma_s - \gamma_{lv}\cos\theta_f - \epsilon_t\left(\frac{2}{\delta}\right)^{1+n} \tag{46}$$

$$\cos\theta_f = \overbrace{\cos\theta_0}^{\frac{\Delta\gamma_s}{\gamma_{lv}}} - \frac{\epsilon_t}{\gamma_{lv}}\left(\frac{2}{\delta}\right)^{1+n} \tag{47}$$

Here, $\frac{2}{\delta} = 1/r_f$ represents the inverse theoretical radius of curvature of the solder front triple line, n represents the dependency of ϵ_t on the half strip width $\frac{2}{\delta}$, and θ_0 is the equilibrium CA which for a rough surface will become the Wenzel CA θ_W. Equation (47) can be best understood by splitting the RHS into two terms: the first term represents the ideal or Wenzel equilibrium situation and the second term including the triple-line energy is a correction for any non-ideal size dependency. To apply the predictive model (47) the following data was used: the measured dependent θ_f and independent δ variables; the surface tension $\gamma_{vl} = 465.0\ \mathrm{mJ/m^2}$ as determined from the previous study under the same measurement conditions (see section 4.2.1: Surface Tension); and $\Delta\gamma_s = 463.9\ \mathrm{mJ/m^2}$ as predetermined from the control measurement which was assumed to be sufficiently close to the macroscopic limit (i.e. negligible size/miniaturization effects). Using the numerical least-squares minimization approach to fit eq. (47), the triple-line energy was determined for the three exponents $n = 0, 1/2, -1/2$. The fitted (colored) curves are presented in Figure 5.10. The exponent $n = 0$ clearly yields the best fit, indicating a constant effective triple-line energy, and for which the triple-line energy was quantified to $\epsilon_t = (753 \times 10^{-6} \pm 31)\ \mathrm{mJ/m}$. This result is quite remarkable, since the magnitude of ϵ_t is several orders of magnitude larger than the energy of atomic interactions and broken bonds at the triple-line. A discussion of the possible phenomenological cause of this result follows in 5.6.6 and from a different perspective in 5.7.2.

5.4.3 The lollipop geometry: proportional vs disproportional scaling

Here a brief calculation will be offered investigating the dependence of θ_s on the disproportionally scaled lollipop metallizations under ideal conditions. But first consider the proportional size variation of the metallization, i.e. the geometric ratio δ/r_p defining the lollipop metallization structure is held constant. For an ideal wetting system that is solely governed by the minimization of the surface and interface energies, it is clear that the equilibrium CAs on the pad and strip after spreading would be independent of size and so the spreading distance would be proportional to δ. But in our experiments, we have varied r_p and δ disproportionately. In this case, the equilibrium spreading distance no longer varies proportionally with δ and thus it seems advisable to theoretically investigate whether or not varying δ/r_p (i.e. geometric effects) may influence the ideal equilibrium CAs. To this end, a simple model was considered, with model parameters taken from the metallization experiments: $r_p = 250$ µm, $\gamma_{lv} = 465$ mJ/m^2 and $\Delta\gamma_s = 463.9$ mJ/m^2 (see section 5.4.2). The ratio δ/r_p was varied from 0.5 to 1.6 and the solder volume was taken as $V_{solder} = \frac{3}{4}\frac{3\pi r_p^3}{4}$ as in the experiments. Considering the geometric equilibrium pressure condition (41) and accounting for volume conservation, the equilibrium CAs were determined by iterative energy minimization of the total system energy, which was determined as the sum of the pad and strip surface and interface energies (i.e. ideal conditions).

$$E = A_{sl}\Delta\gamma_s + A_{lv}\gamma_{lv} \tag{48}$$

The solder on the pad was calculated as a spherical cap, and for simplification, the solder along the strip was approximated as a cylinder segment with constant radius along the strip.

$$E = \left(\pi r_p^2 + \delta s_f\right)\Delta\gamma_s + \left(2\pi r_p^2(1-\cos\theta) + 2\theta_s r_s s_f\right)\gamma_{lv} \tag{49}$$

The results are presented in Figure 5.11. As predicted, the spreading distance varies disproportionally with δ. Nonetheless for this ideal case, θ_s remains independent of δ/r_p amounting to $\theta_s = 6.4$ °. Thus, the variation of θ_s measured experimentally is not affected by the variation of δ/r_p and can only result from the triple line equilibrium.

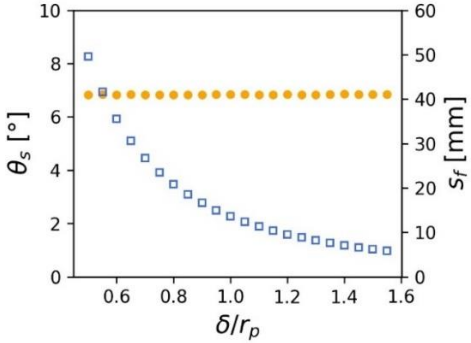

Figure 5.11: Expected ideal equilibrium strip CA, θ_s, (yellow dots) and spreading distance, s_f, (blue hollow squares) as a function of δ/r_p, as modeled by simply energy minimization under the conditions of pressure equilibrium (eq. (41)) and volume conservation. Parameters were taken from experimental results: $r_p = 250$ μm, $\gamma_{lv} = 465$ mJ/m^2 and $\Delta\gamma_s = 463.9$ mJ/m^2, $V_{solder} = 0.75 \cdot V_{sphere}(r = r_p)$.

5.4.4 Comparison with a numerical reflow model

Now, to better understand the θ_s and θ_f experimental results and their relationship and dependence on area and line energies, the surface shape of the equilibrium spreading solder front was numerically modeled using finite element energy minimization. The surface of the solder front was constructed on a strip of width δ from a mesh grid of $n \times m$ points on the transverse x-y plane normal to the spreading direction z (see Figure 5.12 for reference). Each grid point was assigned a spreading distance s_{ij} which was calculated by gradient descent energy minimization. The radius of curvature of the solder surface at $z = 0$ was held constant in space (across the strip) but was made temporally variable, allowing the height of the individual grid points to be calculated trigonometrically from the radius after each iteration. The iterative variation of the spreading distances and the strip radius of curvature cause the areas A_{sv}, A_{lv}, and A_{sl} at the solid-vapor surface, liquid-vapor surface, and solid-liquid interface, as well as the triple-line length l_t to change dynamically. From these area and line variables, the system energy E_{sys} is calculated as

$$E_{sys} = A_{sl}\gamma_{sl} + A_{lg}\gamma_{lg} - A_{sg}\gamma_{sg} + l_t\varepsilon_t + \lambda V \qquad (50)$$

where λ is a Lagrange multiplier playing the role of the pressure and acts as a penalty term assisting in the conservation of solder volume V. Systems with sufficient spreading have been modeled so that the strip height can be assumed constant far from the spreading solder front. This allowed the trigonometric determination of both equilibrium CAs θ_s and θ_f once the system energy had converged to a minimum and the surface had been optimized.

$$\mathrm{d}E_{sys} = \sum_{i=1}^{n} \sum_{j=1}^{m-i} \left\{ \Delta\gamma_s \frac{\partial A_{sl}^{ij}}{\partial s_{ij}} + \gamma_{lg} \frac{\partial A_{lg}^{ij}}{\partial s_{ij}} + \varepsilon_t \frac{\partial l_t^{ij}}{\partial s_{ij}} + \lambda \frac{\partial V}{\partial s_{ij}} \right\} ds_{ij} = 0 \qquad (51)$$

$$\Delta\gamma_s = \gamma_{sl} - \gamma_{sg}$$

Numerically modeled results are presented in Figure 5.13. Subplot (a) demonstrates the relationship between θ_s and θ_f as a function of δ for an ideal system with $\epsilon_t = 0$. Unsurprisingly both CAs are constant and independent of δ where $\theta_f = \theta_Y$ because spreading in the direction of the solder front is unhindered making θ_f solely dependent on the balance of the interface energies. This is contradictory to our experimental results which demonstrate clear dependencies on δ. Subplot (b) similarly compares θ_s and θ_f, but as a function of Young's angle ($\Delta\gamma_s$ is varied and δ is held constant). In this case, θ_s and θ_f are found to vary approximately proportional ($\theta_s / \theta_f = 1.79$). This is an important conclusion, as the relationship between θ_s and θ_f cannot be determined analytically.

To be rigorous, we can test the consistency/correctness of this ideal theoretical ratio by comparing it with the experimental results for θ_f from section 5.4.2 and the theoretical results for θ_s from section 5.4.3, of which θ_Y is crucially the same in all cases (i.e. equivalent surface and interface energies). Since θ_Y is equivalent in all cases, the ideal ratio $\theta_s / \theta_f = 1.79$ should also hold in all cases. Indeed, if we calculate the ratio of $\theta_s = 6.4\,°$ from section 5.4.3 and $\theta_f = 3.9°$ from Figure 5.10 (for the largest experimentally measured droplet, approaching the macroscopic limit where approximately ideal wetting is assumed), the result is $\theta_s / \theta_f = 1.64$, which is remarkably similar and confirms the consistency of our calculations.

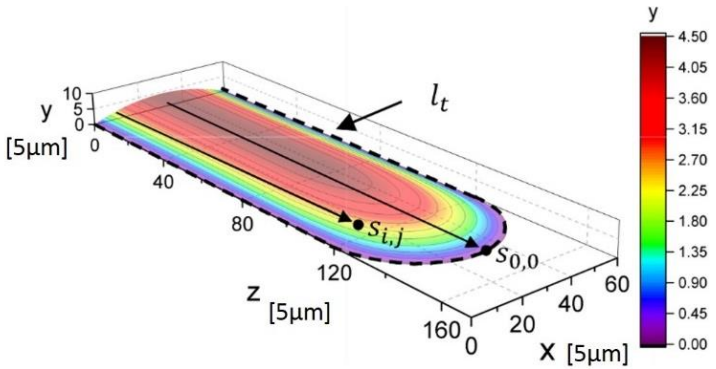

Figure 5.12: Example of a typical surface optimization solution using a 30 x 30 (x-y) mesh grid. The energy parameters used in this example are $\Delta\gamma_s = 300\ \mathrm{mJ/m^2}$, $\gamma_{lv} = 305\ \mathrm{mJ/m^2}$ and the strip width (x-axis) is $\delta = 300\ \mu\mathrm{m}$ [106].

Figure 5.13 (c) presents both numerically modeled data of θ_f and θ_s (points) and continuous curves of θ_f calculated from eq. (47) for wetting systems with varying triple-line energies $\epsilon_t = 0$ (black), $\epsilon_t = 100\ \mathrm{nJ/m}$ (blue), and $\epsilon_t = 400\ \mathrm{nJ/m}$ (red) and with γ_s and $\Delta\gamma_s$ held constant. One may first observe that the calculated and modeled θ_f data are self-consistent, confirming the validity of the modeled data. From the modeled data, both the θ_f and θ_s CAs demonstrate a deviation from ideal behavior, where the CAs not only increase inversely with δ, but also increase with ϵ_t. Furthermore, θ_f and θ_s remain approximately proportional ($\theta_s\ /\theta_f = 1.79$), particularly for large δ. Thus for this wetting model we may conclude that $\theta_f > \theta_Y$ unless $\epsilon_t = 0$, and that $\theta_f \to \theta_Y$ as δ increases regardless of ϵ_t.

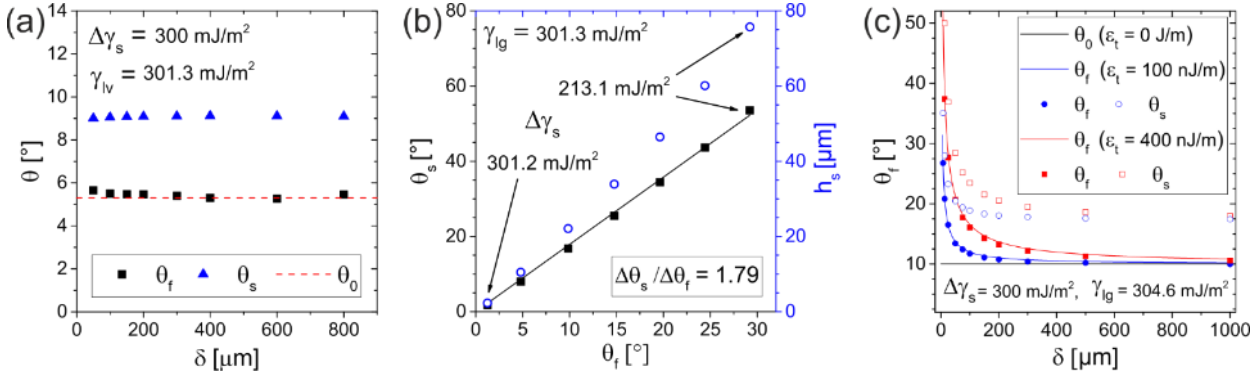

Figure 5.13: Results for θ_f and θ_s obtained by numerical surface optimization modelling of solder fronts spreading on metallization strips of varying width δ [106]. (a) Strip width vs CAs for the ideal wetting case ($\epsilon_t = 0$). The points are modeled and the red dashed line is calculated from Young's equation. (b) Relationship between various geometric variables with $\Delta\gamma_s$ varied from 213.1 to 201.2 mJ/m^2 and δ held constant. (c) Relationship between δ and θ_f for various values of ϵ_t representing an ideal system (black) and two non-ideal systems (red and blue). The lines are calculated from eq. (47) and the points are modeled.

5.5 Results – unstructured substrates

5.5.1 Smooth polished substrates

A list of the various measurements on unstructured substrates can be found in Table 5.2. On polished substrates, three measurements were repeated at both a low temperature (LT) of 242 °C and a high temperature (HT) or 350 °C. The results are presented in Figure 5.14 and individual measurements are indicated by different shapes. At first glance, one can observe clear trends at both temperatures with moderate fluctuations. A closer look at the individual measurements reveals that the fluctuations predominantly result from small deviations between measurement trials; the data points within a single measurement trial on the other hand exhibit impressively little deviation from their main trends. The LT3 measurement (yellow squares) is most representative of this point. Regarding the measurement trends, at both temperatures, the advancing CA is observed to decrease with decreasing solder ball diameter. Furthermore, an unquestionable non-linear dependency on solder diameter is observed, where the CA curve drops off significantly faster at smaller solder volumes. Finally, across all diameters, the HT system demonstrates a shift to lower CAs compared with the LT system. The direct relationship between wetting angle and solder diameter is quite remarkable considering that the exact opposite trend was observed between the front CA and

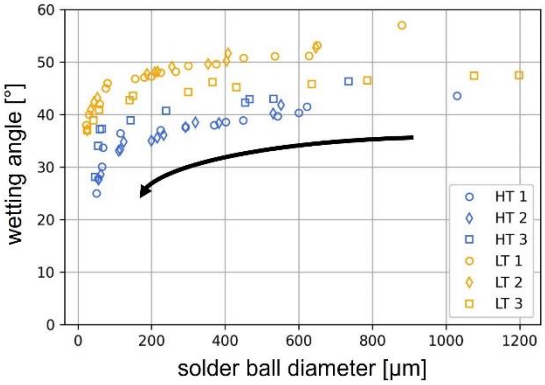

Figure 5.14: High temperature (HT) and low temperature (LT) advancing CA measurements vs solder ball diameter for pure Sn on polished Cu using RMA flux and formic acid / N_2 atmosphere.

the strip width of the patterned electroplated substrates. A detailed comparison of these results is presented in section 5.7.

5.5.2 Rough electroplated substrates

Wetting experiments were also conducted on rough unstructured substrates to compare with those done on unstructured polished substrates. For these investigations, four electroplated Cu substrates were used of varying roughness. Both the surface roughness and the reflow holding temperature were varied to provide a complete comparison with the polished substrate measurements. The surface roughnesses of samples 1-4 are imaged in Figure 5.15. The substrate roughnesses increase from samples 1 to 4. Samples 1 and 2 are the least rough of the four and besides some minor mushroom caps on sample 2 which are scattered with a low density, the predominant roughness of samples 1 and 2 is similar. The predominant surface roughness then increases with sample 3 and again with sample 4 which is the roughest. Here the roughness is ranked qualitatively by observation via electron microscopy and an increase in the predominant roughness

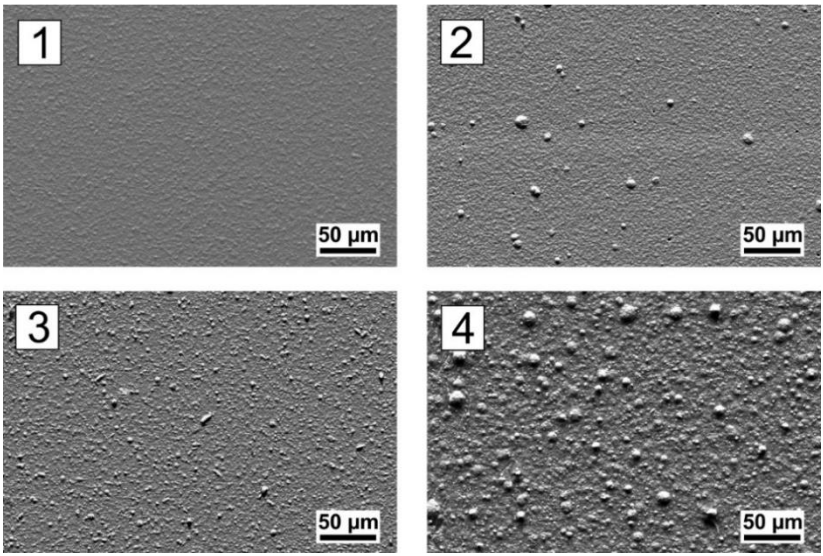

Figure 5.15: Surface roughness of electroplated copper samples 1-4.

between samples is recognized as both an increase in roughness wavelength and amplitude.

The results of the reactive wetting measurements are provided in Figure 5.16. Four measurements are presented in total. Two measurements were done at both HT and LT and the sample numbers correspond to the numbered rough surfaces in Figure 5.15. At first glance, it can be generally stated that, across all samples, more significant statistical fluctuations are observed compared with the CAs measured on smooth polished Cu (Figure 5.14). This may although be expected due to the random nature of the roughness investigated. Nonetheless, variation between the CA trends of each sample can be observed. Firstly considering the rougher samples 3 and 4 (red and gray circles), an inverse relationship between solder diameter and CA is clearly observed. Whereas, the less rough substrates 1 and 2 demonstrate no clear dependence on solder diameter. In fact, at lower solder diameters, the CAs of sample 1 exhibit the opposite trend to that of the rougher samples, showing a slight tendency to decrease directly with solder diameter. In all cases, any dependence of the CA on solder diameter is greatly reduced at larger solder diameters. Furthermore, it is at these larger solder diameters that the

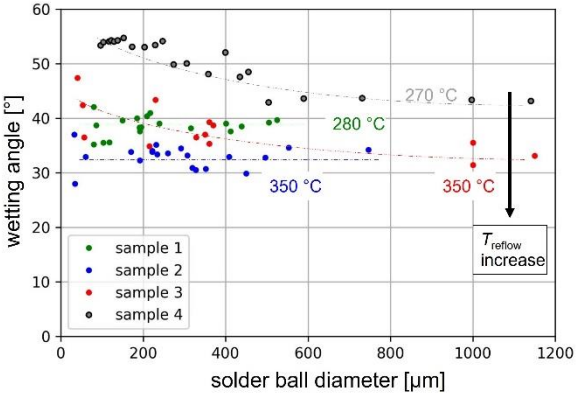

Figure 5.16: Advancing CAs of Sn on rough electroplated Cu substrates using RMA flux and formic acid / N_2 atmosphere. Sample 1 (green): 280 °C holding temperature. Sample 2 (blue): 350 °C holding temperature. Sample 3 (red): 350 °C holding temperature. Sample 4 (grey): 270 °C holding temperature. Sample 4 is represented as a 3 point moving average of the raw data. The colored dashed lines serve only to highlight the main trends.

influence of temperature is systematically visible. As indicated in Figure 5.16, an increase in reflow temperature is visibly associated with a decrease in CA. Moreover, the CAs of samples 2 and 3—which differ in roughness but share the same reflow temperature of 350 °C—deviate noticeably for smaller solder diameters, yet converge towards larger solder diameters. A comparison of the results for smooth and rough substrates including a phenomenological interpretation of their differences will follow in section 5.7.

5.6 Discussion – structured substrates

5.6.1 Substrate roughness vs intermetallic roughness

We have conducted numerous reactive wetting experiments using a variety of Cu substrates. Both structured and non-structured substrates have been prepared with both rough and smooth surface finishes. Before beginning a deeper discussion of the individual results, it is necessary first to outline an important conclusion which to the author's knowledge has not been directly addressed in literature previously. In the field of reactive wetting, it is widely understood that the kinetics of the spreading triple line is controlled by the kinetics of lateral growth of the product phase at the triple line. This in turn is controlled by the slower of: (i) the reaction rate and (ii) the rate of diffusion of the reactive species from the bulk liquid to the triple line. The diffusion-controlled spreading is only relevant for liquid alloys, which may form a reactive element depletion zone at the spreading triple line. In either case, the spreading triple line is assumed to advance on the newly formed product phase. But critically, for $Cu^{(s)}/Sn^{(l)}$-based solder systems, the product phase is predominantly Cu_6Sn_5 which forms a rough scallop microstructure.

This begs the question: assuming the reactive spreading triple line is influenced by surface roughness—is it influenced by the inherent morphology of the substrate, or rather by the scallop-like Cu_6Sn_5 morphology. Of course, this depends on the spreading velocity, since the IMC scallops do not grow instantaneously. Fortunately, an initial comparison of the reactive spreading experiments on rough and smooth substrates sheds light on this question. All experiments on rough electrodeposited substrates resulted in an inverse relationship between CA and solder joint size. The experiments conducted on polished substrates on the other hand demonstrated a direct relationship between CA and solder size. Considering that the Cu_6Sn_5 scallop morphology formed at

the interface is—given sufficient reaction time—to a first approximation independent of initial substrate roughness, we can say, applying proof by elimination, that the inherent surface roughness is the predominant factor causing either a direct (smooth surface case) or indirect (rough surface case) relationship between CAs and solder diameter to exist. This conclusion will be critical in subsequent discussions. The physical interpretation of the observed CA trends will follow.

5.6.2 Trivial and non-trivial size effects

This study, in contrast to various similar studies on size effects in non-reactive wetting systems, investigates reactive wetting systems which are technically relevant as solder joints. The characteristic product phase which forms during reflow of reactive systems has the effect of homogenizing the prepared surface via the formation of intermetallic scallops and purging the surface of imperfections and asperities (see section 2.4). This is of course only the case for imperfections smaller than the inherent roughness of the product phase. For transparency of argumentation, we will now categorize our observations as either trivial or non-trivial size effects:

A) Trivial size effects are unique to the investigated test geometry (or similar) which comprises two geometrically non-equivalent areas (the pad and strip). This effect arises from disproportionate changes in the substrate geometry (i.e. δ/r_p not constant). Such a case is exemplified in Figure 5.9 (also theoretically in Figure 5.11) where trivial size effects are predominant: the varying geometric δ/r_p ratio causes a shift in the equilibrium pad-strip pressure balance, finally resulting in disproportional spreading behavior. Logically, all wetting systems may exhibit trivial size effects if the restricting substrate geometry is varied disproportionately. Nonetheless, the CA at the solder front θ_f is unaffected by such trivial effects. Considering that the maximum pad pressure occurs for a hemispherical solder droplet where $\theta_p = \pi/2$ and given that $\theta_s \approx 1.8\theta_f$ from Figure 5.13 (b), by rearranging and substituting into eq. (41) one may furthermore deduce the condition:

$$r_p \sin(1.8\,\theta_f) < \delta < 2r_p \tag{52}$$

This modification of the earlier geometric condition eq. (41) has the following consequences: (i) δ must be sufficiently large to spread, overcoming the strip pressure (as exemplified in Figure 5.9); (ii) not only the metallization geometry but also the front wetting angle θ_f—which is ideally defined by the balance of surface and interface energies according to Young's equation—controls spreading along the strip. This is exemplified by the different spreading distances observed on geometrically equivalent Cu and Ni substrates (Figure 5.9) due to the larger wetting angle of SnPb on Ni_3Sn_4 compared with Cu_6Sn_5.

B) Non-trivial size effects arise even if the substrate geometry is varied proportionally. They primarily cause variation in the wetting angle θ_f at the spreading solder front, as observed experimentally (see Figure 5.10). Furthermore, non-trivial size effects secondarily influence the strip pressure ΔP_s by controlling θ_s vis the relationship $\theta_s \approx 1.8\ \theta_f$ (see Figure 5.13 (b, c)).

A primary finding of our study, although unexpected, is that the experimentally observed non-trivial size effects are analytically well described if—like surface area has the property of surface energy—the triple line is assigned the property of a line energy (demonstrated in Figure 5.10). A few past studies, while investigating CAH, have also used this concept and calculated triple line energies, although only inert substrates were investigated. A comparison of the TL energies from these past studies, with the TL energy measured for a reactive system in this work follows in section 5.6.4.

5.6.3 Comparison with the model of Huh and Mason

To strengthen our conclusions on size effects and the impact of roughness on CAs, we now employ the first-order perturbation model suggested by Huh and Mason [19] for a liquid droplet on a sinusoidal cross grooved surface (see inset of Figure 5.17). It is not discussed explicitly by the authors, but their model predicts a dependency of the CA on the ratio of the droplet size to roughness wavelength/amplitude, although the physical reason for this prediction will be discussed later. The conditions of the model were previously outlined in section 2.3.2, and the eq. (19) provides the relationship between CA and drop radius. The sinusoidal cross-grooved surface model of Huh and Mason represents perhaps the simplest theoretical 2-dimensional rough surface, making it the logical best

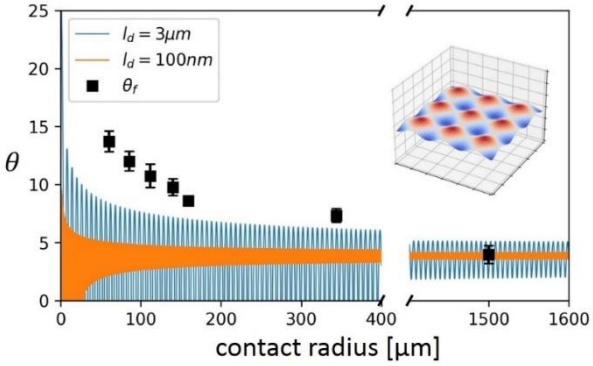

Figure 5.17: Wetting angles calculated with the perturbation model of Huh and Mason using constant parameters $\theta_0 = 3.9\,°$, $\omega = 0.2$, and $l_d = 3$ µm, 100 nm. θ_f (black squares) are the experimental data for eutectic SnPb on structured Cu substrates. The inset in the top right corner is the theoretical surface represented by the model. The modeled CA varies periodically with drop base radius. As the drop base radius decreases, the relative difference between the number of peaks and troughs under the triple line increases, causing the amplitude of the CA fluctuations to increase.

starting point for investigating CAs on surface roughnesses. Solutions to eq. (19) for roughness wavelengths $l_d = 3$ µm and 100 nm are presented in Figure 5.17 in comparison to our θ_f data experimentally measured on the lollipop metallizations. $\theta(r)$ determined from Huh and Mason's model oscillates around θ_0 as a function of contact radius. The deviation of θ from θ_0 is a consequence of the triple line resting on a varying number of roughness peaks and troughs. As the contact radius decreases, this inequality fluctuates and increases which causes $\Delta\theta = |\theta - \theta_0|$ to increase. For certain contact radii, θ is observed to decrease below 0°; this simply represents perfect wetting.

This model does not explicitly calculate hysteresis, since the function solution is independent of the direction of triple line movement. Nonetheless, the envelopes of the fluctuations of $\theta(r)$ may be considered an approximation of hysteresis (as also stated by the authors), whereby the maxima and minima of the contact angle envelopes approximate θ_a and θ_r respectively. In effect, the jumps between adjacent maxima or minima simply represent periodic shifts in the equilibrium configuration and CA as a function of droplet volume (or radius). Yet it can also

be recognized that, in the advancing wetting case, the minima between the maxima could represent triple line configurations which are energetically unfavorable and could act as energy barriers between metastable states, i.e. the jumps between maxima or minima are comparable to jumps between metastable advancing or receding configurations. From this model investigation, we can conclude that (i) the reduction of the size of the defects from 3 µm to 100 nm is accompanied by a significant reduction of the predicted CA hysteresis and (ii) the degree of hysteresis becomes most severe once the drop contact radius approaches the scale of the roughness within 2-3 orders. To test the utility of this model, our experimental data can be compared with the blue curve ($l_d = 3$ µm) which was calculated with parameters approximating the microstructure (as presented in Figure 5.4) of the electroplated Cu surfaces used in our solder track experiments. The resulting trend of the model is indeed similar to our experimental data, although deviating slightly at lower contact radii. This underestimation of the model at lower contact radii might be an indicator of the limitation of using this model to predict CAH. Real systems which demonstrate triple line pining and energy barriers to spreading can presumably be expected to exhibit stronger CAH. Finally, the model offers a useful comparison with experiment, but should only be taken as an approximation, as it represents a simple, ideal periodic interface geometry contrary to the complex interfaces we have measured.

We may conclude that the cross-grooved model of Huh and Mason offers a good estimation of hysteresis for rigid chemically homogeneous wetting systems with smooth regular surface defects, although it is likely to be on the side of underestimation. The predictive power of the model will although deteriorate for surfaces with irregularly shaped, randomly sized, or low-density defects.

5.6.4 Comparison of line energy with literature

The focus will now turn to the comparison of our measured effective triple line energy relative to those reported for various non-reactive wetting systems in literature. Good and Koo, who investigated CAs of droplets (1-10 mm diameter) of various liquids on PMMA and PTFE, generally found a direct correlation between drop size and CA, i.e. sufficiently small droplets demonstrated lower CAs [108]. Consequently, they determined ϵ_t to be negative and even to decrease in magnitude with decreasing drop size. It should although be noted that as exceptions, the receding angles measured for ethylene glycol on Teflon were

observed to remain constant. Furthermore, the advancing and receding angles of decane on Teflon were observed to remain constant in dependence on drop size, as were the receding CAs of ethylene glycol on Teflon. Good and Koo argued that the size dependence was not observed for decane compared with water on the basis that decane is non-polar. Conversely, Drelich who investigated CAs of various solutions on quartz observed the inverse relationship: that CAs increased with decreasing drop size [109]. This was the case both for systems exhibiting CAs larger than and smaller than 90°. Furthermore, there was one additional case where polyethylene substrates were either washed with water or processed with nitric acid to create different surface roughnesses. It was found that CAs of water on polyethylene substrates demonstrated an inversion of the drop size dependency depending on the surface finish. The smoother water-washed system demonstrated CAs which increased with decreasing drop size, whereas the rougher acid-treated system demonstrated CAs which decreased with decreasing drop size. This is the opposite trend to that which we have observed concerning surface roughness. One explanation may be that, in the case of Drelich, both systems exhibited predominantly dewetting CAs ($\theta > 90\,°$), whereas our experiments have solely investigated wetting systems ($\theta < 60\,°$), which may invert the influence of roughness on CA hysteresis due to the way the triple line interacts with the roughness. Although this idea should be investigated in the future.

Clearly, the large combination of possible material systems (elastic/rigid substrate, wetting/dewetting, smooth/rough, homogeneous/heterogeneous, reactive/non-reactive, etc.) complicates finding a general quantifiable description relating CA, drop size, and surface roughness. In other words, this lack of consistency between studies on wetting hysteresis is simply indicative of the strong dependence of wettability not only on bulk material properties but also critically on the substrate surface in the vicinity of the triple line. Unfortunately, physical interpretations of these non-ideal hysteretic wetting systems are largely lacking. Logically, a deeper phenomenological analysis of the investigated wetting systems at the microscopic scale is required to pinpoint the cause of these vastly varying size-dependent CA results. Nonetheless, the effective triple line energy is a useful tool for quantitatively comparing the hysteresis and size effects of different wetting systems. Thus, determining the effective triple line energy in conjunction with microscopic investigations of the surface/interface can provide an important point of comparison which may reveal the predominant phenomena controlling wetting equilibria in various systems.

It may only be reasonable to assign the triple line the inherent property of line energy if this line energy is relatively constant. Hence, we should expect the effective triple line energy to be independent of the size or geometry of the joint. This has although only been demonstrated in a few non-reactive cases until now. Our experiments for the first time demonstrate that hysteresis of the advancing CA of a reactive solder system can be well described by assigning a constant effective energy to the spreading triple line. The line energy term was determined to be $\epsilon_t = 0.752 \times 10^{-6}$ J/m, which falls within the higher end of the values determined by various studies for non-reactive polymeric wetting systems ($\sim 10^{-5}$ to $\sim 10^{-8}$ N) which were mostly determined via receding stick-slip experiments [26,28,97,109]. This larger line energy could be expected since metallic substrates have been shown to demonstrate stronger triple line pinning than soft matter [28], which is ironically a disadvantage in stick-slip experiments, where liquid droplets tend to remain stuck on metallic substrates until only a thin film remains and finally evaporates.

5.6.5 Phenomena at the reactive triple line

For transparency, we can compare our measured triple line energy with an estimation of the excess energy of atoms at the triple line. It may be expected that the interfacial atomic interactions of a reactive system are stronger than typical Van der Waals forces. Nonetheless, by estimating the triple line energy as the excess energy of a 2 atom thick tube of surface atoms, we find ϵ_t in the order of $\sim 10^{-10}$ J/m. This is approximately five orders of magnitude less than the line energy determined experimentally, confirming that the effective triple line energy requires an alternative phenomenological explanation.

It is often conceptualized that an effective triple line energy exists—additional to the excess energy of atoms at the triple line—which results from the pinning of the spreading/receding triple line between metastable orientations by surface roughness/asperities [13,94]. Unfortunately, due to the complexity of real rough surfaces, no reliable analytical description relating roughness to CA exists. Nonetheless, a deeper analysis of the root cause of this triple line pinning force is required to progress this field. Extraordinarily, if we are to rationalize a constant effective triple line energy, the triple line pinning force per length must increase proportionally to the triple line curvature (i.e. inverse to drop radius). Consider a droplet spherical cap with contact radius, *a*, which would expand by a distance d*a*,

if not for the average pinning force f per length at the triple line acting against it. The work required to expand or contract the droplet triple line (assuming constant line energy) can be formalized as:

$$\begin{aligned} \mathrm{d}E &= 2\pi\epsilon_t \mathrm{d}a = 2\pi r f \mathrm{d}a \\ &\Rightarrow \epsilon_t = f \cdot a \end{aligned} \tag{53}$$

We see, to rationalize the constant triple line energy calculated from the θ_f measurements, the pinning force f must scale inversely with the contact radius. Furthermore, if ϵ_t is to account for CA hysteresis, the pinning force f must oppose triple line movement for advancing and receding drops and so the sign of ϵ_t must invert for receding drops. But the reliable measurement of a receding drop (which is comparable with the advancing case) is complicated by the structural deformation of the surface during product phase formation. Consider that for a reactive system, the initial solid surface is transformed into a reactive product phase at the triple line as the liquid advances, whereas when the liquid recedes, the product phase is not only pre-existing but also thicker and of differing roughness and will not evaporate, as is generally the case for inert aqueous or organic liquids at room temperature. This makes it practically impossible to compare advancing and receding reactive wetting measurements under the same substrate conditions.

Nonetheless, for the advancing case, we have observed a clear trend of θ_f increasing with decreasing δ (see Figure 5.10) and a fundamental physical explanation for the measured effective triple line energy must be logically developed. As discussed in section 5.6.1, we know that the inherent surface roughness of the electroplated Cu substrates was the dominant cause of the observed trend. However, experiments have demonstrated that the kinetics of a reactive spreading triple line is controlled by product phase formation [47]. It may subsequently be concluded that the product phase forms ahead of the triple line, but this does not comment on the homogeneity of the fresh product phase. Studies on the morphology of Cu/Sn intermetallics of Tu et al. have demonstrated that intra-grain Cu diffusion channels of approximately 1-2 nm width (similar to grain boundary widths) exist between the Cu_6Sn_5 grains which are the uppermost intermetallic layer contacting the liquid solder during wetting of SnPb on Cu [110,111]. Thus it can be assumed that the advancing solder triple line contacts only a nanometer-thin layer of Cu_6Sn_5 which initially takes on the morphology of the underlying Cu substrate—neglecting the Cu diffusion channels which comprise only a small fraction of the solid-liquid interface, i.e. the triple line does

not encounter chemical surface heterogeneities, leaving the surface micro-roughness as the predominant cause of CA variations.

One study by Wu et al. investigated the reactive wetting of molten AgCuTi on Al_2O_3 and non-reactive wetting of molten eutectic AgCu on Cu and demonstrated variation in the CA and drop base radius in dependence on the surfaces arithmetic roughness ($R_a = \frac{1}{l_r}\int_0^{l_r}|z(x)|\,dx$ for the one-dimensional case). They observed opposite trends for the two systems and explained that the improved wetting of the non-reactive system with roughness was a consequence of both capillary channeling through roughness grooves and the increased surface area as described by Wenzel. Conversely, the decreased wettability with roughness observed by the reactive system was attributed to pinning of the triple line by surface asperities. Indeed their conclusion does fit our observed trend for $\theta_f(\delta)$, i.e. that the front wetting CA increases as the drop radius (half strip width) decreases, approaching the scale of the roughness. Nonetheless, there is insubstantial evidence to support their physical reasoning. Their choice to vary the surface roughness and hold the liquid volume constant has the repercussion that one cannot differentiate between the impact of the variable surface area (Wenzel case: equilibrium interface phenomenon) and the variable pinning behavior (non-equilibrium triple line phenomenon). Consequently, it is difficult to draw conclusions on the physical cause of their observed trends. Keeping the roughness constant, as we have done in our primary experiment, has the advantage that the substrate surface area remains unchanged and the concept of Wenzel becomes irrelevant. The following section will discuss the relationship between roughness and triple line radius in greater detail.

5.6.6 Roughness vs triple line contact radius

We have previously found the experimentally observed trend of $\theta_f(\delta)$ to be well described by assigning the solder triple line the property of a constant effective line energy ϵ_t. This constant pinning energy per line length would seem to indicate that the pinning force $f = \epsilon_t/a$ per line length increases inversely with drop radius, opposing the advancing triple line due to surface roughness/asperities. The variability of the triple line pinning force with drop curvature is counterintuitive since surface asperities are the cause of the pinning and yet the substrate surface morphology is independent of drop curvature. Yet after deeper considerations, a possible cause of this counterintuitive pinning force elucidates.

First, consider the possible causes of a pinning force which is inversely proportional to drop size even with all other material properties held constant. We may postulate that the production of the intermetallic phase during reactive spreading somehow causes this size dependency. Indeed from our experiments on unstructured substrates, the product phase does seem to contribute to wetting equilibrium size dependencies, but this phenomenon is not dominant in this case as will be discussed later in section 5.7.3 concerning the reactive wetting experiments on unstructured substrates. Other possible causes of a drop size-dependent pinning force must stem from variation in the droplet dimensions. Of course for an ideal system, the contact angle which defines the driving force for spreading ($F = \sigma_{sv} - \sigma_{sl} - \sigma_{lv}\cos\theta$) is independent of drop size. But there are two geometrical properties of a droplet that may influence the pinning force experienced by the triple line (although the properties are dependent): (i) the triple line length and (ii) the droplet contact (base) radius.

Consider first, possible consequences of varying the TL length. Taking a statistical perspective, a smaller droplet will encounter fewer surface defects. Now for a random spatial distribution of defects and variation in pinning force between different defects, it is to be expected that smaller droplets demonstrate less reproducible advancing CAs since the TL length is comparable to the average roughness wavelength. Such statistical fluctuations are expected to reduce for larger droplets (this is indeed observed when comparing wetting on substrates of varying roughness, see Figure 5.21). Nonetheless, provided sufficient repeat CA measurements are done, no size dependency should result. But how does the droplet contact radius impact the TL pinning force? The answer to this question is not obvious, but a possible physical answer will be outlined now. Take a single defect example, where the defect is situated directly outside the TL perimeter (see Figure 5.18 for depiction). The driving force for triple line spreading is defined as $F = \sigma_{sv} - \sigma_{sl} - \sigma_{lv}\cos\theta$. This driving force must be larger than the triple line pinning force, f, in order to continue spreading. Now we compare two almost identical situations, where the triple lines of two different droplets are separated by a short distance from identical defects. Only the contact radius of these droplets differs; one is large, $a \gg \lambda$, whereas the other is relatively small, $a \geq \lambda$, where λ is the lateral defect size.

Now consider that the larger droplet is approaching θ_a, i.e. the spreading driving force of the larger droplet is barely enough to overcome the pinning force at the defect site. As a small portion of the TL spreads through the center of the defect (black dot in Figure 5.18), the neighboring TL segments on either side of the defect will move with it, relaxing into a new stable low energy configuration. Now if the TL of the smaller droplet (in the vicinity of the defect) were to spread to the exact same configuration, it would need to cross a larger distance on average than the larger droplet (additional area to be covered is marked by diagonal black lines in Figure 5.18). Furthermore, the smaller droplet TL would need to contort more severely. This could result in the TL of the smaller droplet experiencing a stronger pinning (or retention) force than the larger droplet. Of course, the theoretical situation becomes more complex for a dense surface of defects, but this could potentially lead to a more pronounced result. It would be interesting to test this

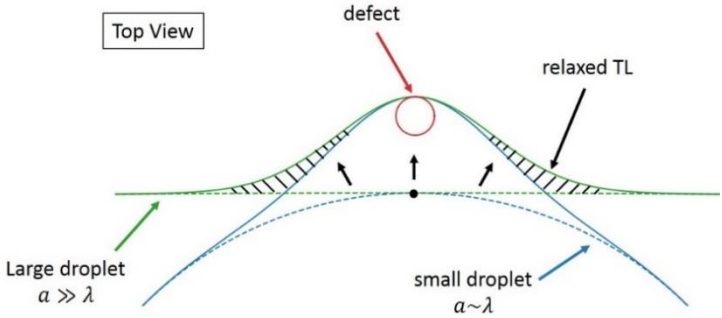

Figure 5.18: Simplified top view depiction of two droplets of different contact radii in the vicinity of a single finite defect. The droplets are completely equivalent besides their size. Both droplets are currently advancing with the same CA, their θ_0 is also identical, and they are initially separated from the defect by the same distance. The contact radius of the small droplet (blue) is comparable in size to the width of the defect. The contact radius of the large droplet (green) is much larger than the defect size (and the defect is practically flat relative to the droplet size). The dashed lines represent the initial droplet TL configurations and the solid lines represent the final states after jumping across the defect to the next stable configurations. Although distance between the defect and the closest points of the droplet TLs are equivalent, in the vicinity of the defect, the average TL position of the larger droplet is closer.

hypothesis for example by finite element modelling of the single defect example or of the capillary energy of an advancing droplet on a surface of heterogeneous surface energy.

5.6.7 Vibrational energy

Before continuing to the discussion comparing substrates of differing roughness, one more topic must be addressed which might influence the inverse CA vs droplet size relationship. Namely, that vibrational energy sources may assist a TL to move and jump over an energy barrier that it could otherwise not cross with capillary energy alone. It is possible, for example, that environmental vibrations like those from motorized laboratory equipment could cause transfer energy into a pinned droplet causing it to depin and move towards capillary equilibrium. Experimental studies have already demonstrated that vibration energy can induce TL movement [41], and in some cases is claimed to promote a droplet to adopt the lowest energy state [112]. But these studies have not investigated lower energy ambient vibrations and are unlikely to be of high relevance in this work. Furthermore, it is not clear if the influence of vibrational energy could also induce a size dependence in hysteretic wetting angles. This would be an interesting dependency to investigate in the future.

5.7 Discussion - unstructured substrates

The investigations on unstructured substrates were principally aimed at answering two open questions: (i) How is the relationship between wetting angle and solder volume influenced by variation in substrate surface roughness and (ii) how is the relationship between wetting angle and solder volume influenced by temperature variation. First, we will make a slight adaption to the stick-slip approach for determining pinning energy barriers (as outlined by Shanahan [27]) so that it is suitable for evaluating advancing systems. After a quantitative evaluation of the results, a discussion of the open questions will follow.

5.7.1 Excess capillary energy

Now we will discuss an approach for evaluating the observed experimental TL pinning which is adapted from the stick-slip approach. We will call this approach, the “excess capillary energy approach”. Although the stick-slip phenomenon can

theoretically occur during both advancing and receding wetting, due to the stronger pinning nature of metallic wetting systems [28] it is more likely to observe the gradual, continuous movement of the triple line than clear, quantifiable stick-slip movements. This creates a problem where θ_0 cannot be determined from a single measurement for metallic systems. Regardless, the accurate determination of θ_0 from stick-slip experiments is altogether questionable. As is represented in Figure 5.19, the final TL configuration of a droplet after a slip movement is almost certainly not the equilibrium configuration, but some intermediate metastable configuration. Alternatively, Shanahan and Bormashenko have separately observed that at some point during evaporation of a droplet, a critical contact radius is reached after which the dynamics of the receding droplet changes [27,28]. Typically, the contact radius decreases slowly or remains steady. This final

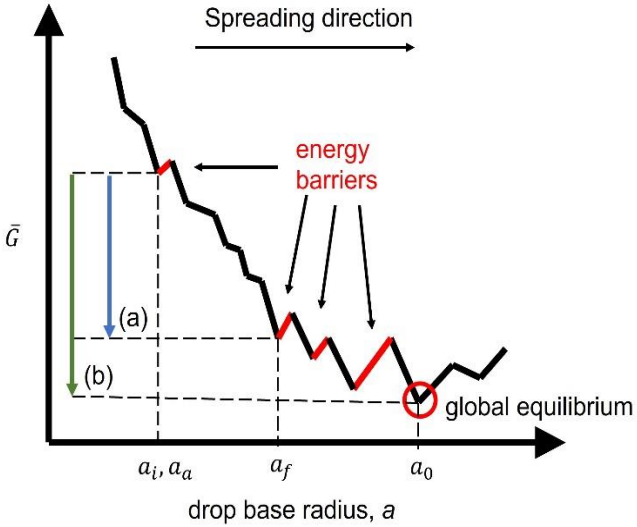

Figure 5.19: Depiction of metastable contact radius orientations of an advancing drop. From lower to higher drop radii the Gibbs energy is reduced. The black lines represent changes in position which will occur spontaneously (negative energy gradient), whereas the red lines represent the immediate energy barriers hindering jumps between metastable triple line positions. (a) The energy change used to calculate the line energy from stick-slip experiments (from initial a_i to final a_f contact radius). (b) The actual energy difference between the pinned and equilibrium drop configurations.

pinning configuration they explain is a consequence of the droplet possessing insufficient excess capillary energy per line length ($\tilde{G}$ defined in eq. (21)) to overcome the pinning barrier. But as is visible in their results, the slow receding of the TL after the final pinning is not as insignificant as one would hope (c.f. Figure 2, [28]), which brings to question the accuracy of the approach.

Fortunately the problem of the stick-slip approach of not being able to determine θ_0 can be circumnavigated in the current work. Although we cannot estimate θ_0 from our individual measurements since no stick-slip motion is occurring, we do have CA large datasets with variations in solder ball volume for each material system. Furthermore, let us define the pinning energy barrier as equal to the excess capillary energy per line length for an advancing droplet when the TL pins:

$$\delta\tilde{G} = \frac{G_a - G_0}{2\pi a} = U \qquad \left(G = \gamma_{lv}\pi a^2\left(\frac{2}{1+\cos\theta} - \cos\theta_0\right)\right) \tag{54}$$

Here G_a and G_0 are the absolute capillary energies of a droplet in the advancing and equilibrium states. Since θ_a is easily measured for different controlled droplet volumes, it becomes possible to determine both θ_0 and U from eq. (54) as fitting parameters provided a sufficient $\theta_a(a)$ dataset.

To solve eq. (54), we employ a simple numerical minimization approach, whereby U is varied until the equation is satisfied. Here we must take into account the dependence of a_a on θ_a under the condition of constant volume, where the volume, V, of a droplet on a surface is given by the volume of a spherical cap.

$$V = \frac{\pi}{3}a^3\left(\frac{(2+\cos\theta)(1-\cos\theta)^2}{\sin^3\theta}\right) \tag{55}$$

Consider the visual depiction of the minimization calculation which is provided in Figure 5.20. For each droplet volume, a $\delta\tilde{G}$ curve (colored curves) is calculated which intersects with θ_0 at $\delta\tilde{G} = 0$ (lower intersection of black dashed lines). Now as already mentioned, TL pinning is defined by the condition, $\delta\tilde{G} = U$. Interestingly, comparing the intersections of $\delta\tilde{G}(\theta)$ for each drop volume with the dash line representing a pinning barrier energy U, a clear droplet size dependence is visible. As the droplet volume decreases, the advancing CA in the pinned state increases. This is a critical observation, as it offers a more intuitive interpretation of the hysteretic size dependency observed in the non-structures substrate reactive

wetting experiments (see Figure 5.21). The implication is simple: as the size of a droplet decreases, for an equivalent CA, θ, the available excess Gibbs energy per line length decreases, causing smaller droplets to relax in metastable advancing configurations with larger CAs. This is exactly what we have observed.

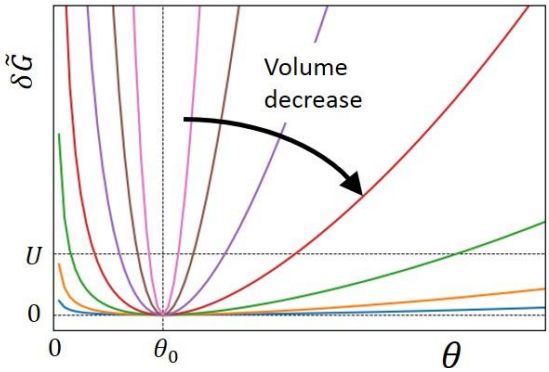

Figure 5.20: Excess Gibbs energy per TL length, $\delta\tilde{G}$, is calculated according to eq. (21) as a function of contact angle, θ, for droplets of varying volumes. The droplet excess energies are represented by colored curves. All trends converge at θ_0 where $\delta\tilde{G} = 0$. For any given CA where $\theta \neq \theta_0$, larger droplets exhibit larger excess capillary energies. This has the consequence that for a given pinning barrier energy U, smaller droplets are expected to pin ($\delta\tilde{G} = U$) at higher CAs (see curve intersections).

5.7.2 Wetting angle vs solder size: rough substrates

Quantitative fits of the wetting angle data for all rough unstructured samples in dependence of solder ball diameter were done using the excess capillary energy approach outlined in section 5.7.1. The fitted parameters are provided in Table 3. The curve fits are presented in Figure 5.21, which offer a comparison of all wetting angle measurements. The figure does not present the raw data but rather moving averages of each raw dataset, except for the structured substrate measurements (black circles) for which each data point already comprises an average of several repeated measurements. The moving averages are useful given the large datasets and have the advantage of smoothing some of the statistical fluctuations making a comparison of the underlying trends with the fitted curves easier.

Table 3: Parameters fitted using the excess capillary energy approach for all rough Cu samples investigated. Experimental parameters also provided. All substrates were Cu.

	θ_0 [°]	U [mJ/m]	Temperature [°C]	Solder	Substrate roughness
Sample 1	38	$300 \cdot 10^{-9}$	280	Sn	minor
Sample 2	32	$300 \cdot 10^{-8}$	350	Sn	minor
Sample 3	32	$400 \cdot 10^{-6}$	350	Sn	major
Sample 4	38.5	$200 \cdot 10^{-5}$	270	Sn	major
HT Sample	No fit		350	Sn	polished Cu
LT Sample	No fit		242	Sn	polished Cu
Structured	3	$753 \cdot 10^{-6}$	350	$Sn_{60}Pb_{40}$	major

First, if we examine the variation in θ_0 between samples 1 to 4 and find θ_0 is smaller (32°) for the higher temperature samples 2 and 3 (see temperatures in Table 3). This fits our expectations from previous observations (see Figure 4.3). Comparing first the impact of roughness for each system, clear observations can be made about the varying dependencies of CAs on solder size. The smooth polished samples demonstrate a direct relationship between CA and solder diameter, whereas the roughhoused electroplated samples 3 and 4 as well as the electroplated metallization tracks conversely demonstrate an inverse relationship. Remarkably, the CAs measured on the intermediate roughnesses of samples 1 and 2 appear to be independent of solder diameter, remaining approximately constant across all solder sizes. There seems to be an overlap of two counteractive size effects which effectively cancel out for the moderately rough samples (yellow and red triangles in Figure 5.21).

Nonetheless, the trends of the varyingly rough samples corroborate the argument that the degree of surface roughness influences the pinning energy of the substrate. The determined TL pinning energies (see Table 3) demonstrate a clear increasing trend with increasing surface roughness (surface roughness increase from samples 1 to 4, see Figure 5.15). Furthermore, the fitted parameters for the structured substrate experiments (see section 5.4) are in great agreement with the parameters

fitted by the modified Young's equation (47) in section 5.4.2, where U and ϵ_t were fitted as $753 \cdot 10^{-6}$ mJ/m and θ_0 varied only by 1° between fits.

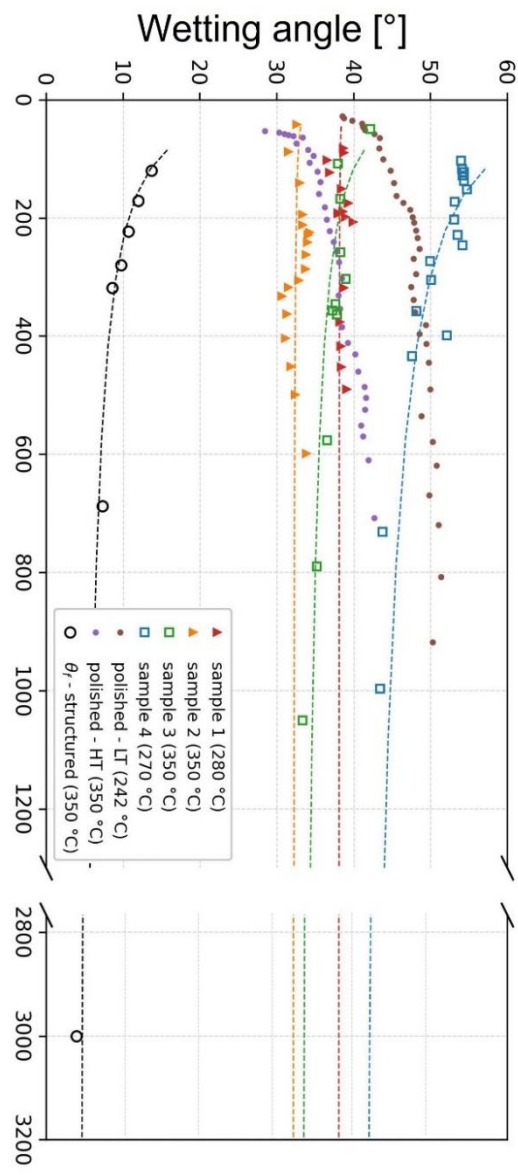

Figure 5.21: Wetting angle vs solder ball diameter results compared for all structured and unstructured samples of varying roughness. Samples 1-4 are represented by a 3 point moving average of the raw data. The HT and LT polished substrate datasets are represented by 5 point moving averages. The individual data points of the structured samples (black circles) are already mean values of several repetitions. Note that the CAs for the structured metallization data are significantly lower than the unstructured datasets because eutectic SnPb solder was used rather than pure Sn. The dashed lines are fitted using the excess capillary energy approach outlined in section 5.7.1. The pinning energy barrier is found to increase for rougher substrates.

Taking solely into consideration the effects of surface roughness on wetting equilibria, we might naively expect that CAs become independent of solder size as the surface approaches atomic smoothness, but this is not what is observed. Rather, CAs independent of roughness are already observed for mildly rough surfaces (samples 1, 2) and an inversion of the relationship is observed for smooth polished surfaces (brown and purple circles, Figure 5.21). This begs the question: what causes the transition from an indirect to a direct relationship between CA and solder diameter. A discussion of the inverse relationship between CA and Sn ball diameter follows in the next section.

5.7.3 Wetting angle vs solder size: smooth substrates

To answer this question, let us consider the timeline of a reactive wetting experiment on an atomically smooth substrate and what is happening physically at the microscopic scale. First, recall that a reflow time of 1 min was used for all unstructured substrate experiments. Upon live visual inspection, spreading of the largest solder balls was observed to stop within one minute, and so by extension, it could be assumed that solder balls of all sizes should equilibrate within one minute. With this clarified, let us now begin at the moment when the Sn ball melts and end at the moment the Sn has recrystallized. First, the solder forms a spherical cap with a CA much larger than θ_0. Now, considering the contact resistance between the substrate and Sn balls and the rate of limited heat conduction into the Sn balls, it is likely that the smaller volume Sn balls melted slightly before the larger Sn balls. Furthermore, it is also probable that the smaller balls, which spread a shorter radial distance after melting, reached a stable triple line configuration faster than the larger balls. Within a matter of seconds t_{pin} after a liquid Sn cap is formed, the cap spreads radially and the triple line is pinned in a metastable configuration with a radius smaller than the equilibrium radius and a CA equal to the θ_a, the maximum angle of a hysteretic system. At this point, the drop remains in the liquid state with the triple line pinned in position. After the 1 minute holding time, the droplet would gradually cool until recrystallization. The critical period is directly after the initial triple line pinning and before droplet recrystallization. During this time two crucial phenomena occur: (i) The formation of the IMC product phase at the interface continues regardless of the pinning TL, and (ii) a halo ring of Sn and IMC forms around the perimeter of the colder cap (see example in Figure 5.22 (a)).

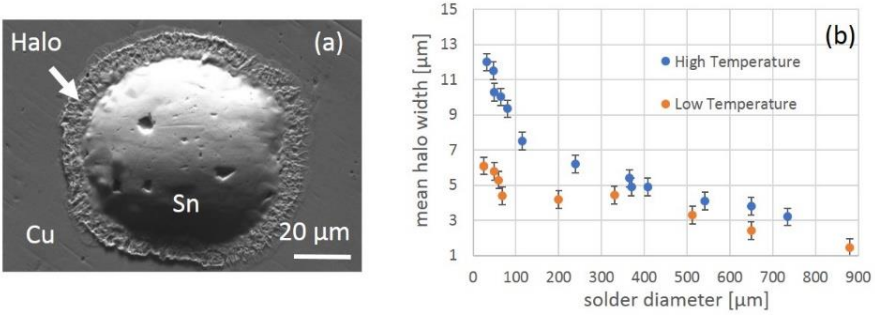

Figure 5.22: (a) SEM micrograph of a 30 µm diameter Sn ball which was melted on a Cu substrate and demonstrates the typical halo ring around the perimeter of the Sn cap. The reflow holding temperature and time was 350 °C for 1 min. (b) The mean width of the observed halo rings is plotted at a function of initial solder ball diameter.

Similar halo regions have been previously reported for lead-free Sn-based solders [113]. EDX measurements logically confirm the halo region to contain both Sn and Cu and it can be assumed that this region is simply an extension of the product phase formed at the liquid-solid interface to the solid-vapor interface. A comparison of the mean width of the halo regions for the HT and LT samples (see Figure 5.22 (b)) reveals that the width of the halos increases with temperature. This supports the hypothesis that the probable cause of the halo is surface or vapor phase diffusion of Sn from the bulk droplet across the Cu substrate.

It could be conceivable that the consumption of tin from these two phenomena has caused the Sn cap volume to shrink while the triple line remains pinned, consequently reducing the CA below θ_a. This would also explain the size effect since the impact of phenomena at the droplet perimeter increases relative to interface and volume phenomena as the drop volume decreases (scaling with r and r^2 and r^3 respectively). We can test this hypothesis by first calculating the volume loss required for such a decrease in CA and then checking if the result can realistically be explained by the loss of Sn to the newly formed IMC phase and halo region. Let us consider the LT smooth substrate system and take $\theta_a = 50\,°$ from the observed plateau at larger solder diameters (see Figure 5.21, brown circles) where the Sn-ball volumes are large enough to neglect the impact of line and area phenomena (like Sn consumption). We take this CA as the expected "ideal" advancing angle on a smooth substrate, i.e. based on our current theory, we would expect to observe $\theta_a = 50\,°$ for all solder ball volumes if there was

negligible Sn consumption. Now let us calculate the difference in Sn volume between (a) a droplet with an initial diameter of 50 µm which spreads as a spherical cap radially and pins at an angle of $\theta_a = 50\,°$ and (b) the same pinned cap with a reduced angle of $\theta = 42\,°$ as was measured experimentally (see Figure 5.21, brown circles). The initial volume of a sphere with $r_{sphere} = 25$ µm is $V_{init} = 65450$ µm^3. For a spherical cap, eq. (56) relates the cap radius r to the volume and CA.

$$V = \frac{\pi}{3} r^3 (2 + \cos\theta)\,(1 - \cos\theta)^2 \qquad (56)$$

Rearranging eq. (56), we find that $r = 57.0$ µm for a cap with $\theta_a = 50\,°$ and $V_{init} = 65450$ µm^3. By simple trigonometry, the spherical cap contact radius is found to be $a = 43.7$ µm. Now assuming that the CA reduces to $\theta = 42\,°$ due to Sn consumption, but the contact radius remains unchanged, the final drop volume is determined to be $V_{final} = 52000$ µm^3. This represents a significant loss of 20 % of the initial cap volume. To test how realistic this is, we must first determine the volume loss by the product phase reaction at the interface.

The effective thickness τ is determined from SEM micrographs as the cross-sectional area of the IMC divided by the length measured. From cross-section analysis, the Cu_6Sn_5 effective (average) thickness was determined as $\tau = 6.1$ µm and $\tau = 6.9$ µm for solder balls of diameter 700 µm and 190 µm respectively. Furthermore, the mean Cu_6Sn_5 grain diameter was determined as 4.7 µm and 5.5 µm for solder balls of diameter 700 µm and 190 µm respectively. The observed increase in IMC thickness with decreasing solder volume has been discussed previously [114]. Essentially, due to the larger area/volume ratio of smaller droplets, the increase in Cu composition in the liquid by the dissolution of Cu atoms at the interface is more rapid. Consequently, the rate of Cu_6Sn_5 growth, which is dependent on the composition of Cu in the liquid solder, increases. Taking $\tau = 6.9$ µm as our average IMC thickness within the TL perimeter (although this may be a slight underestimation for a 50 µm diameter solder ball) and approximating the impact of Cu_3Sn to be negligible, the corresponding volume change is given as $V_{final} = V_{init} - \Delta V$ where $V_{init} = 65450$ µm^3 and ΔV is the volume lost from the solder droplet during reactive spreading. It is crucial to define ΔV carefully. The volume loss can come from either the consumption of Sn at the interface, or from diffusion into the halo region. The droplet volume loss at the solid-liquid interface is calculated as the difference between the volume of the

original pure metals (Sn and Cu) and the formed IMC (Cu_6Sn_5) based on the density change. Conversely, the Sn volume consumed in the halo region is completely lost to the droplet (since it exists outside of the droplet perimeter). Let us approximate that the IMC halo thickness is half that of the IMC under the droplet (this is fair since the halo is not directly connected to the bulk Sn and may also have started growing later than the IMC under the droplet). Furthermore, for a solder ball at LT with $\emptyset = 50$ µm, a halo width of ca. 6 µm is expected (see Figure 5.22 (b)). Then we may approximate ΔV as follows:

$$\Delta V = \Delta V^{(i)} + \Delta V^{(h)} = V_{Cu_6Sn_5}^{(i)} - \left(V_{Sn}^{(i)} + V_{Sn}^{(i)}\right) - V_{Sn}^{(h)} \qquad (57)$$

Where (i) and (h) represent the interface and halo, and the sign of the volume terms represents if they are causing the droplet to lose or gain volume. The volume terms in turn are calculated as:

$$V_{\mathrm{j}} = \frac{m_{\mathrm{j}}}{\rho_{\mathrm{j}}} = \frac{\nu_j\left(V_{\mathrm{cu_6sn_5}}\rho_{\mathrm{cu_6sn_5}}\right)}{\rho_{\mathrm{j}}}, \qquad \nu_j = \frac{x_{\mathrm{j}}a_{\mathrm{j}}}{6a_{\mathrm{cu}} + 5a_{\mathrm{sn}}} \qquad (58)$$

Where m_{j}, ρ_{j}, a_{j}, and ν_{j} are the mass, density, and molar mass, and mass fraction of element j respectively and $x_{\mathrm{j}} = 5\ (\mathrm{sn}), \mathrm{or}\ 6\ (\mathrm{cu})$, represents the intermetallic stoichiometry. The result comes to $\Delta V = 6558\ \mu m^3$ which is ca. 10 % droplet volume loss and yields an expected final volume $V_f = 58892\ \mu m^3$, which is significant, yet still far from the necessary 20 % volume loss required to attribute the CA decrease solely to Sn consumption. So although the decrease in CA with

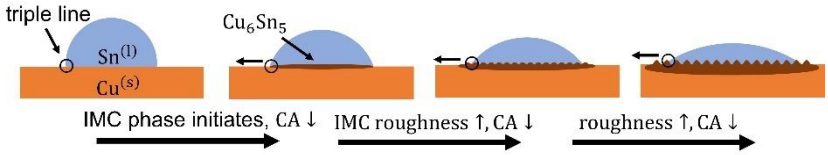

Figure 5.23: Detailed development of the reactive wetting of Sn on a smooth Cu substrate. From left to right: (1) the Sn melts; (2) a thin approximately smooth layer of Cu_6Sn_5 forms at the interface in contact with the Sn.; (3) the Cu_6Sn_5 intermetallic begins forming rough scallop grains and steadily grows ahead of the triple line forming a halo ring; (4) the intermetallic grows thicker at the interface and continues to form ahead of the triple line. The roughening of the substrate results in a reduction of the equilibrium CA according to Wenzel's principle.

droplet size on smooth Cu substrates may be partially explained by the loss of Sn during the product phase reaction, an additional explanation is still required. There is, in fact, one dynamic effect of reactive wetting on smooth substrates which has not been discussed; namely, as the droplet spreads radially, the intermetallic around the triple line roughens. This (micrometer thick) roughening occurs over a longer period than that required for forming an initial thin intermetallic film.

Thus we have two effects that are influencing the surface/interface energies. These effects are depicted in Figure 5.23 for the system of liquid Sn on a smooth Cu substrate. First, the Sn melts and immediately spreads to an equilibrium configuration on pure Cu. Then, within $t < 1$s a nanoscopic approximately smooth layer of Cu_6Sn_5 forms at the interface and the drop triple line begins to advance towards the new equilibrium configuration according to Young's equation, but with the pure Cu surface replaced by the product phase. Within a matter of seconds, the Sn droplets reach equilibrium on the relatively smooth and thin Cu_6Sn_5 phase. At this point, the Cu_6Sn_5 phase continuously roughens at the interface and ahead of the triple line. This causes the interface energy to increase according to Wenzel's model and the triple line consequently edges forward, approaching the dynamically shifting advancing equilibrium configuration. As the advancing equilibrium shifts with surface roughening, θ_a continuously decreases. This process of surface roughening and triple line spreading occurs continuously and simultaneously until the driving force for spreading is insufficient to overcome the hysteretic pinning of the rough Cu_6Sn_5 grains. Therefore, this is a dynamic process difficult to observe for microscopic systems in-situ, particularly when using liquid RMA flux to hinder oxide formation. Now, if we make the naive assumption that for an initially smooth surface, the spreading rate *during the IMC roughening stage* is independent of solder volume, then we may expect that all solder droplets spread the same radial distance over a short time. This would have the geometrical consequence that for variously sized droplets with equal starting CA (before the roughening stage), the smaller radius droplets would undergo a larger CA reduction. Furthermore, due to Cu dissolution, smaller Sn droplets will saturate with Cu faster and so the IMC growth rate of smaller Sn droplets is expected to be higher than larger droplets, which strengthens the expectation of small droplets exhibiting smaller CAs due to dynamic shifting of the equilibrium TL configuration (see Figure 5.21, polished samples). Moreover, the smaller Cu_6Sn_5 grains observed near the droplet perimeter in Figure 5.24 (a) have presumably had less time to grow than grains at the droplet center, supporting the argument that the triple line continues spreading during surface roughening.

Finally, Figure 5.24 (b) provides an example of a 20 µm diameter Sn droplet reacted on Cu at 350 °C for 1 min. Due to the small droplet volume, the droplet has been almost entirely consumed by the interfacial reaction and demonstrates a very low CA. Presumably, given sufficient time and a sufficiently low solder ball volume, the CA will inevitably recede, demonstrating a final CA below θ_0 and approaching θ_r. Thus it is likely the combination of these phenomena which result in a CA reduction for smaller Sn ball on polished Cu. Additionally, since this effect counteracts the size dependence observed as a result of triple line pinning, the pinning energy barriers measured for the mildly rough substrates may be underestimated, although it is not clear if these phenomena are independent of how to separate them. But, since the droplets on rough substrates did not demonstrate clear halo regions, then the influence of Sn consumption outside of the TL perimeter is presumably minimal for rougher substrates. Finally, adjusting the reflow (reactive wetting) probably will not alleviate these complications. Longer reflow times may result in the smaller droplets over-reacting (see Figure 5.24 (b)) and ultimately receding, whereas, with shorter reflow times, the temperature ramping/cooling times become more significant than the temperature holding time, which can lead to new issues if the larger solder balls melt later than the smaller solder balls (due to their larger volume and the thermal contact resistance between the solder and substrate).

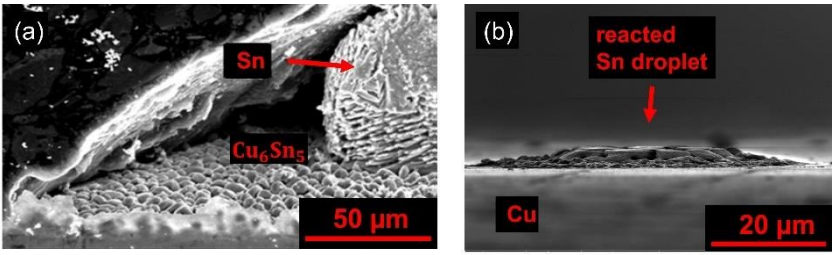

Figure 5.24: (a) Intermetallic grains become flatter closer to the droplet circumference. (b) A small Ø = 20 µm Sn droplet has wetted a Cu substrate and is largely consumed by the formation of intermetallic, demonstrating a very inhomogeneous surface morphology and relatively small CA. The reflow temperature was 350 °C (held for ~1 min).

6 Kinetics of solder spreading

6.1 Introduction

Until now, we have solely investigated reactive wetting equilibria, in particular reactive wetting angles, which are indicative of the wettability of a system and to an extent the quality of a solder joint. Yet to fully comprehend reactive wetting processes of solder, their spreading kinetics must also be investigated. Many material physical properties may influence the spreading rate of a wetting liquid, such as pressure, viscosity, density, capillary force, surface roughness. A reactive spreading system may additionally be influenced by chemical properties such as diffusion kinetics and reaction kinetics. This poses the question: which phenomena are predominant.

Of course, the spreading rate of non-reactive systems, without the application of external pressure, must always be controlled by a combination of viscosity, capillary force, and surface roughness, and is probably best described by the ratio of capillary force to viscosity, where the influence of the roughness is contained in the capillary force via the roughness parameter r according to Wenzel (16). Furthermore, any influence of viscosity is less significant for smaller drop sizes. In the case of reactive spreading, past studies have conversely argued that kinetics are controlled by either the reaction kinetics (always the case for pure metallic liquids) or in the case of a liquid alloy, possibly by the diffusion kinetics of the reactive element from the bulk liquid to the triple-line [65][47], i.e. for a bimetallic solder like SnPb, the spreading kinetics is controlled by the slower of the two phenomena. Diffusion kinetics may become decisive particularly as a reaction progresses and the concentration of the alloy's reactive component is depleted at the triple-line due to consumption. Unfortunately, although scientific discussion on the topic of reactive wetting kinetics exists [39,47,65,115–117], these studies have solely investigated high-temperature metal$^{(l)}$/ceramic$^{(s)}$ or metal$^{(l)}$/carbon$^{(s)}$ brazing systems (here metal also implies alloys). Furthermore, they do not use flux to remove any potential passive oxide layer from the base material which would otherwise limit the reactive spreading speed due to the additional time required for the liquid metal/alloy to penetrate the oxide. Finally, they typically compare the

measured reactive wetting kinetics with dissimilar systems, e.g. non-reactive wetting of organic liquids. Due to the plethora of factors influencing the kinetics of reactive wetting, it is wise to only compare truly similar systems.

One additional series of studies by Zhao et al. has attempted to overcome these shortcomings [118][113]. Their approach was to compare the reactive wetting kinetics in sessile drop geometry of various Sn-based lead-free solders on both pure Cu and Cu_6Sn_5 prepared surfaces. Unfortunately, it is difficult to draw conclusions from their kinetics results, because the radial spreading distances were too short (particularly for pure Cu substrates) and the temporal resolution was insufficient to properly gauge the spreading velocity. Zhao also investigated the spreading kinetics of eutectic SnPb solder on both pure Cu and Cu_6Sn_5 prepared surfaces, but for the Cu_6Sn_5 system, they observed only intergranular wetting of the IMC grains and could therefore not be compared with the Cu system which demonstrated the formation of a solder cap, thus representing a different wetting situation. The present study aims at overcoming the weaknesses of related past studies by measuring the kinetics of material systems which have similar physical properties but differ crucially in their reactive behavior. Thus we have chosen two solder alloys with similar compositions, Sn_4Pb_6 and Sn_3Pb_7, which nonetheless when melted on Cu at 350 °C have been demonstrated to grow different intermetallic phases at the liquid solder interface, namely Cu_6Sn_5 and Cu_3Sn respectively (see Figure 4.7). Thereby it is possible to compare spreading kinetics in dependence on the kinetics of product phase growth. Furthermore, the spreading kinetics of Sn_4Pb_6 on exposed Cu_6Sn_5 intermetallic substrates is also investigated, thereby removing the rate-limiting reaction step of reactive spreading and offering a useful comparison with the spreading experiments on pure Cu substrates.

6.2 Experimental

6.2.1 Substrate preparation

Wetting kinetics of SnPb solder alloys on both Cu and Cu_6Sn_5 IMC surfaces have been investigated. Instead of using the sessile drop geometry, the lollipop geometry described in section 5.1 has been utilized which offers a greater spreading distance over which the spreading kinetics can be evaluated. The same equilibrium and geometric conditions are valid as described in section 5.1. First, 37 x 14 x 1 mm Cu platelets (99.99% purity) were cut from Cu sheet. The platelets

were processed by milling away the edges of the desired geometry leaving only the free-standing lollipop structure attached at the plate base (see depiction: Figure 6.1). The geometric parameters were held constant at $r_p = 1$ mm and $\delta = 1.4$ mm across all kinetics measurements, since we are studying flow kinetics in dependence of material variation rather than size variation. The larger sample dimensions chosen here (compared to those of the miniaturization investigations discussed in section 5.6) decrease the impact of random microscopic imperfections (e.g. imperfect strip edges), thus limiting undesired statistical variation during spreading experiments while remaining sufficiently small to neglect gravitational force. Furthermore, the larger sample size permitted the use of mechanical sample processing techniques like milling, without compromising sample quality or reproducibility. The surfaces of the samples were then homogenized by grinding the surface of the lollipop structures with incrementally finer SiC grinding paper, finally down to 1200 grit. The Cu platelets were then separated into two groups; those intended for measuring spreading kinetics on a surface of either pure Cu or Cu_6Sn_5. The pure Cu samples required no further processing, whereas the Cu_6Sn_5 samples were prepared in such a way that the upper surface was composed of a homogeneous layer of Cu_6Sn_5 grains upon which solder spreading kinetics could be investigated and compared. To achieve this, the patterned Cu platelets were dipped into a furnace containing RMS flux and molten Sn for several minutes. The dipping time was varied between approximately 3-13 minutes to grow intermetallic layers of varying thickness. The platelets were then removed in such a way as to minimize residual liquid Sn solidifying on the newly formed IMC surface. This could not be altogether hindered, so the remaining Sn was etched from the structure surface. 37 % fuming HCL was used for the etching treatment and the samples were removed from the acid incrementally and observed via SEM

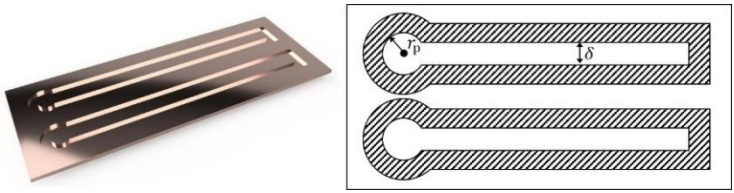

Figure 6.1: (left) CAD model of the Cu platelets after milling the edges of the lollipop test geometry as used in the kinetics experiments. (right) Top view of the same sample. Shaded regions represent shallower (ca. 0.5 mm deep) milled areas. For all samples, the dimensions were held constant at $r_p = 1$ mm and $\delta = 1.4$ mm.

to continuously control the extent of etching and avoid over-etching. After the Sn was completely etched from the surface of the Cu_6Sn_5 grains, the samples were cleaned in an ultrasound bath first with water, then acetone, then ethanol. The base of the samples was then roughly ground to remove any excess Sn or Cu_6Sn_5 to avoid the sample reacting to the heating furnace stage during the kinetics experiment. Figure 6.2 (a) shows the high homogeneity of the Cu_6Sn_5 grains at the microscopic scale via SEM micrograph. Although looking at the macroscopic picture of the pad surface in Figure 6.2 (b), some scattered imperfections were also observed. These came in the form of clusters of Cu_6Sn_5 grains protruding above the mean height of the surface, seemingly delaminated from the Cu surface and taking the shape of a small bubble or mound. These defects are neglected in subsequent analyses because of their low density and size. Finally, trial experiments revealed that the solder often flowed off the sides of the Cu_6Sn_5 samples during the kinetics measurements. It was hypothesized that this effect was caused by the Cu_6Sn_5 grains, which were formed over the entire sample during the

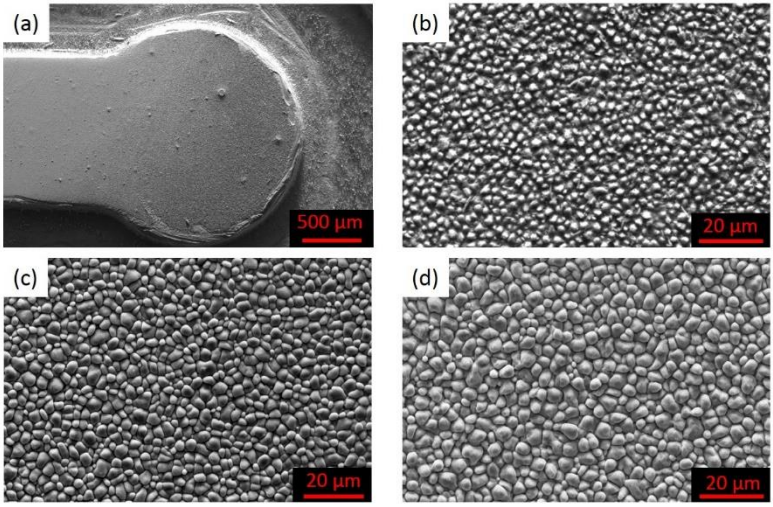

Figure 6.2: SEM micrographs of samples with exposed Cu_6Sn_5 surfaces, structured for kinetics experiments. (a) The pad of a structured kinetics sample before measurement, including visible edge abrasion which served to remove excess Cu_6Sn_5 grains at the structure edge. (b-d) displays the Cu_6Sn_5 grain size of three measured samples.

molten Sn dipping process, including at the structure edges, which facilitated intergranular wetting from the upper surface into the milled grooves. To hinder this impractically, the sidewalls of the pad and strip were mechanically abraded, removing the Cu_6Sn_5 grains at the edge (see edge abrasion of the pad in Figure 6.2 (a)). This method was sufficiently effective to contain the spreading solder upon the lollipop structure in the majority of cases. Furthermore, due to the abrasion localization at the structure edges, the accuracy of the measurements should not be negatively influenced.

6.2.2 Solder preparation

Both Sn4Pb6 and Sn3Pb7 solder compositions were prepared for the kinetics measures. Sn and Pb of 99.99 % purity were melted together in the required stoichiometric ratios in an open furnace filled with RMA flux to submerge the molten alloy and hinder oxidation. To avoid phase separation during recrystallization, the liquid alloys were poured onto a glass dish which was cooled in an ice bath. By this means the liquid recrystallized rapidly while dispersing into a thin layer from which the alloy could easily be cut. From the bulk solder alloys, small quantities were cut and weighed and subsequently melted into balls and re-solidified as previously outlined in 5.2.2. The solder ball mass was chosen corresponding to 80% of the volume of a hemisphere with a radius equal to the pad radius, thus assuring a large initial Laplace pressure.

6.2.3 Kinetics measurements

Kinetics measurements were conducted similarly as described in 5.2.3, with the CCD camera additionally recording a video of the solder spreading along the strip. The frame rate of the CCD camera was ca. 9 fps. From the recordings, the spreading distance was determined as a function of time.

6.3 Results and discussion

The results of all successful measurements are presented in Figure 6.3. Various observations can be made from the raw data. Moderate scatter is observed between the maximum spreading distance and the spreading rate of repeated measurements (shapes of the same color). Although we find the spreading rate (slope) and maximum spreading distance to be correlated; i.e. measurements that spread faster

also spread further. The green circle measurement (Sn_4Pb_6 on Cu_6Sn_5) appears to be an exception to this rule, spreading further than the faster spreading green square measurement, but this is only a measurement artifact.

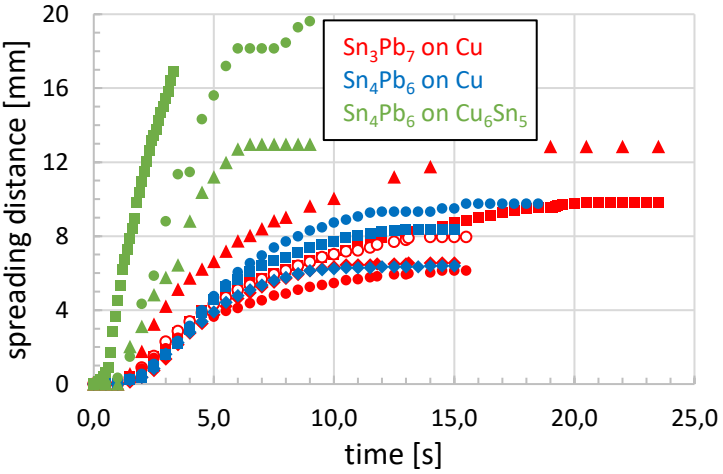

Figure 6.3: The spreading kinetics of various solder/substrate combinations. Measurements were conducted along narrow patterned strips. Different colors represent different material systems and repeated measurements are assigned different shapes. Variation in the number of data points between measurements is an artifact of flux coating which occasionally concealed the spreading solder front. The spreading rate increases significantly for pre-reacted substrates.

In actuality, during the green square measurement, the solder spread beyond the viewing window of the recorded video and thus could not be evaluated to the end of the measurement. The initial spreading rate on the pure Cu substrates (red and blue data) demonstrates the similarity between all measurements except one Sn_3Pb_7 measurement (red triangles) which spreads faster than the rest. This deviation is probably a result of an inconsistent sample surface, where the Cu surface was possibly ground to a different degree compared with the other measurements. Comparing the measurements of pure Cu vs Cu_6Sn_5 we find remarkably, as hypothesized, that the spreading kinetics of Sn_4Pb_6 are significantly faster on Cu_6Sn_5 intermetallic (green data) than on pure Cu. But counterintuitively, the measured wetting angles on the Cu vs Cu_6Sn_5 substrates are different (longer spreading distances correlate with smaller wetting angles). We might naively

expect the final wetting angles to be equivalent since Cu_6Sn_5 is also formed on the Cu track during the measurement as a result of the reactive spreading. Nonetheless, the wetting angles on the smooth Cu tracks are higher than on the pre-reacted tracks. This may although reasonably be explained by the differing surface roughnesses. Not only will the IMC track promote faster spreading (since the rate is not limited by IMC formation), but the roughness of the IMC track will also provide a higher driving force for spreading given the larger surface area (according to Wenzel, $F = \Delta\sigma_s - (\sigma_{lv}\cos\theta)/R$). The smooth Cu substrate conversely becomes rougher only after the formation of the IMC product phase. But remember that the Sn_4Pb_6 solder which spread on initially smooth Cu also come to rest in equilibrium on Cu_6Sn_5, so another possibility for differentiation must exist. Most likely, either: (i) the formed Cu_6Sn_5 morphology is less rough (lower surface area) than the pre-reacted tracks or (ii) the solder has not reached equilibrium. That is, given more time, the reaction and surface roughening at the triple line may have promoted continued but significantly slower spreading. But this seems to be the less likely of the two options considering that, within the spatial resolution of the experiments, the solder was observed to stop spreading.

Now considering the spreading rate in detail, the precise cause of the variation is not obvious. There are various differences between the pure Cu and Cu_6Sn_5 surfaces which may cause the observed effect. Probably the most predominant cause is that we presumably observe "Reaction Limited Spreading" (RLS) in the pure Cu case, and in the Cu_6Sn_5 case spreading is independent of the ongoing reaction, i.e. on the Cu_6Sn_5 surface, the spreading behavior should be similar to non-reactive spreading. Note, RLS encompasses the possibility of both "reaction-rate-limited" [117,119] and "diffusion-rate-limited" [120] spreading. Indeed, investigations on non-reactive wetting systems report significantly higher spreading rates than those reported for reactive systems [47,119], commonly reaching equilibrium in ~ 0.1 s . Although the spreading times on pre-reacted Cu_6Sn_5 are still much longer than those reported for inert systems, one must consider that inert wetting kinetics studies have largely applied the sessile drop measurement geometry, which by design offers significantly shorter total spreading distances. Furthermore, the high viscosity of the RMA flux we have used for oxide mitigation may retard the spreading speed of the molten solder, resulting in reduced spreading velocities between those of typical inert systems and reactive systems. Another possible cause for the increased spreading rates on Cu_6Sn_5 is the lower energy interface that SnPb shares with Cu_6Sn_5 compared with pure Cu, which increases the driving force for spreading. Finally, as previously

mentioned, the scallop grain morphology of the Cu_6Sn_5 surface is rougher than the pure Cu surface, which according to Wenzel (16) also increases the driving force for wetting. To further understand the influence of IMC roughness on spreading kinetics, we compare the initial surface morphologies of the Cu_6Sn_5 samples (Figure 6.2 (b-d)) with their corresponding measured spreading rates found in Figure 6.3 (green data): the green rectangles belong to surface (b), the green circles belong to surface (c), and the green squares belong to surface (d). Remarkably, the spreading rate increases with increasing grain size. This is presumably, a consequence of the larger surface area of the taller grains, and demonstrates the added complexity involved with finding a general model for reactive wetting kinetics.

Unfortunately, with the present experiments, it is difficult to completely separate the influences of surface energy, surface area, and reactive product formation on the kinetics of reactive wetting. To irrefutably separate these three influences, additional kinetics experiments using Sn_4Pb_6 solder should be conducted on: (i) smooth Cu_6Sn_5 substrates (removing the influence of roughness); (ii) pure Cu substrates with roughness morphology equivalent to the Cu_6Sn_5 grain morphology (although this cannot easily be manufactured); (iii) an inert substrate with surface/interface energy similar to Cu_6Sn_5 (removing any possibility of continued Cu_6Sn_5 formation). These recommended measurements would provide to determine the impact of the three dominant independent free parameters and are thus necessary to once and for all allow for the accurate description of the dependencies of reactive vs non-reactive wetting kinetics. Thus they should not be neglected, yet they are unfortunately out of the scope of this work.

Now we compare the measurements on pure Cu with Sn_4Pb_6 and Sn_3Pb_7 solder alloys. Given the experimental deviations between repeated measurements, the similarity between the spreading rates of both Sn_4Pb_6 and Sn_3Pb_7 does not permit a conclusive statement to be made about the dependence of the spreading kinetics on the particular IMC being formed. We may although hypothesize that the Sn_3Pb_7 solder should spread slower for two reasons: (i) the lower Sn concentration makes the solder more susceptible to diffusion kinetics limited spreading, where a low Sn concentration region exists near the reactive spreading triple line, (ii) Pb has a higher viscosity than Sn. Nonetheless, it is also possible that both solders are rather controlled by reaction kinetics limited spreading, in which case the above influences are irrelevant. Since we do not know the degree to which the spreading kinetics are expected to vary for similar solders which form different IMCs at the

liquid interface, it is recommended that the reproducibility of the measurements be improved. By this means, experimental error is reduced and the product-phase-dependent variation in spreading kinetics might be extracted.

7 Conclusions

Interpreting and understanding reactive wetting phenomena is crucial within the framework of ever-decreasing solder joint sizes. The studies presented in this thesis both build on the foundation of existing reactive wetting concepts and provide new insights into a largely overlooked area of reactive wetting; namely, the effect of joint size on wetting equilibria. By the systematic selection of material systems, substrate properties, and measurement conditions, these studies offer meaningful results which, corroborated with theoretical calculations and considerations, allow clear conclusions to be drawn on such questions as: (i) how best to quantify solder bond strength, (ii) how does solder joint size influence reactive wetting equilibria, and (iii) how does the inherent surface roughness and intermetallic roughness of a reactive solder joint affect the wetting equilibrium and spreading kinetics.

In our first study, we have investigated the work of adhesion of SnPb and SnBi solder alloys on both Cu and Ni substrates over their entire composition range at both 350 °C and 500 °C. Thus eight systems in total were investigated. For each system, the surface tensions and contact angles were experimentally measured for all compositions. The experimental conditions, in particular, the heat treatment and flux environment were kept constant across all measurements. This allowed the work of adhesion to be determined via the Young-Dupree equation which related the work of adhesion to the contact angle and surface tension. Using the sub-regular solution model with Redlich-Kister polynomials and applying the model of Butler [121] for interface segregation, the experimental data was modeled with good accuracy. CALPHAD Gibbs Energy calculations of the reactive wetting systems in combination with SEM micrographs and EDX analysis of selected intermetallic interfaces provided additional validation between the experimental observations and theoretical predictions. From these investigations, the following major conclusions can be drawn:

- For all eight systems, the wetting angles generally exhibit minimum values at intermediate solder compositions.

- The surface tensions of both SnPb and SnBi decrease with increasing Pb/Bi concentration. This decrease is stronger for the SnBi solder. The highly non-linear trends observed are clear indications of strong surface segregation of alloying components Pb/Bi, resulting from their lower partial surface energies.
- As a general rule, higher Sn concentration solders demonstrated higher work of adhesions. This contrasts with the contact angles measurements, which are commonly used as a quantification of joint strength, where lower angles are thought to represent stronger bonding strengths, but here demonstrate minimum values at intermediate concentrations. Since the work of adhesion by definition is a more precise representation of bonding strength, one can conclude that the contact angle can only be used as an approximation, but not an accurate representation of a solder joint's bonding strength.
- From thermodynamic modelling of the interface tension, it is suggested that strong segregation of Sn occurs near the solid-liquid interface, where the product phase is reacting.
- Concentration dependent characteristic discontinuities are observed in the work of adhesion, which correlate well with the composition dependent changes in the phase stabilities of the various intermetallic phases, as verified by binary Gibbs Energy plots and microscopic investigation of the intermetallic interface microstructure. This strongly supports the proposition of Eustathopoulos, that the low contact angle of reactive wetting bonds is highly dependent on the underlying product phase.

In our second study, we have investigated the effects of joint miniaturization on reactive wetting equilibria for both structured and unstructured substrates. First, electrodeposited Cu metallizations were structured with a long strip attached to a circular pad (lollipop geometry). Measurements were conducted by melting a eutectic SnPb solder ball on the pad so that it spread along the strip, and the equilibrium contact angles and spreading distances were measured. This was repeated for metallizations with a range of strip widths to evaluate the impact of solder joint size. The observed size effects are separated into two categories: (1) trivial size effects, resulting from variation in the Laplace pressure on the strip; (2) non-trivial size effects, which become predominant as the structure dimensions

approach the characteristic size of the surface roughness. The unstructured measurements were conducted with pure Sn on both rough electroplated and smooth polished Cu substrates. The joint size was investigated by varying the solder ball volume. From this study, the following conclusions can be drawn:

- Trivial size effects: As a consequence of the increasing capillary pressure, ΔP_s, with decreasing metallization strip width, δ, three trivial spreading regimes can be distinguished. In order of increasing δ, they are: (I) no spreading; (II) spreading distance limited by the high ΔP_s; (III) spreading distance limited by solder volume. The strip pressure is also dependent on the wetting angle and eutectic SnPb demonstrates a larger wetting angle on Ni than Cu. Consequently, Ni metallizations with smaller δ fell into regime (I), whereas all Cu metallizations fell within regime (III).
- Non-trivial size effects: An unexpected increase in the front wetting angle is observed with decreasing strip width. This cannot be understood by variation of the Laplace pressure and should ideally only depend on the capillary equilibrium. This size dependency was found to be well described by assigning an effective energy to the droplet triple line and modifying Young's energy balance. For eutectic SnPb on Cu, the effective triple line energy was determined to be $\epsilon_t = 0.73 \times 10^{-6}$ J/m. Although not initially obvious, the line energy was found to be best described as independent of joint dimensions (i.e. constant).
- The magnitude of ϵ_t is similar to those documented previously in literature for non-reactive systems. Nonetheless, the energy cannot be understood by disturbed chemical bonds at a triple line, which possess orders of magnitude smaller energies. Rather it can be interpreted as an energy barrier to the spreading triple line, caused by pinning of the triple line.
- Rough vs smooth Cu substrates: as the Sn drop size was decreased, the contact angle was found to increase on rough Cu and decrease on smooth Cu. This indicates that the hysteretic pinning effect is a consequence of the inherent substrate surface roughness and not of the rough product phase (scallop-shaped Cu_6Sn_5 grains).
- To rationalize the constant line energy barrier, the line pinning force must necessarily increase inversely to the joint size. Furthermore, this force must oppose both advancing and receding triple lines (hysteretic effect), so that the line energy must change sign for the receding case.

- The increasing pinning force with decreasing drop base radius could be rationalized as such: when the droplet base radius becomes larger, the triple line becomes linear relative to the roughness wavelength and more easily contort and relax around asperities, reducing the force required to jump between metastable configurations.
- An additional method for evaluating and explaining the relationship between drop size and contact angle was adapted from considerations of Shanahan for evaluating triple line Stick-Slip movement [26]. With this method, the so-called pinning energy barrier U calculated for all rough systems and was found to increase with increasing surface roughness. The larger advancing contact angles measured for smaller droplets on rough surfaces was rationalized by a reduction in the available excess capillary energy per triple line length (I.e. smaller droplets have less capillary energy to overcome the triple line pinning energy barrier).
- Finally, the CA of Sn solder droplets on polished Cu substrates demonstrated the opposite trend to that on rough substrates. This was found to result partially from the droplet losing Sn to the Cu_6Sn_5 interface reaction, partially from Sn loss into the so-called "halo region" which formed around the triple line perimeter, and partially due to the dynamic roughening of the surface around the triple line caused by intermetallic growth which probably caused a shift in the wetting equilibrium according to the concept of Wenzel.

Finally, reactive spreading kinetics were investigated in dependence of the product phase. The spreading kinetics of Sn_4Pb_6 and Sn_3Pb_7 solders were measured on smooth Cu tracks at 350 °C. At this temperature, the intermetallics expected to form in contact with the molten solder are Cu_6Sn_5 and Cu_3Sn respectively. Sn_4Pb_6 was also measured on a track of exposed Cu_6Sn_5 scallop grains which were pre-reacted and exposed via etching. The spreading kinetics on the Cu_6Sn_5 tracks were significantly faster than the Cu tracks. This was attributed primarily to the slower spreading on the Cu tracks which were limited by the rate of intermetallic formation. Although the increased roughness and lowered interface energy of the Cu_6Sn_5 tracks should also attribute to faster spreading.

8 References

1. Atkins, P. & de Paula, J. *Physical Chemistry*. *W. H. Freeman and Company* (Oxford University Press, 2006).

2. de Gennes, P.-G., Brochard-Wyart, F. & Quéré, D. *Capillarity and Wetting Phenomena*. *Journal of Chemical Information and Modelling* vol. 53 (Springer New York, 2004).

3. Moustafa, E.-A. *et al.* Investigating the Effect of Various Nanomaterials on the Wettability of Sandstone Reservoir. *World J. Eng. Technol.* **03**, 116–126 (2015).

4. Adhesives.org. Wetting - The physics behind wetting. https://www.adhesives.org/adhesives-sealants/science-of-adhesion/wetting.

5. Carré, A., Gastel, J. & Shanahan, M. E. R. Viscoelastic effects in the spreading of liquids. *Nature* **379**, 432–434 (1996).

6. Gelissen, E. J., van der Geld, C. W. M., Baltussen, M. W. & Kuerten, J. G. M. Modelling of droplet impact on a heated solid surface with a diffuse interface model. *Int. J. Multiph. Flow* **123**, 103173 (2020).

7. Cassie, B. D. & Baxter, S. wettability of porous surfaces. *Trans. faraday Soc.* **40**, 546–551 (1944).

8. He, X. *et al.* The Cassie-to-Wenzel wetting transition of water films on textured surfaces with different topologies. *Phys. Fluids* **33**, (2021).

9. Vanzo, D., Luzar, A. & Bratko, D. Reversible electrowetting transitions on superhydrophobic surfaces. *Phys. Chem. Chem. Phys.* **23**, 27005–27013 (2021).

10. C.W., E. & Extrand, C. W. A Thermodynamic Model for Contact Angle Hysteresis. *J. Colloid Interface Sci.* **207**, 11–19 (1998).

11. Chibowski, E. & Jurak, M. Comparison of contact angle hysteresis of different probe liquids on the same solid surface. *Colloid Polym. Sci.* **291**, 391–399 (2013).

12. Lam, C. N. C., Wu, R., Li, D., Hair, M. L. & Neumann, A. W. Study of the advancing and receding contact. *Adv. Colloid Interface Sci.* **96**, 169–191 (2002).

13. Long, J. & Chen, P. On the role of energy barriers in determining contact angle hysteresis. *Adv. Colloid Interface Sci.* **127**, 55–66 (2006).

14. Decker, E. L. & Garoff, S. Contact Line Structure and Dynamics on Surfaces with Contact Angle Hysteresis. *Langmuir* **13**, 6321–6332 (2002).

15. Erbil, H. Y. The debate on the dependence of apparent contact angles on drop contact area or three-phase contact line: A review. *Surf. Sci. Rep.* **69**, 325–365 (2014).

16. Xu, X. Modified Wenzel and Cassie Equations for Wetting on Rough Surfaces. *SIAM J. Appl. Math.* **76**, 2353–2374 (2016).

17. Shardt, N. & Elliott, J. A. W. Gibbsian Thermodynamics of Wenzel Wetting (Was Wenzel Wrong? Revisited). *Langmuir* **36**, 435–446 (2020).

18. Yildirim Erbil, H. Dependency of contact angles on three-phase contact line: A review. *Colloids and Interfaces* **5**, (2021).

19. Huh, C. & Mason, S. G. Effects of surface roughness on wetting (theoretical). *J. Colloid Interface Sci.* **60**, 11–38 (1977).

20. DETTRE, R. H. & JOHNSON, R. E. Contact Angle Hysteresis. in 136–144 (1964). doi:10.1021/ba-1964-0043.ch008.

21. Shuttleworth, R. & Bailey, G. L. J. The spreading of a liquid over a rough solid. *Discuss. Faraday Soc.* **3**, 16 (1948).

22. Extrand, C. W. Contact angles and hysteresis on surfaces with chemically heterogeneous islands. *Langmuir* **19**, 3793–3796 (2003).

23. Gao, L. & McCarthy, T. J. How Wenzel and Cassie Were Wrong. *Langmuir* **23**, 3762–3765 (2007).

24. Marmur, A. & Bittoun, E. When wenzel and cassie are right: Reconciling local and global considerations. *Langmuir* **25**, 1277–1281 (2009).

25. Panchagnula, M. V. & Vedantam, S. Comment on How Wenzel and Cassie Were Wrong by Gao and McCarthy. *Langmuir* **23**, 13242–13242 (2007).

26. Shanahan, M. E. R. & Sefiane, K. Kinetics Of Triple Line Motion During Evaporation. *Contact Angle, Wettability Adhes. Vol. 6* 19–32 (2010) doi:10.1163/ej.9789004169326.i-400.12.

27. Shanahan, M. E. R. Simple Theory of 'Stick-Slip' Wetting Hysteresis. *Langmuir* **11**, 1041–1043 (1995).

28. Bormashenko, E., Musin, A. & Zinigrad, M. Evaporation of droplets on strongly and weakly pinning surfaces and dynamics of the triple line. *Colloids Surfaces A Physicochem. Eng. Asp.* **385**, 235–240 (2011).

29. Promraksa, A. & Chen, L. J. Modelling contact angle hysteresis of a liquid droplet sitting on a cosine wave-like pattern surface. *J. Colloid Interface Sci.* **384**, 172–181 (2012).

30. Wang, F. C. & Wu, H. A. Molecular origin of contact line stick-slip motion during droplet evaporation. *Sci. Rep.* **5**, 1–10 (2015).

31. Semal, S. *et al.* Influence of Surface Roughness on Wetting Dynamics. *Langmuir* **15**, 8765–8770 (1999).

32. Chatain, D. & De Jonghe, V. Chemical wetting hysteresis. *J. Adhes.* **58**, 163–171 (1996).

33. Priest, C., Sedev, R. & Ralston, J. A quantitative experimental study of wetting hysteresis on discrete and continuous chemical heterogeneities. *Colloid Polym. Sci.* **291**, 271–277 (2013).

34. Roman, B. & Bico, J. Elasto-capillarity: Deforming an elastic structure with a liquid droplet. *J. Phys. Condens. Matter* **22**, (2010).

35. Pericet-Cámara, R., Best, A., Butt, H. J. & Bonaccurso, E. Effect of capillary pressure and surface tension on the deformation of elastic surfaces by sessile liquid microdrops: An experimental investigation. *Langmuir* **24**, 10565–10568 (2008).

36. Jerison, E. R., Xu, Y., Wilen, L. A. & Dufresne, E. R. Deformation of an elastic substrate by a three-phase contact line. *Phys. Rev. Lett.* **106**, 1–4 (2011).

37. Style, R. W. & Dufresne, E. R. Static wetting on deformable substrates, from liquids to soft solids. *Soft Matter* **8**, 7177–7184 (2012).

38. Saiz, E., Tomsia, A. P. & Cannon, R. M. Ridging effects on wetting and spreading of liquids on solids. *Acta Mater.* **46**, 2349–2361 (1998).

39. Saiz, E., Cannon, R. M. & Tomsia, A. P. Reactive spreading: Adsorption, ridging and compound formation. *Acta Mater.* **48**, 4449–4462 (2000).

40. Chatterjee, S., Pal Singh, K. & Bhattacharjee, S. Wetting hysteresis of

atomically heterogeneous systems created by low energy inert gas ion irradiation on metal surfaces: Liquid thin film coverage in the receding mode and surface interaction energies. *Appl. Surf. Sci.* **470**, 773–782 (2019).

41. Galleguillos-Silva, R., Vargas-Hernández, Y. & Gaete-Garretón, L. Wettability of a surface subjected to high frequency mechanical vibrations. *Ultrason. Sonochem.* **35**, 134–141 (2017).

42. Fuentes, C. A. *et al.* Equilibrium contact angle measurements of natural fibers by an acoustic vibration technique. *Colloids Surfaces A Physicochem. Eng. Asp.* **455**, 164–173 (2014).

43. Noblin, X., Buguin, A. & Brochard-Wyart, F. Vibrated sessile drops: Transition between pinned and mobile contact line oscillations. *Eur. Phys. J. E* **14**, 395–404 (2004).

44. Wang, F., Chen, H., Li, D., Zhang, Z. & Wang, X. Interfacial Behaviors in Cu / Molten Sn – 58Bi / Cu Solder Joints Under Coupling with Thermal and Current Stressing. *Electron. Mater. Lett.* **15**, 36–48 (2018).

45. Tadmor, R. & R., T. Line energy and the relation between advancing, receding, and Young contact angles. *Langmuir* **20**, 7659–7664 (2004).

46. Tadmor, R. *et al.* Measurement of lateral adhesion forces at the interface between a liquid drop and a substrate. *Phys. Rev. Lett.* **103**, 1–4 (2009).

47. Dezellus, O. & Eustathopoulos, N. Fundamental issues of reactive wetting by liquid metals. *J. Mater. Sci.* **45**, 4256–4264 (2010).

48. Eustathopoulos, N. Dynamics of wetting in reactive metal/ ceramic systems. *Acta Mater.* **46**, 2319–2327 (1998).

49. Meier, A., Javernick, D. A. & Edwards, G. R. Ceramic-Metal Interfaces and the Spreading of Reactive Liquids. *Jom* **51**, 44–47 (1999).

50. Shim, J.-H., Oh, C.-S. & Lee, B.-J. Thermodynamic assessment of the Cu-Sn system. *Zeitschrift fuer Met.* **87**, 156–162 (1996).

51. Gusak, A. M. & Tu, K. N. Kinetic theory of flux-driven ripening. *Phys. Rev. B - Condens. Matter Mater. Phys.* **66**, 1–14 (2002).

52. Tu, K. N. *et al.* Wetting reaction versus solid state aging of eutectic SnPb on Cu. *J. Appl. Phys.* **89**, 4843–4849 (2001).

53. Griffiths, S., Wedi, A. & Schmitz, G. Work of adhesion and reactive

wetting in SnPb/Cu,Ni and SnBi/Cu,Ni soldering systems. *Mater. Charact.* **178**, 111304 (2021).

54. Görlich, J., Baither, D. & Schmitz, G. Reaction kinetics of Ni/Sn soldering reaction. *Acta Mater.* **58**, 3187–3197 (2010).

55. Nash, P. Thermodynamic calculation of phase equilibria in the Ti-Co and Ni-Sn systems. *J. Mater. Sci.* **33**, 4929 – 4936 (1998).

56. Prasad, L. C. & Mikula, A. Concentration Fluctuations and Interfacial Adhesion at the Solid-Liquid Interface between Al2O3 and Al-Sn Liquid Alloys. *High Temp. Mater. Process.* **19**, 61–69 (2000).

57. Nikolopoulos, P., Agatho Pou Los, S., Angelopoulos, G. N., Naoumidis, A. & Grübmeier, H. Wettability and interfacial energies in SiC-liquid metal systems. *J. Mater. Sci.* **27**, 139–145 (1992).

58. Wang, S. F., Yang, T. C. K. & Lee, S. C. Wettability of electrode metals on barium titanate substrate. *J. Mater. Sci.* **36**, 825–829 (2001).

59. Wolansky, G. & Marmur, A. Apparent contact angles on rough surfaces: The Wenzel equation revisited. *Colloids Surfaces A Physicochem. Eng. Asp.* **156**, 381–388 (1999).

60. Kim, D., Pugno, N. M. & Ryu, S. Wetting theory for small droplets on textured solid surfaces. *Sci. Rep.* **6**, 1–8 (2016).

61. Forsberg, P. S. H., Priest, C., Brinkmann, M., Sedev, R. & Ralston, J. Contact line pinning on microstructured surfaces for liquids in the Wenzel state. *Langmuir* **26**, 860–865 (2010).

62. Quéré, D. Wetting and Roughness. *Annu. Rev. Mater. Res.* **38**, 71–99 (2008).

63. Yost, F. G. & Romig, A. D. Thermodynamics of Wetting by Liquid Metals. *MRS Proc.* **108**, 385 (1987).

64. Liu, C. Y. & Tu, K. N. Morphology of wetting reactions of SnPb alloys on Cu as a function of alloy composition. *J. Mater. Res.* **13**, 37–43 (1998).

65. Of, D. *et al.* DYNAMICS OF WETTING IN REACTIVE METAL / CERAMIC SYSTEMS : LINEAR SPREADING K . LANDRY and N . EUSTATHOPOULOS. *Acta Metall.* **44**, 3923–3932 (1996).

66. Saiz, E., Hwang, C. W., Suganuma, K. & Tomsia, A. P. Spreading of Sn-Ag solders on FeNi alloys. *Acta Mater.* **51**, 3185–3197 (2003).

67. Eustathopoulos, N. Progress in understanding and modelling reactive wetting of metals on ceramics. *Curr. Opin. Solid State Mater. Sci.* **9**, 152–160 (2005).

68. Drevet, B., Voytovych, R., Israel, R. & Eustathopoulos, N. Wetting and adhesion of Si on Si3N4 and BN substrates. *J. Eur. Ceram. Soc.* **29**, 2363–2367 (2009).

69. Stalder, A. F. *et al.* Low-bond axisymmetric drop shape analysis for surface tension and contact angle measurements of sessile drops. *Colloids Surfaces A Physicochem. Eng. Asp.* **364**, 72–81 (2010).

70. Butler, J. A. V. 348 J. A. V. Butler. **1**, 348–375 (1931).

71. Kaptay, G. Improved Derivation of the Butler Equations for Surface Tension of Solutions. *Langmuir* **35**, 10987–10992 (2019).

72. Li, J. G., Coudurier, L. & EustathoPouLos, N. Work of adhesion and contact-angle isotherm of binary alloys on ionocovalent oxides. *J. Mater. Sci.* **24**, 1109–1116 (1989).

73. Kaptay, G. A unified model for the cohesive enthalpy, critical temperature, surface tension and volume thermal expansion coefficient of liquid metals of bcc, fcc and hcp crystals. *Mater. Sci. Eng. A* **495**, 19–26 (2008).

74. Ohtani, H., Okuda, K. & Ishida, K. Thermodynamic study of phase equilibria in the Pb-Sn-Sb system. *J. Phase Equilibria* **16**, 416–429 (1995).

75. Malakhov, D. V., Liu, X. J., Ohnuma, I. & Ishida, K. Thermodynamic calculation of phase equilibria of the Bi-Sn-Zn system. *J. Phase Equilibria* **21**, 514–520 (2000).

76. Picha, R., Vřešťál, J. & Kroupa, A. Prediction of alloy surface tension using a thermodynamic database. *Calphad Comput. Coupling Phase Diagrams Thermochem.* **28**, 141–146 (2004).

77. Redlich, O. & Kister, A. T. Algebraic Representation of Thermodynamic Properties and the Classification of Solutions. *Ind. Eng. Chem.* **40**, 345–348 (1948).

78. Li, J. *et al.* Measurement and calculation of surface tension of molten Sn-Bi alloy. *J. Colloid Interface Sci.* **297**, 261–265 (2006).

79. Schwaneke, A. E., Falke, W. L. & Miller, V. R. Surface Tension and Density of Liquid Tin-Lead Solder Alloys. *J. Chem. Eng. Data* **23**, 298–301 (1978).

80. Howie, F. H. & Hondros, E. D. The surface tension of tin-lead alloys in contact with fluxes. *J. Mater. Sci.* **17**, 1434–1440 (1982).

81. Mills, K. C. & Su, Y. C. Review of surface tension data for metallic elements and alloys: Part 1 - Pure metals. *Int. Mater. Rev.* **51**, 329–351 (2006).

82. Keene, B. J. Review of data for the surface tension of pure metals. *Int. Mater. Rev.* **38**, 157–192 (1993).

83. Gąsior, W., Moser, Z. & Pstruś, J. Density and surface tension of the Pb-Sn liquid alloys. *J. Phase Equilibria* **22**, 20–25 (2001).

84. Moser, Z., Gasior, W. & Pstrus, J. Surface tension measurements of the Bi-Sn and Sn-Bi-Ag liquid alloys. *J. Electron. Mater.* **30**, 1104–1111 (2001).

85. Straumal, A. *et al.* Bulk and Surface Low Temperature Phase Transitions in the Mg-Alloy EZ33A. *Metals (Basel).* **10**, 1127 (2020).

86. Dinsdale, A. T. SGTE data for pure elements. *Calphad* **15**, 317–425 (1991).

87. Lukas, H., Fries, S. G. & Sundman, B. *Computational Thermodynamics*. (Cambridge University Press, 2007). doi:10.1017/CBO9780511804137.

88. Gierlotka, W., Chen, S. & Lin, S. Thermodynamic description of the Cu–Sn system. *J. Mater. Res.* **22**, 3158–3165 (2007).

89. Yoon, S. W. & Lee, H. M. A thermodynamic study of phase equilibria in the Sn-Bi-Pb solder system. *Calphad* **22**, 167–178 (1998).

90. Cho, J., Sheikhi, R., Mallampati, S., Yin, L. & Shaddock, D. Bismuth-Based Transient Liquid Phase (TLP) Bonding as High-Temperature Lead-Free Solder Alternatives. *Proc. - Electron. Components Technol. Conf.* 1553–1559 (2017) doi:10.1109/ECTC.2017.184.

91. Shen, Y. A. & Chen, C. Effect of Sn grain orientation on the formation of Cu6S5 intermetallic compounds during electromigration. *Proc. Tech. Pap. - Int. Microsystems, Packag. Assem. Circuits Technol. Conf. IMPACT* **128**, 85–86 (2016).

92. Kim, J., Jung, K.-H., Kim, J.-H., Lee, C.-J. & Jung, S.-B. Electromigration behaviors of Sn58%Bi solder containing Ag-coated MWCNTs with OSP surface finished PCB. *J. Alloys Compd.* **775**, 581–588 (2019).

93. Nguena, E., Danovitch, D., Sylvestre, J., Langlois, R. & Martel, S. Gallium Liquid Metal Embrittlement of Tin-based Solder Alloys. *Metall. Mater. Trans. A Phys. Metall. Mater. Sci.* **51**, 6222–6233 (2020).

94. Joanny, J. F. & De Gennes, P. G. A model for contact angle hysteresis. *J. Chem. Phys.* **81**, 552–562 (1984).

95. Bormashenko, E. Apparent contact angles for reactive wetting of smooth, rough, and heterogeneous surfaces calculated from the variational principles. *J. Colloid Interface Sci.* **537**, 597–603 (2019).

96. Yu, Y., Wu, Q., Zhang, K. & Ji, B. H. Effect of triple-phase contact line on contact angle hysteresis. *Sci. China Physics, Mech. Astron.* **55**, 1045–1050 (2012).

97. Bormashenko, E., Musin, A., Whyman, G. & Zinigrad, M. Wetting transitions and depinning of the triple line. *Langmuir* **28**, 3460–3464 (2012).

98. Liu, J., Mei, Y. & Xia, R. A new wetting mechanism based upon triple contact line pinning. *Langmuir* **27**, 196–200 (2011).

99. Tadmor, R. Line energy, line tension and drop size. *Surf. Sci.* **602**, 12–15 (2008).

100. Good, R. J. & Koo, M. N. The effect of drop size on contact angle. *J. Colloid Interface Sci.* **71**, 283–292 (1979).

101. Arenas, M. F. & Acoff, V. L. Contact angle measurements of Sn-Ag and Sn-Cu lead-free solders on copper substrates. *J. Electron. Mater.* **33**, 1452–1458 (2004).

102. Satyanarayan & Prabhu, K. N. Spreading behavior and evolution of IMCs during reactive wetting of SAC solders on smooth and rough copper substrates. *J. Electron. Mater.* **42**, 2696–2707 (2013).

103. Sekulic, D. P. Wetting and spreading of liquid metals through open microgrooves and surface alterations. *Heat Transf. Eng.* **32**, 648–657 (2011).

104. Eustathopoulos, N. Wetting by Liquid Metals—Application in Materials Processing: The Contribution of the Grenoble Group. *Metals (Basel).* **5**, 350–370 (2015).

105. F.M. Hosking, F.G. Yost, E.A. Holm, and J. R. M., Hosking, F. M., Yost, F. G., Holm, E. A. & Michael, J. R. Solder flow on narrow copper strips. *J. Electron. Mater.* **25**, 1099–1107 (1996).

106. Griffiths, S. J., Jantimapornkij, P. & Schmitz, G. Miniaturization, Triple-Line Effects, and Reactive Wetting of Microsolder Interfaces. *ACS Appl.*

Mater. Interfaces **12**, 8935–8943 (2020).

107. Li, J. F., Agyakwa, P. A. & Johnson, C. M. Interfacial reaction in Cu/Sn/Cu system during the transient liquid phase soldering process. *Acta Mater.* **59**, 1198–1211 (2011).

108. MCGUIRE, J. & YANG, J. The Effect of Drop Volume on Contact Angle. *J. Food Prot.* **54**, 232–235 (2016).

109. Drelich, J. & Miller, J. A. N. D. THE LINE / PSEUDO-LINE TENSION IN THREE-PHASE SYSTEMS. **6351**, (2007).

110. Görlich, J., Schmitz, G. & Tu, K. N. On the mechanism of the binary Cu/Sn solder reaction. *Appl. Phys. Lett.* **86**, 053106 (2005).

111. Suh, J. O., Tu, K. N. & Gusak, A. M. Morphology Change, Size Distribution, and Nano-sized Channels in Cu 6 Sn 5 Intermetallic Compound Formation at the SnPb Solder and Copper Interface. *MRS Proc.* **863**, B10.3 (2005).

112. Rodríguez-Valverde, M. A., Montes Ruiz-Cabello, F. J. & Cabrerizo-Vílchez, M. A. A new method for evaluating the most-stable contact angle using mechanical vibration. *Soft Matter* **7**, 53–56 (2011).

113. Zhao, H., Nalagatla, D. R. & Sekulic, D. P. Wetting kinetics of eutectic lead and lead-free solders: Spreading over the Cu surface. *J. Electron. Mater.* **38**, 284–291 (2009).

114. Huang, M. L. & Yang, F. Size effect model on kinetics of interfacial reaction between Sn-xAg-yCu solders and Cu substrate. *Sci. Rep.* **4**, 1–9 (2014).

115. Yost, F. G. Kinetics of reactive wetting. *Scr. Mater.* **42**, 801–806 (2000).

116. Mortensen, A., Drevet, B. & Eustathopoulos, N. Reply to `` Kinetics of reactive wetting ' '. **45**, 953–956 (2001).

117. Dezellus, O., Hodaj, F. & Eustathopoulos, N. Chemical reaction-limited spreading: The triple line velocity versus contact angle relation. *Acta Mater.* **50**, 4741–4753 (2002).

118. Zhao, H., Wang, H. Q., Sekulic, D. P. & Qian, Y. Y. Spreading kinetics of liquid solders over an intermetallic solid surface. Part 2: Lead-free solders. *J. Electron. Mater.* **38**, 1846–1854 (2009).

119. Eustathopoulos, N., Garandet, J. P. & Drevet, B. Influence of reactive solute transport on spreading kinetics of alloy droplets on ceramic

surfaces. *Philos. Trans. R. Soc. A Math. Phys. Eng. Sci.* **356**, 871–884 (1998).

120. Mortemen ', A., Drevet2, B., Eustathopoulos3, N. & Fourt, M. KINETICS OF DIFFUSION-LIMITED SPREADING OF SESSILE DROPS IN REACTIVE WETTING currently on sabbatical leave at the Centre des Materiaux Pierre. *Scr. Mater.* **36**, 645–651 (1997).

121. Butler, J. A. V. The Thermodynamics of the Surfaces of Solutions. *Proc. R. Soc. A Math. Phys. Eng. Sci.* **135**, 348–375 (1932).

122. Karakaya, I. & Thompson, W. T. The Pb-Sn (Lead-Tin) system. *J. Phase Equilibria* **9**, 144–152 (1988).

123. Vianco, P. T. & Rejent, J. A. Properties of ternary Sn-Ag-Bi solder alloys: Part I - thermal properties and microstructural analysis. *J. Electron. Mater.* **28**, 1127–1137 (1999).

9 Appendix

9.1 Sn/Pb phase diagram

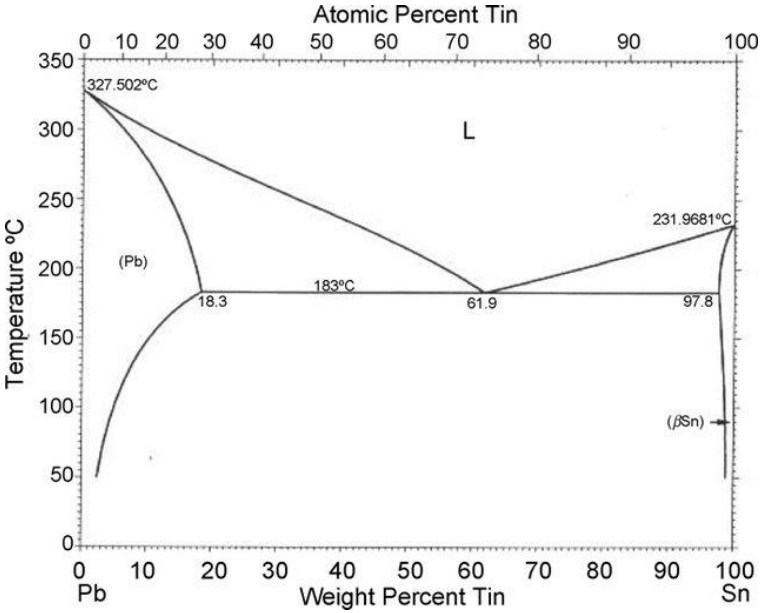

Figure 9.1: Thermodynamic optimization calculation of the Sn-Pb solder system phase diagram [122].

9.2 Sn/Bi phase diagram

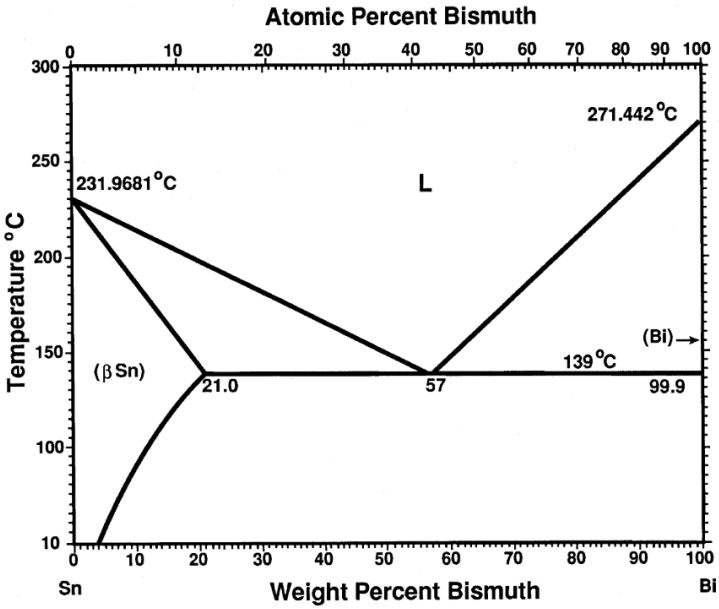

Figure 9.2: Thermodynamic optimization calculation of the Sn-Bi solder system phase diagram [123].

List of publications

(1) Griffiths SJ, Jantimapornkij P, Schmitz G. Miniaturization, Triple-Line Effects, and Reactive Wetting of Microsolder Interfaces. ACS Appl Mater Interfaces. 2020 Feb 19;12(7):8935-8943. doi: 10.1021/acsami.9b22512.

(2) Griffiths SJ, Wedi A, Schmitz G. Work of adhesion and reactive wetting in SnPb/Cu,Ni and SnBi/Cu,Ni soldering systems. Mater Charact. 2021 July 6, 178:1-11. Doi: 10.1016/j.matchar.2021.111304.

Acknowledgments

First I would like to express my deepest gratitude to my academic supervisor Prof. Dr. Dr. h.c. Guido Schmitz, whose guidance has allowed me to flourish as a junior scientist. Under his supervision at the chair for materials physics, I have learned to apply the scientific process to the highest degree and have become more confident in my abilities. Furthermore, in times of struggle during my research, his support and dedication have been invaluable. For these reasons and more, I am thankful.

I would also like to thank Prof. Dr.-Ing. Andre Zimmermann and Prof. Dr. Peer Fischer for showing interest in my doctoral research and accepting to be co-examiner and chairman of this dissertation respectively.

A special thanks to all my colleagues for their positive attitude around the institute. Thank you to Peter Engelhardt and Frank Hack who were always friendly and available to help in the laboratory. A special thanks to our postdocs Dr. Patrick Stender, Dr. Gábor Csizár, Dr. Sebastian Eich, who are very knowledgeable and were always open for discussion (not always work-related). Thank you to all of my students alongside whom I enjoyed working, and a special thanks to Fateeha Zuhaib who provided valuable support to my research interests. Finally, a big "cheers" to all of my fellow Ph.D. institute buddies, in particular my various office buddies, Robert (Roberto) Lawitzki, Yug Yoshi, Rüya Duran, Ahmed Mohamed (the King of …), Jianshu Zheng (JZ), and Helena (Hells Bells) Solodenko with whom I have shared all the inevitable ups and downs of our Ph.D. journey, as well as numerous memorable occasions in leisure time.

Last but not least, I am very grateful to all my friends and family who give my life joy and meaning, and of whom there are, unfortunately (or rather, fortunately) too many to list here. To those closest to me: I want to express my deepest gratitude to my loving family, Susan, Cameron, Ella, and Tony who are all legends and have always remained supportive of my choices, in particular leaving my home country

Australia to live in Germany, and whose regular contact is sorely missed. Finally, to my loving partner, Armaghan who, throughout my doctoral research, has been supportive in every way, lending an open ear, sharing the good times, remaining positive in difficult times, cooking delicious Fesenjoon (numerously), and being generally awesome to be around.

Declaration of Authorship

I hereby certify that the dissertation entitled

„Reactive wetting of miniaturized Sn-based solder joints“

is entirely my own work except where otherwise indicated. Passages and ideas from other sources have been clearly indicated.

Erklärung über die Eigenständigkeit der Dissertation

Ich versichere, dass ich die vorliegende Arbeit mit dem Titel

„Reaktive Benetzung miniaturisierter Sn-basierter Lötstellen“

selbständig verfasst und keine anderen als die angegebenen Quellen und Hilfsmittel benutzt habe; aus fremden Quellen entnommene Passagen und Gedanken sind als solche kenntlich gemacht.

Name/Name: Samuel Jordan Griffiths

Unterschrift/Signed: _____

Datum/Date: _____